



Virginia Commonwealth University
VCU Scholars Compass

Theses and Dissertations


Graduate School

2016

Laser Vaporization Controlled Condensation and Laser Irradiation in Solution for the Synthesis of Supported Nanoparticle Catalysts

Vitaly Kisurin Mr.

Follow this and additional works at: <https://scholarscompass.vcu.edu/etd>

 Part of the [Materials Chemistry Commons](#), and the [Physical Chemistry Commons](#)

© The Author

Downloaded from

<https://scholarscompass.vcu.edu/etd/4636>

This Thesis is brought to you for free and open access by the Graduate School at VCU Scholars Compass. It has been accepted for inclusion in Theses and Dissertations by an authorized administrator of VCU Scholars Compass. For more information, please contact libcompass@vcu.edu.

Laser Vaporization Controlled Condensation and Laser Irradiation in Solution for the Synthesis of Supported Nanoparticle Catalysts.

A thesis submitted in partial fulfillment of the requirements for the degree of Master of Science
at Virginia Commonwealth University

By

Vitaly Y. Kisurin

B.S., Chemistry, Virginia Commonwealth University, Richmond, Virginia 2016

Director: M. Samy El-Shall

Chair, Department of Chemistry

Virginia Commonwealth University

Richmond, Virginia

Spring 2016

Acknowledgments

First and foremost, I would like to thank my advisor Dr. Samy El-Shall for providing me with the opportunity to work in his lab. The extravagant instruments and equipment in this lab are dear to me, and have served as a source of practice and inspiration for other potential projects. I especially enjoyed working with the Nd:YAG pulsed laser and I hope that I will be able to continue working with it in the near future.

Continuing with appreciation, I would like to thank my committee members Dr. Jena, Dr. El-Kaderi and Dr. Tibbetts for their moral support and help in writing this thesis. Their impact and guidance was really valuable and taught me to always be appreciative and understanding of all forms of advice

I additionally want to express my gratitude and appreciation to my friends and fellow lab mates Andrew Lin, Julian Bobb, Hiran Danushka, Adam Percy, Pezhman Arab, Babak Ashourirad, Tsemre Tessema, Ryon Smith, Colleen Malone, Logan Wilder, Ashley Fourney, Sarah Smith, Melissa Tsui and Brent Williams for their support, optimistic attitude and help on multiple occasions when I needed it. I am very grateful to have so many friends that are truly thoughtful, considerate and kind towards me.

I would also like to thank the rest of Dr. El-Shall's lab group members Khaled Abouzeid, Amr Awad, Sean Platt, Kyle Mason and Kwame Isaac Attah for all the help around the lab and continuous support and advice on various matters. Moreover, I appreciate the friendly atmosphere their presence created in the lab, which was crucial in contributing towards a successful working environment.

I would like to thank my collaborators Dr. Ali Siamaki for providing me the data for cross-coupling reactions and Stanley Gilliland for helping me with performing catalysis reactions on carbon cross coupling. I would also like to thank Khaled Abozeid, Julian Bobb and Tsemre Tessema for performing TEM, XPS and nitrogen uptake measurements respectively for my samples.

A special thanks should be addressed to the creators of the EndNote software. With the use of EndNote, near-automatically citing scientific articles in the appropriate areas and in the correct order simplified significantly the thesis writing process. Without these people and such wonderful software, my writing would be unimaginably difficult.

Additionally, I am blessed and very lucky to have a wonderful family. I am forever indebted to my parents for raising and taking utmost care of me. They have been instrumental in ensuring I aim for the best life has to offer, in maintaining my emotional stability, and in teaching me many useful skills and knowledge to carry on in college and then graduate school.

I would like to thank my significant other - Eleni Galanopolous for continuous support and help throughout these years. I am grateful for her love, as she is always willing to listen to me during difficult times and cheer me up with a good advice.

I would like to thank my tutor and mentor Ivan Korablev-Dyson for providing continuous support and great advice throughout many years I have known him. I am grateful to have him as a friend, as he always cheers me up at times when my days seemed more difficult to face than others.

Lastly, but definitely not least, I would like to express my deepest gratitude to all the teachers and mentors I had up to this point in my academic career.

Table of Contents

List of Figures	v
List of Tables	Error! Bookmark not defined.
List of Equations	Error! Bookmark not defined.
Abstract	viii
CHAPTER 1	1
Introduction.....	1
1.1 Objective Statement	1
1.2. Approach.....	1
1.3 Organization of Chapters	2
CHAPTER 2	4
2.1 Literature Review and Background	4
CHAPTER 3	10
Experimental	10
3.1 Overview.....	10
3.2 Laser Vaporization Controlled Condensation (LVCC).....	10
3.2.1 Laser Assisted Synthesis of SiO _x Nanoparticles	14
3.2.2 Laser Assisted Synthesis of SiO _x /Si-RGO Supports.....	14
3.2.3 Incorporation of Palladium Nanoparticles into SiO _x /RGO supports	15
3.3 Laser Irradiation In Solution	15
3.3.1 Chemical Synthesis of UiO-67 Metal-Organic Framework.....	15
3.3.2 Preparation and Incorporation of Palladium Nanoparticles into the UiO-67 Framework	16
3.4 Heterogeneous Catalysis	17
3.4.1 Carbon Cross Coupling Reactions in Microwave Reactor	17
3.4.2. Oxidation of Benzyl Alcohol in the Autoclave Reactor	17
CHAPTER 4	19
4 Laser Assisted Synthesis Results and Discussion.....	19
4.1 Characterization of SiO _x Nanoparticles	19
4.1.1 UV-Vis Spectroscopy	19
4.1.2. FTIR Spectroscopy	21
4.1.3 Photoluminescence	23
4.1.4 Raman Spectroscopy.....	25
4.1.5 Powder X-Ray Crystallography	27

4.1 Characterization of SiO_x -RGO support	29
4.2.1. FTIR Spectroscopy.....	29
4.2.2 Powder X-ray Crystallography	30
4.2.3 X Ray Photoelectron Spectroscopy.....	33
4.2.4 Transmission Electron Microscopy	36
4.2.5 Raman Spectroscopy.....	38
4.2 Carbon Cross-Coupling Reactions Results	41
4.3 Characterization of Pd@UiO-67 catalyst.....	51
4.3.1 X-ray Diffraction	54
4.3.2 FTIR Spectroscopy	55
4.3.3 Nitrogen Adsorption Isotherms.....	56
4.3.4 Pore Size Distribution	59
4.3.5 Transmission Electron Microscopy	61
4.4 Benzyl Alcohol Oxidation Results.....	70
CHAPTER 5	86
5.1 Concluding Remarks.....	86
5.2 Future Research	89
LIST OF REFERENCES	92
VITA	101

List of Figures

Figure 1. Experimental LVCC setup used to synthesize nanoparticles of controlled size. . **Error! Bookmark not defined.**

Figure 2. LVCC chamber from (A) side view and (B) top view with the upper steel plate removed for clarity purposes..... **Error! Bookmark not defined.**

Figure 3. Incorporation and reduction of palladium precursor in UiO-67 during pulsed laser irradiation. **Error! Bookmark not defined.**

Figure 4. Suzuki-Miyaura Cross-Coupling reaction with the use of Pd/ SiO_x -RGO catalyst. **Error! Bookmark not defined.**

Figure 5. Benzyl alcohol oxidation over palladium nanoparticles supported on UiO-67 MOF. **Error! Bookmark not defined.**

Figure 6. UV-Vis spectrum of silicon nanoparticles in methanol solvent synthesized by LVCC process. **Error! Bookmark not defined.**

Figure 7. FTIR Spectrum of silicon nanoparticles synthesized by LVCC method. **Error! Bookmark not defined.**

Figure 8. Photoluminescence of silicon nanoparticles synthesized by LVCC method.. **Error! Bookmark not defined.**

Figure 9. Raman spectrum of surface-oxidized silicon nanoparticles synthesized by LVCC method... **Error! Bookmark not defined.**

Figure 10. Powder X-ray diffraction of silicon nanoparticles synthesized by LVCC method. **Error! Bookmark not defined.**

Figure 11. FTIR spectrum of Si nanoparticles (black) and SiO_x-RGO support (red). **Error! Bookmark not defined.**

Figure 12. Powder XRD pattern of Si(50%) RGO(50%) support with 10 % by weight of palladium nanoparticles deposited on the support. **Error! Bookmark not defined.**

Figure 13. Powder XRD pattern of Si(80%) G(20%) support with 10 % by weight of palladium deposited on the support. **Error! Bookmark not defined.**

Figure 14. Powder XRD of reduced graphene with palladium nanoparticles deposited on its surface. **Error! Bookmark not defined.**

Figure 15. XPS binding energies of palladium in G-Pd (10%) sample **Error! Bookmark not defined.**

Figure 16. XPS spectrum of Pd/SiO_x-RGO showing the oxidation states of palladium catalyst..... **Error! Bookmark not defined.**

Figure 17. XPS spectrum of Pd/SiO_x-RGO sample with 10% palladium by weight..... **Error! Bookmark not defined.**

Figure 18. TEM images of Graphene with 10% palladium by weight deposited on the sheets **Error! Bookmark not defined.**

Figure 19. TEM images of Pd/SiO_x-RGO and 10% palladium by weight..... **Error! Bookmark not defined.**

Figure 20. TEM images of silicon-graphene support with embedded palladium nanoparticles 10% by weight. **Error! Bookmark not defined.**

Figure 21. Raman scattering of SiO_x-RGO support used for carbon cross-coupling reactions..... **Error! Bookmark not defined.**

Figure 22. Raman scattering of Graphene Oxide..... **Error! Bookmark not defined.**

Figure 23. Suzuki-Miyaura cross-coupling reaction between bromobenzene and phenylboronic acid to produce biphenyl. **Error! Bookmark not defined.**

Figure 24. Sonogashira reactions using 10% palladium by weight on SiO_x/RGO support and its corresponding conversion into products..... **Error! Bookmark not defined.**

Figure 25. (Left) UiO-66 with BDC linkers, (center) UiO-67 with BPDC linkers and (right) UiO-68 MOF with TPDC linkers **Error! Bookmark not defined.**

Figure 26. Powder X ray diffraction patterns of (black) UiO-67 (red) Pd/UiO-67 (blue) Pd/UiO-67 after benzyl alcohol oxidation reaction.	Error! Bookmark not defined.
Figure 27. Fourier Transformation Infrared spectra of UiO-67 crystals	Error! Bookmark not defined.
Figure 29. Pore size distribution of (black) UiO-67 and (red) Pd@UiO-67	Error! Bookmark not defined.
Figure 30. Transmission electron micrographs of UiO-67 crystals	Error! Bookmark not defined.
Figure 31. TEM image (A) of Pd@UiO-67 MOF crystal with 1% palladium by weight (B) size distribution of palladium nanoparticles on the UiO-67 MOF	Error! Bookmark not defined.
Figure 32. TEM image (A) of Pd@UiO-67 MOF crystals with 2% palladium by weight, (B) size distribution of palladium nanoparticles within UiO-67	Error! Bookmark not defined.
Figure 33. TEM images (A) of Pd@UiO-67 MOF crystal with 5% palladium by weight and (B) size distribution of palladium nanoparticles within UiO-67	Error! Bookmark not defined.
Figure 34. UV-Vis spectra of UiO-67 in ethanol (black) and water (red).	Error! Bookmark not defined.
Figure 35. UV-Vis spectra of palladium nitrate after laser irradiation.	Error! Bookmark not defined.
Figure 36. Mole conversion of benzyl alcohol into products versus time	Error! Bookmark not defined.
Figure 37. Influence of temperature on (A) mole conversion of benzyl alcohol and (B) selectivity for benzaldehyde at a constant pressure of 0.7 MPa.	Error! Bookmark not defined.
Figure 38. Influence of pressure on (A) mole conversion of benzyl alcohol and (B) selectivity for benzaldehyde at a constant temperature of 100 °C.....	Error! Bookmark not defined.
Figure 39. Influence of (A) solvent in the autoclave reactor on the mole conversion of benzyl alcohol and (B) selectivity for benzaldehyde.....	Error! Bookmark not defined.
Figure 40. The effect of various reducing solvents during laser irradiation on the (A) mole conversion of benzyl alcohol and (B) selectivity for benzaldehyde.....	Error! Bookmark not defined.
Figure 41. Influence of (black) compressed oxygen at 0.7 Mpa (red) oxygen flow (blue) compressed air and (green) air flow at 1 atm on conversion of (A) benzyl alcohol and (B) selectivity for benzaldehyde.	Error! Bookmark not defined.

List of Tables

Table 1 Palladium Wt% Distribution versus Conversion	43
Table 2 Reusability of the Pd-SiO _x -RGO Catalyst	44
Table 3 Comparison of Catalytic Activity Among Pd/SiO _x -RGO Catalysts	45
Table 4 Comparison With Published Literature Results	50
Table 5 Summary of Benzyl Alcohol Reactions in Different Reaction Conditions	82
Table 6 Comparison of Pd@UiO-67 with Published Literature	85

List of Equations

Equation 1 Palladium weight % in SiO _x -RGO support	41
Equation 2 Conversion % of Biphenyl Product	42
Equation 3 Palladium weight % in UiO-67	62
Equation 4 Conversion % of Benzaldehyde Product	72
Equation 5 TOF calculation for Benzyl Alcohol Oxidation	80

Abstract

Solid catalyst supports of SiO_x-RGO (Reduced Graphene Oxide) and UiO-67 (*Universitet i Oslo*) have been successfully synthesized and were loaded with palladium nanoparticles to test for a series of heterogeneous reactions. The SiO_x/RGO catalysts were synthesized through laser ablation of silicon and graphite oxide micron powder and UiO-67 metal-organic framework (MOF) was synthesized through mixing of precursors with DMF/HCl solution and washing the resultant powder from impurities. The SiO_x/RGO supports were later impregnated with palladium precursors which were then subject to Microwave Irradiation (MWI). The UiO-67 framework was impregnated with palladium precursors and was irradiated with pulsed Nd:YAG 532 nm laser and was purified through washing and centrifugation. The resulting catalyst supports were characterized with UV-Vis, FTIR, Raman, XRD and XPS techniques and the UiO-67 framework was subject to Brunauer-Emmet-Teller (BET) surface area measurements before

and after the catalytic reactions. The catalytic activity of palladium nanoparticles supported on SiO_x/RGO and UiO-67 framework was tested in carbon cross-coupling reactions of Suzuki-Miyaura, Sonogashira reactions and oxidation of benzyl alcohol respectively. The catalysts have demonstrated excellent performance and have yielded a promising future for the catalytic supports in the previously stated reactions.

CHAPTER 1

Introduction

1.1 Objective Statement

The objective of this research is to synthesize SiO_x -RGO and UiO-67 supports, load them with palladium nanoparticles and study the resulting catalyst systems for heterogeneous catalysis. Reactions of interest are carbon cross-coupling such as Suzuki-Miyaura and Sonogashira as well as solvent-free oxidation of benzyl alcohol. Prior to performing reactions the supports will be characterized by various techniques to verify their structure and chemical identity. Subsequently, the reactions will be examined for conversion, selectivity and reusability of the catalysts and future research will be discussed in the light of gathered results.

1.2. Approach

Synthesis of SiO_x -RGO supports requires the preparation of solid target pellet for the laser ablation by using hydraulic press and micron powders of silicon and graphite oxide. After the laser ablation process, the synthesized SiO_x -RGO supports are impregnated with palladium precursors in water solution and chemically reduced in conventional microwave oven. The resulting catalysts are then characterized by UV-Vis, FTIR and Raman spectroscopy as well as x-ray diffraction, x-ray photoelectron spectroscopy and electron microscopy. UV-Vis, FTIR and Raman spectroscopy enables to identify the presence of silicon and carbon in the supports, the amount of defects present in reduced graphene oxide and possible size of silicon nanoparticles. X-ray diffraction allows us to see the crystallinity of the sample, nature of the chemical elements present in the sample and possible size of the palladium nanoparticles. X-ray photoelectron

spectroscopy provides detailed information on oxidation states of palladium nanoparticles supported on the catalyst and helps identify what species are most active for the catalysis. Electron microscopy aids in visualizing how the palladium nanoparticles are dispersed throughout the sample and provide information on particle size distribution and theoretical active sites available on the surface of the nanoparticles available for catalysis.

Synthesis of Pd@UiO-67 catalyst requires preparation of UiO-67 metal-organic framework. Palladium precursor is impregnated into UiO-67/ethanol mixture and is then irradiated by laser. Subsequently, the resulting mixture is washed and centrifuged to eliminate the unwanted solvent and other reagents. The resulting catalyst is then characterized by FTIR spectroscopy, x-ray crystallography, electron microscopy and is subject to BET surface area measurements. FTIR spectroscopy would provide us with information on presence of linkers and inorganic nodes in UiO-67 as well as presence or absence of residual reagents or contaminants in the pores. X-ray diffractions would demonstrate the crystallinity of the metal-organic framework sample before and after palladium impregnation as well as its crystallinity after the reaction. Electron microscopy would aid in visualizing the size of MOF crystals as well as provide information on size and dispersion of palladium nanoparticles in the UiO-67. Additionally, electron microscopy would help in determining the particle size distribution and theoretical number of active sites available on the surface of palladium nanoparticles. BET surface area measurements would provide the surface area of UiO-67 metal-organic framework and its porosity which is crucial for high surface area supports.

1.3 Organization of Chapters

The thesis is subdivided into several chapters. Chapter 1 gives reader a brief introduction and motivation about the work written.

Chapter 2 gives a more thorough introduction and background on nanoparticles, heterogeneous catalysis, graphene, UiO-67 metal-organic framework, carbon cross-coupling reactions and alcohol oxidation reactions.

Chapter 3 introduces the reader with experimental details of SiO_x-RGO and UiO-67 synthesis, palladium impregnation procedures, LVCC process and procedure for heterogeneous reactions performed.

Chapter 4 demonstrates the characterization of SiO_x-RGO and UiO-67 supports and results of reactions performed followed by discussion and comparison with published literature work.

Chapter 5 presents the reader with concluding remarks of performed work and discussion of possible research implemented in the future.

CHAPTER 2

2.1 Literature Review and Background

Nanoparticles are defined as solid particles with a size range from 1-100 nm in at least one of their dimensions. These particles have received significant research interest in the past two decades due to their interesting properties such as quantum size confinement, surface plasmon resonance and high surface area. Because of these unique properties nanoparticles are different from their bulk counterparts and offer a wide range of potential applications in the areas of pharmaceuticals¹⁻³, catalysis⁴⁻⁶, solar cells⁷⁻¹⁰ and energy storage^{11, 12}.

Nanoparticles can be classified into two main groups: metallic nanoparticles and semiconductor nanoparticles, sometimes known as quantum dots. Metallic nanoparticles usually consist of metal particles which can have a thin oxide layer and depending on the metal possess surface plasmon resonance, which arises in different colors of metal nanoparticles depending on their size and shape. Metallic nanoparticles have a very high interest in catalysis^{4, 6}, biomedical imaging^{13, 14}, drug delivery¹⁵ and energy storage^{11, 12}. Semiconductor nanoparticles, known as quantum dots or artificial atoms, are usually below 10 nm in size, comparable to Bohr diameter for exciton, and possess discrete energy levels due to quantum confinement of electrons. Semiconductor nanoparticles are being researched extensively for photovoltaics¹⁶, integrated electronics¹⁷⁻¹⁹ and biomedical imaging technologies²⁰⁻²².

Due to the high surface area and high surface energy of metal nanoparticles, they have become a very hot research topic in the field of catalysis. Nanoparticles in catalysis are usually synthesized from a metal salt, then treated with a reducing agent and are either stabilized by polymers such as PVP and CTAB or supported on oxides, charcoals and zeolites. These

nanoparticles can also be supported on Metal Organic Frameworks (MOFs), carbon nanotubes, graphene, organic membranes and they can be stabilized by ligands, ionic liquids and surfactants. Metal nanoparticles are often used for heterogeneous catalysis, where the catalyst is in a different phase than the reagent. Numerous reactions have been catalyzed with help of metal nanoparticles and some examples of metal nanoparticles being used in heterogeneous catalysis include oxidation reactions^{23, 24}, various hydrogenation reactions^{25, 26} as well as photocatalysis^{27, 28}, carbon cross coupling reactions^{29, 30} and Fischer-Tropsch synthesis^{31, 32}.

Catalyst increases the rate of the reaction by decreasing its activation energy without being consumed in the process. Because metal nanoparticles have a high surface area, they have a higher ratio of surface to volume atoms, thus providing the much needed active sites of the catalyst for the reagents. However, as a result of this ratio, metal nanoparticles have a high surface energy, which leads to aggregation into larger particles, decreasing their surface area and thus decreasing the active sites available for catalysis. To prevent aggregation, nanometer sized catalysts are affixed to a high surface area materials, such as zeolites, various metal oxides, MOFs, graphene and carbon nanotubes. Not only the high surface area supports prevent aggregation they can participate in catalysis by aiding metal nanoparticles affixed to them in catalysis. Such an effect between the catalyst and a support is referred as strong metal support interaction (SMSI) and is usually seen with metal catalysts dispersed on reducible oxide supports such as TiO_x, AlO_x, TaO_x, NbO_x^{33, 34}. Strong metal support interaction can also be seen in reverse situation - with metal oxides dispersed on the metal surface. This phenomenon is attributed to an electron exchange between the support and the catalyst which has shown to be very significant in several catalytic reactions^{34, 35}. Thus, catalyst supports have a dual role of

affixing nanoparticles and, depending on the nature of support, activating the catalyst affixed on them.

Recently, two different classes of support have gained a lot of interest: reduced graphene oxide (RGO) and Metal Organic Frameworks (MOFs). Reduced graphene oxide is a support that is synthesized by chemically³⁶ or physically reducing graphene oxide sheets, which still has some of the functional groups present on the surface of graphene. Reduced graphene oxide offers numerous advantages as a catalyst support such as large specific surface area of up to 2600 m²/g³⁷, high carrier mobility³⁸ of more than 200,000 cm² V⁻¹ s⁻¹, high elasticity and mechanical strength³⁹, functional groups on the surface of the sheets and carbon vacancies and defects, which offer anchoring sites for metal nanoparticles preventing their aggregation^{37, 40}. This material has been used extensively as an efficient support for photocatalysis of hydrogen gas evolution⁴¹, carbon cross coupling reactions, oxidation reactions, and dye degradation^{42, 43}. Palladium nanoparticles supported on RGO have shown excellent catalytic activity for various carbon cross-coupling reactions such as Suzuki-Miyaura, Heck and Sonogashira reactions and CO oxidation reactions.

Metal Organic Frameworks are an extensive class of crystalline materials consisting of organic linkers and inorganic nodes. MOFs not only possess a very large surface areas of up to 7,000 m²/g⁴⁴ they also have high porosity with 90% of volume being empty space⁴⁵ and a high degree of variability^{46, 47} due to relative easiness of changing linkers and nodes. Because nodes and linkers in MOFs can be changed, their porosity and internal surface can be tuned

respectively, resulting in new MOFs with different properties and functions. Due to their very large surface areas and unique ability to be fine-tuned, MOFs have been used extensively in catalysis as supports for metal nanoparticles^{4, 48-50} as well as catalyst materials⁵⁰⁻⁵³. Typical examples of MOFs being used as supports include oxidation reactions⁵⁴, hydrolysis reactions⁵⁵, biomimetic catalysis⁵⁶ and photocatalysis⁵⁷. Additionally, MOFs have been reported to act as catalysts with reactions occurring on the metal centers⁵⁸ and on the organic linkers⁵⁹. Incorporation of noble metal nanoparticles, such as palladium, has shown exceptional catalytic activity for carbon monoxide oxidation reactions as well as multiple carbon cross-coupling reactions such as Suzuki-Miyaura⁴⁸, Heck and Sonogashira⁴⁸ reactions.

In this work two different types of catalyst will be developed. Catalysts of palladium nanoparticles supported on SiO_x (Pd/SiO_x-RGO) for carbon cross-coupling reactions and palladium nanoparticles supported in UiO-67 MOF (Pd/UiO-67) for benzyl alcohol oxidation.

Carbon-carbon cross coupling reactions, catalyzed by palladium complexes, represent a very important branch of organic synthesis due to their possibility of synthesizing complex molecules by coupling hydrocarbons⁶⁰. Because of its importance in the area of drug development Akira Suzuki, Richard Heck and Ei-ichi Negishi were awarded a Nobel Prize in Chemistry for their work in palladium-catalyzed cross-coupling reactions⁶¹. Homogeneous catalysis was used extensively for carbon cross-coupling reactions; however problems arose with such an approach due to inability to efficiently separate the catalysts from the reaction products which essentially led to drug contamination and inability to recycle the catalyst for the reaction. Removing such catalyst from the pharmaceutical substance to passable concentration levels involves a costly purification process⁶². As a result, heterogeneous palladium catalysts would be deemed useful, due to their ability to be recycled and because of their much simpler separation process from the

pharmaceutical product and thus lower toxicity. Some of the commercially available heterogeneous catalysts are Pd/C and Pd/Al₂O₃ and have a turnover number (TON) of up to 36,000 for Suzuki, Heck and Sonogashira cross coupling reactions⁶². Dispersed palladium nanoparticles on different supports have been tested for various cross coupling reactions and have been reported in literature. Annapurna, et al⁶³ have successfully incorporated palladium nanoparticles into MIL 101 MOF and have been able to achieve up to 96% in yield for Sonogashira coupling under mild base conditions and they have managed to recycle their catalyst four times whilst still maintaining significant yield. Wang et al⁶⁴ reported 91% yield for Suzuki-Miyaura cross coupling under mild base conditions at 80 °C by using palladium nanoparticles encapsulated by polyethylene glycol (PEG) and supported on magnetic iron oxide core. Their magnetic nanoparticles were recycled up to 9 times without significant loss in catalytic power. Song et al⁶⁵, have successfully synthesized composite hydrogel from graphene and multiwall carbon nanotube encapsulated with palladium nanoparticles and have achieved 99% yield in Suzuki-Miyaura cross coupling of iodobenzene with phenylboronic acid under 15 minutes in mild base conditions. The composite hydrogel catalyst was recycled up to 6 times without significant loss in activity.

Oxidation of primary and secondary alcohols is a fundamentally important process both in academic research and industry⁶⁶⁻⁶⁸. Such chemical reactions, specifically oxidation of primary alcohols, produce aldehydes, ketones and carboxylic acids which are valuable both as fine chemicals⁶⁷ precursors for drugs⁶⁹, vitamins⁶⁹ and as intermediates⁶⁷ for the perfume industry due to their attractive aroma. Due to importance of this organic synthesis and its products, many chemicals have been used for alcohol oxidation such as chromates⁶⁹, manganese oxides⁶⁸, permanganates⁶⁸ and hypochlorites⁷⁰. However, these chemicals are toxic, corrosive and

hazardous carrying with them an additional cost of cleaning equipment and safe disposal. Thus, a more efficient and a safer, environmentally-friendly, alternative is deemed necessary^{71, 72}. One of the reagents used for “green chemistry” approach are hydrogen peroxide and molecular oxygen which have been used and provided excellent results^{72, 73}. Aerobic oxidation of alcohol by using molecular oxygen as a reagent has recently been of high interest due to its availability and cheap cost⁷¹. Multiple aerobic oxidation reactions have been carried out by different research groups using various types of catalysts and supports. Long et al⁷⁴, reported synthesizing nitrogen doped graphene sheets that were used to catalyze the oxidation of benzylic alcohols under atmosphere pressure oxygen in a reflux with yields of 99% and selectivities of 100% within 10 hours. Huang et al⁷⁵, synthesized gold-silver alloy nanoparticles stabilized by triblock copolymer (P123) and have achieved a turnover frequency (TOF) of 216 h⁻¹ with 2.8% conversion in 2 minutes. Solvent-free oxidation of benzylic alcohols reported by Zamani et al⁷⁶, have demonstrated 85% yield and 99% selectivity within 1.5 hour of reaction by using palladium nanoparticles supported on the iron oxide/amino acid composite particles. The catalyst has shown no significant decrease in yield after 7 reaction cycles with 100% selectivity for benzaldehyde. Yan et al⁷⁷, reported 27.8% conversion of benzyl alcohol into products with 96.5% selectivity for benzaldehyde over palladium nanoparticles affixed to organosilane-functionalized carbon nanotubes.

Herein we will focus the rest of the work on catalysis of carbon cross coupling reactions with palladium nanoparticles on RGO and benzyl alcohol oxidation on palladium nanoparticles embedded into Zr-based UiO-67 MOF.

CHAPTER 3

Experimental

3.1 Overview

The primary method to prepare the palladium nanoparticles is to synthesize its supports via laser irradiation (SiO_x/RGO supports) or via chemical method (UiO-67 MOF) followed by palladium precursor loading and its further reduction. The resulting solids are then washed and dried in the oven and purified before being characterized by XRD, UV-Vis, FTIR, Raman, XPS or tested for catalysis. GC-MS was used to test the conversion and selectivity for carbon cross-coupling and benzyl alcohol oxidation reactions. The following sections present and discuss the details of the experimental and reaction procedures.

3.2 Laser Vaporization Controlled Condensation (LVCC)

Laser Vaporization Controlled-Condensation (LVCC) is a technique that utilizes pulsed laser irradiation of a target sample and formation of nanoparticles from the vapor-phase inside the chamber⁷⁸⁻⁸⁰. The focused laser pulse ($t = 1\text{-}2\text{ ns}$) vaporizes the solid target, producing ions and atoms which grow into nanoparticles upon nucleation. LVCC chamber consists of two stainless steel plates, through which either liquid nitrogen or hot water circulates, separated by a quartz cell. The target, metal or powder pellet, is placed in the center on the lower steel plate and the chamber is filled with a carrier gas or gas mixture. Gas mixtures used in LVCC process can be inert (He, Ar) or the mixtures can be reactive (O_2 , H_2 , C_2H_4) to synthesize oxides, hydrogen terminated bonds, or carbides respectively. The gas mixture is a composition of inert or reactive gases. The upper steel plate can be cooled to less than $120\text{ }^\circ\text{C}$ by circulating liquid nitrogen and the bottom steel plate can be warmed up to $90\text{ }^\circ\text{C}$ by circulating hot water. Because of this large temperature gradient an upward convection is created forcing the deposition of nanoparticles on

the upper steel plate and this effect can be enhanced by using carrier gas under high pressures upwards of 1000 torr. Typical LVCC setup used for experiments is depicted in figure 1.

LVCC gives an optimal control of nanoparticle synthesis, where nanoparticle size can be adjusted by changing the temperature gradient and changing the pressure of the carrier gas. This process offers a unique, “green” chemical-free method of synthesis of nanoparticles. Composition of deposited nanoparticles can be adjusted by changing the composition of the irradiated target.

Using such technique nanoparticles are produced by condensation from the vapor phase that is formed inside the chamber. LVCC method involves the use of pulsed Nd:YAG laser to vaporize the target inside the chamber, which has a certain mixture of gases under specified pressure and temperature. The focused laser pulse ($t = 1\text{--}2$ ns, 4 Watts, 532 nm, 30 Hz) vaporizes the solid target, producing ions and atoms which grow into nanoparticles upon nucleation. The controlled temperature gradient produces convection flow inside the chamber allowing the particles to deposit on the upper steel plate. LVCC setup with relevant components is depicted in figure 1.

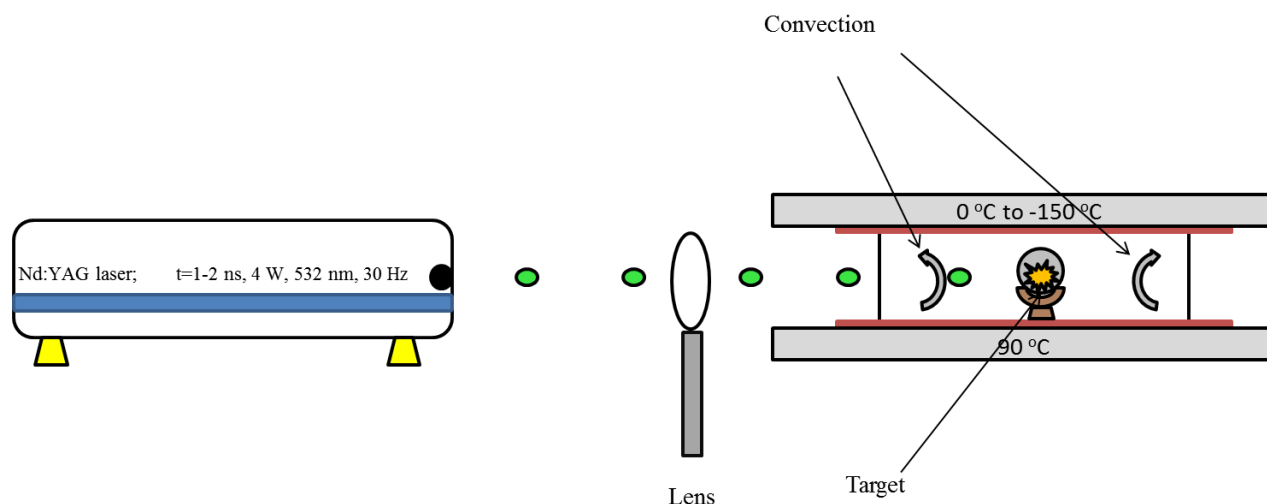


Figure 1. Experimental LVCC setup used to synthesize nanoparticles of controlled size.

The LVCC setup consists of two handmade stainless steel plates, separated by the quartz glass ring. The steel plates create temperature gradient by flowing liquid nitrogen into the upper steel plate cooling it below $-120\text{ }^{\circ}\text{C}$ and flowing hot water into the bottom steel plate to heat it upwards to $90\text{ }^{\circ}\text{C}$. The quartz ring is wrapped by a heating tape to prevent the condensation on the quartz glass, thus, removing contamination, reducing the laser light scattering and avoiding unnecessary side reactions inside the gas chamber. A solid target is set in the middle of the chamber on the bottom steel plate and the chamber is filled with an inert carrier gas, such as Helium, Argon or with a mixture of gases with a known composition (O_2 for oxides, H_2 for hydrogen terminated surface, CH_4 for carbides, etc.) with a pressure upwards of 1000 torr. The LVCC chamber is closely depicted in figure 2.

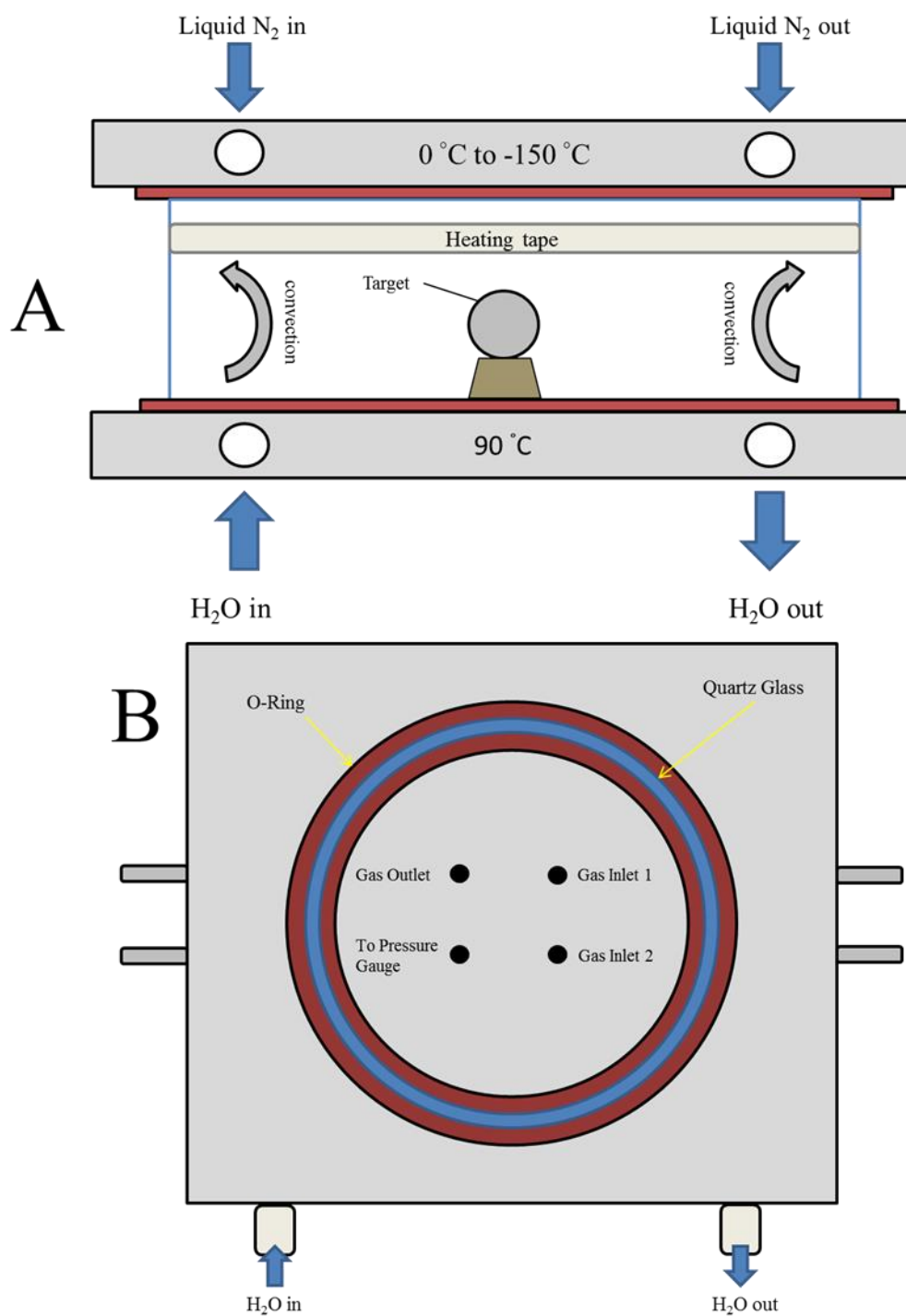


Figure 2. LVCC chamber from (A) side view and (B) top view with the upper steel plate removed for clarity purposes.

Vapor is generated by a high energy pulse from a second harmonic Nd:YAG laser (33-330 mJ/pulse) that is focused through the lens on the target. The focused laser spot is moved over

time to a new surface of the target to ensure reproducibility and uniformity of the catalyst supports deposited on the upper steel plate. When the laser pulse hits the target, atoms and ions are ejected into the vapor phase of the chamber where interaction between the gas and the atoms starts taking place. Maximum supersaturation occurs above the surface of the target due to the target being located in the middle at half the height of the chamber. Because of this, supersaturation can be controlled by adjusting the temperature gradient of the chamber, therefore by changing the temperature gradient - different size of nanoparticles can be formed. Another role of the temperature gradient is creating the convection current, which helps to remove the particles from each other, thus preventing their further growth and producing smaller particles deposited on the upper steel plate. The higher the temperature of the gradient, the stronger the convection current and thus the smaller the nanoparticles deposited on the plate. With a possibility to control the pressure chamber, laser power and temperature gradient it is possible to produce condensing nanoparticles of desired size.

3.2.1 Laser Assisted Synthesis of SiO_x Nanoparticles

A silicon chip (99% purity) was placed into LVCC chamber under 20% H₂/ 80% He by volume at total pressure of 800 torr. The top plate was cooled down to -40 °C by circulating liquid nitrogen through the top plate and the bottom plate was heated up to 90 °C by circulating hot water through it. The silicon chip was irradiated by Nd:YAG 532 nm laser for 1-1.5 hours at power of 4.0 watts with repetition rate of 30 Hz. After terminating the laser irradiation, the LVCC chamber was warmed up and the resulting brown powder was collected and analyzed.

3.2.2 Laser Assisted Synthesis of SiO_x/Si-RGO Supports

A micron powder of silicon was taken and thoroughly mixed in mortar and pestle together with Graphite Oxide (GO) until it became homogeneous. Afterwards, the resulting

powder was subject to a hydraulic press at 6.0 MPa for 2 minutes and the resulting pellet was removed from the press and put into the LVCC chamber. The LVCC chamber was purged multiple times and filled with 800 torr of inert Helium gas (99.9% purity) and the upper plate was cooled down to -40 °C while the bottom plate was heated at 90 °C. The Si pellet was irradiated by pulsed Nd:YAG 532 nm laser at 30 Hz repetition rate with an average power of 4 watts until the pellet structurally failed. Upon warming up the LVCC chamber, the resultant powder was collected from the top plate and analyzed or tested for catalysis reactions.

3.2.3 Incorporation of Palladium Nanoparticles into SiO_x/RGO supports

The nano-sized support particles were collected from LVCC system and then stirred in a water solution for 20 minutes followed by an injection of Pd(NO₃)₂ solution with a subsequent 30 minute stirring. After the solution became well dispersed, 40 µL of Hydrazine Hydrate was injected into the solution and was microwaved in a conventional oven (2.45 GHz) operating at 600-1000 W for 30 seconds. The resulting solution had a deep black color and was dried in the oven overnight at 80 °C.

3.3 Laser Irradiation In Solution

3.3.1 Chemical Synthesis of UiO-67 Metal-Organic Framework

The UiO-67 MOF was prepared following a synthetic procedure reported by Katz⁸¹ and co-workers. In a typical synthesis, 67 mg of ZrCl₄ powder and 0.5 mL of concentrated HCl together with 15 mL of Dimethylformamide (DMF) were added to a flask and sonicated for 20-30 minutes to dissolve all of the ZrCl₄. Afterwards, 90 mg of 4,4-biphenyl dicarboxylic acid was added to the mixture with the remainder of DMF and sonicated for another 20-30 minutes until all the ligand was dissolved in the solution. The resulting mixture was capped and put in the oven at 80 °C overnight. Afterwards, the solution was purified by washing and centrifuging twice with DMF and twice with EtOH and the

resulting white solid was placed in the vacuum oven at 100 mtorr pressure at 100 °C to eliminate all the vapors and gases adsorbed to the surface of the porous framework.

3.3.2 Preparation and Incorporation of Palladium Nanoparticles into the UiO-67 Framework

For the preparation of palladium nanoparticles, first, UiO-67 powder was dispersed in a test tube filled with ethanol and sonicated for 20 minutes. Next, a palladium precursor $\text{Pd}(\text{NO}_3)_2$ in HCl salt was injected into the solution resulting in transformation of solution color from white to pale yellow. The resulting mixture was stirred vigorously for 10-15 minutes before laser irradiation. The solution in the test tube was irradiated by pulsed Nd:YAG laser with repetition rate of 30 Hz, 532 nm, 200 mJ/pulse for 15 minutes. The resulting mixture changed its color from pale yellow to dark grey due to reduction of palladium from +2 to 0 oxidation state. The resulting solution was washed and centrifuged two times with EtOH at 10 000 rpm and was left in the oven overnight at 80 °C. Figure 3 depicts the experimental setup for laser irradiation of UiO-67 in solvent.

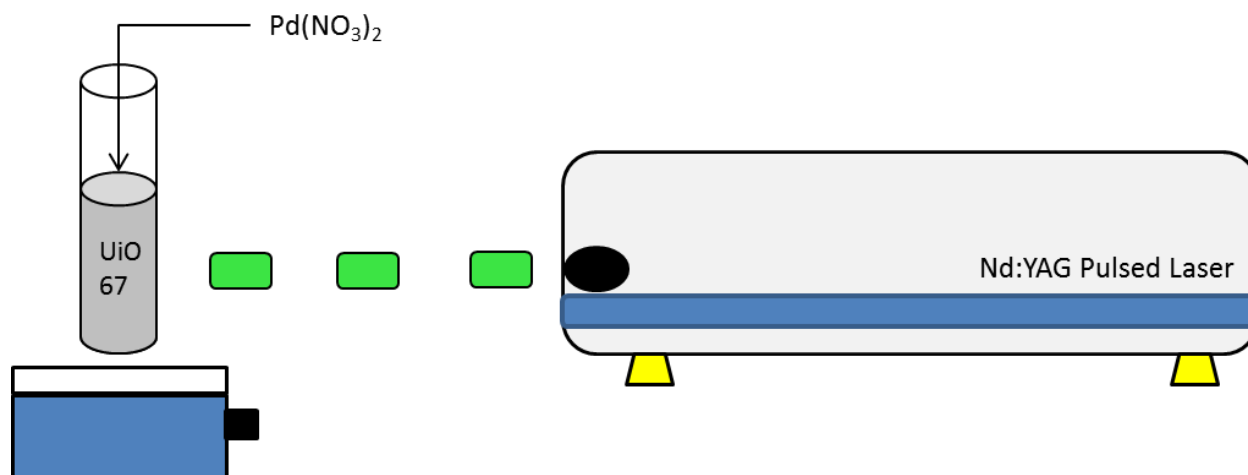


Figure 3. Incorporation and reduction of palladium precursor in UiO-67 during pulsed laser irradiation.

3.4 Heterogeneous Catalysis

3.4.1 Carbon Cross Coupling Reactions in Microwave Reactor

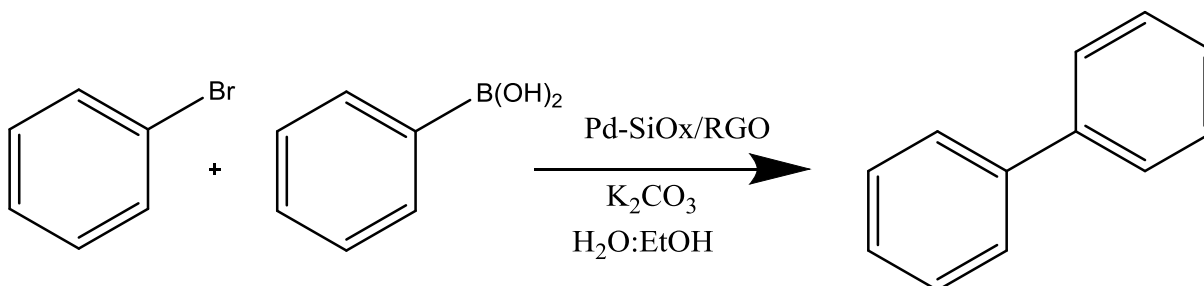


Figure 4. Suzuki-Miyaura Cross-Coupling reaction with the use of $\text{Pd/SiO}_x\text{-RGO}$ catalyst.

Performing the carbon cross-coupling reactions, bromobenzene (50 mg, 0.32 mmol) was dissolved in a mixture of 4 mL of $\text{H}_2\text{O:EtOH}$ (1:1) and placed in a 10 mL microwave tube. Afterwards, phenyl boronic acid (47 mg, 0.38 mmol) and potassium carbonate (133 mg, 0.96 mmol) were added. Subsequently $\text{SiO}_x\text{-RGO-Pd}$ catalyst was added, and the tube was sealed and stirred at room or 80 °C temperature depending on the catalyst type. The aliquots from the reaction were taken in 5 minute intervals and diluted with 10 mL of acetonitrile and injected into GC-MS instrument for product characterization. Percent conversion of the products was calculated based on the bromobenzene consumption throughout the reaction by means of GC-MS. Figure 4 depicts the reaction scheme of bromobenzene with phenylboronic acid to produce biphenyl.

3.4.2. Oxidation of Benzyl Alcohol in the Autoclave Reactor

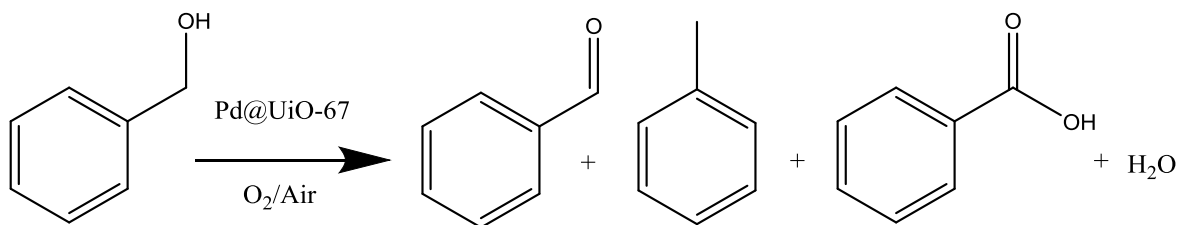


Figure 5. Benzyl alcohol oxidation over palladium nanoparticles supported on UiO-67 MOF.

Detailed procedure for benzyl alcohol oxidation was described by Miedziak⁸². Briefly, the autoclave reactor with a Teflon chamber was charged with 1.0 mg of palladium nanoparticles supported on the UiO-67 framework and 20.0 mL of benzyl alcohol (99%). The resulting autoclave was purged 5 times with carrier oxidant gas and set to appropriate pressure and temperature with a stirring speed of 1000 revolutions per minute (rpm). Throughout the reaction progress, 5 sample aliquots were drawn at 0.5, 1, 2, 3 and 4 hour intervals and analyzed through Varian GC-MS 6890N for the catalytic conversion of benzyl alcohol. Progress of the reaction was monitored by the consumption of benzyl alcohol. Figure 5 depicts the reaction of benzyl alcohol oxidation into its products.

CHAPTER 4

4 Laser Assisted Synthesis Results and Discussion

4.1 Characterization of SiO_x Nanoparticles

4.1.1 UV-Vis Spectroscopy

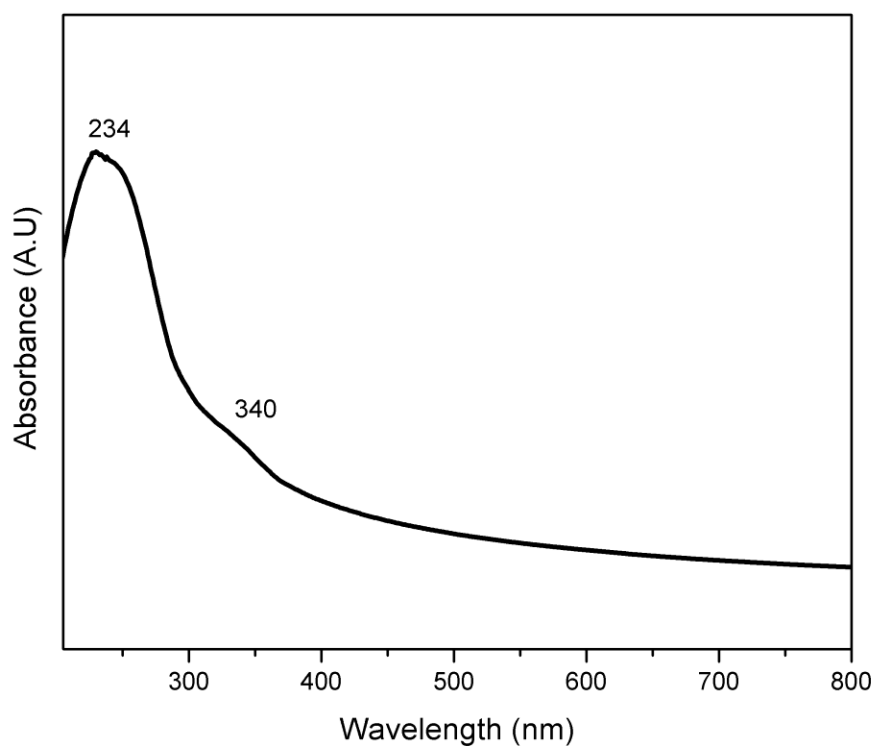


Figure 6. UV-Vis spectrum of silicon nanoparticles in methanol solvent synthesized by LVCC process.

Figure 6 depicts the UV-Vis absorbance of surface-oxidized silicon nanoparticles suspended in methanol solution. The yellow absorption tail extending from 400 nm across the visible and the strong absorption from about 250 to 370 nm is associated with indirect band gap transition in silicon⁸³. Relative to the bulk silicon, the UV-Vis absorbance of LVCC silicon nanoparticles are blue shifted due to quantum confinement effect, suggesting that the silicon core

is less than 4.3 nm in diameter. The particle size might be larger than 4.3 nm and still exhibit quantum confinement effects due to the passivating oxide layer that develops right after the silicon nanoparticles are exposed to ambient atmosphere. Hamad *et al*⁸⁴ have synthesized silicon nanoparticles by ablating bulk silicon with femtosecond laser pulses in acetone solution and have observed broad peaks from 400 to 800 nm corresponding to various sizes of silicon nanoparticles. A sharp peak was observed around 300 nm corresponding to average size of 4 nm for silicon nanocrystals. Holmes⁸⁵ and co-workers have synthesized monodisperse silicon nanoparticles by thermally degrading diphenylsilane at high pressure and temperature in octanol. The silicon nanoparticles produced were in a size range from 1.5 to 4.0 nm in diameter with absorption peak around 260 and 270 nm respectively. The 1.5 nm silicon nanocrystals were blue-shifted in comparison to the larger nanoparticles and had discrete optical transitions in the UV-Vis spectra owing to its quantum confinement. Wu⁸⁶ has synthesized fluorescent silicon quantum dots by reducing 3-aminopropyl trimethoxysilane with sodium ascorbate via hydrothermal process. The resulting silicon quantum dots were monodisperse with a mean size of 4.0 ± 0.7 nm. The UV-Vis spectrum of fluorescent silicon quantum dots displayed multiple peaks at 270, 300 and 360 nm. The 270 nm peak was attributed to 4.4 eV direct bandgap L-L transition, peak at 300 nm corresponded to $\Gamma_{25}-\Gamma_2$ direct bandgap transition with energy of 4.13 eV and the shoulder at 360 nm was associated with $\Gamma_{25}-\Gamma_{15}$ direct transition with energy of 3.4 eV. Similar UV-Vis was obtained for silicon nanoparticles produced by Afshani⁸⁷ and co-workers using LVCC method where strong absorption from 240 nm across the visible region was attributed to indirect bandgap of silicon.

Based on absorption spectra in figure 6, it is possible to calculate the bandgap of silicon nanoparticles synthesized by LVCC process and results in approximately 1.78 eV⁸³. Similar UV-Vis absorbance spectrum was reported by Holmes where they have synthesized 1.5 and 2.5-4.0 nm silicon quantum dots and have observed peaks at 260 nm with a shoulder at 350 nm.

4.1.2. FTIR Spectroscopy

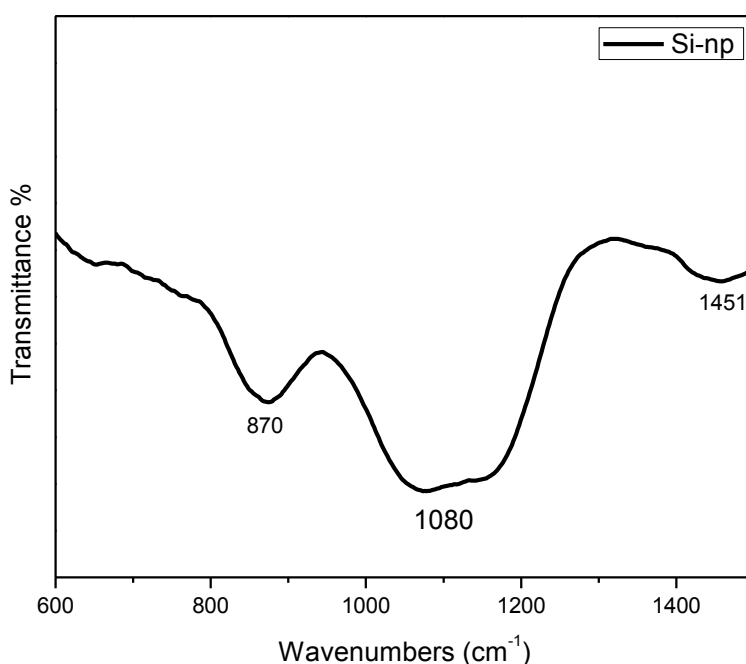


Figure 7. FTIR Spectrum of silicon nanoparticles synthesized by LVCC method.

Figure 7 depicts the FTIR spectrum of surface-oxidized silicon nanoparticles from LVCC chamber. The band at around 870 cm⁻¹ is attributed to in-plane bending of Si-O-Si bonds⁸⁸. The band at 870 cm⁻¹ is not exact and can be shifted depending on the degree of SiO_x plane stress⁸⁸. The band at 1080 cm⁻¹ corresponds to in-plane asymmetric stretching mode of Si-O-Si bond and are often seen in thin films of amorphous SiO₂^{89, 88, 90}. Bands at 870 cm⁻¹ and 1080 cm⁻¹ vary in intensity depending on the content of oxygen present in the LVCC chamber. Passivating

SiO_x layer covers the silicon nanoparticles as soon as the chamber is open, thus rendering surface oxidation unavoidable. The passivating layer of SiO_x is about 1-2 nm thick, preventing further oxidation of the Si nanoparticle core. Introducing oxygen gas into LVCC chamber will increase the Si-O-Si bands in transmittance intensity. The band at 1451 cm⁻¹ corresponds to stretching vibration of Si-C bond⁹⁰ which could originate from remaining carbon dust in the chamber. The band is weak in transmittance intensity, signifying low content of carbon contamination in the sample. LVCC process provides web-like agglomerations⁹¹ of silicon nanoparticles that possess a high surface area of up to 460 m² g⁻¹.

Similar FTIR spectra of silicon nanoparticles have been reported by several groups. In silicon quantum dots synthesized by Wu⁸⁶ and his co-workers several bands have been located in the FTIR spectrum. Bands between 1000 and 1200 cm⁻¹ were ascribed to vibrational stretching of Si-OR as well as to silicon-oxygen double bond and bands from 1300 to 1600 cm⁻¹ were attributed to symmetric bending of Si-CH₂. A few other bands from 600 to 800 cm⁻¹ and 1579 to 3356 cm⁻¹ originated from bending and stretching vibration of single nitrogen-hydrogen bond. A peak at 2931 cm⁻¹ was assigned to O-H vibration. Holmes⁸⁵ has reported peaks ranging from 1085 to 1200 cm⁻¹ corresponding to Si-O-Si stretch. He also reported a strong band between 450 and 520 cm⁻¹ corresponding to transverse optical phonon of silicon. A few other bands were observed from 2800 and 2900 cm⁻¹ corresponding to methyl stretching modes, arising from the capping agent used for silicon nanoparticles. Peaks from 750 to 850 cm⁻¹ and from 2100 to 2300 cm⁻¹ were attributed to Si-H stretching modes. Umezu⁹² and co-workers have synthesized silicon nanoparticles by irradiating bulk silicon target with a 4th harmonic Nd:YAG laser in hydrogen gas atmosphere. The resulting silicon nanoparticles had bands around 2100 cm⁻¹ corresponding

to Si-H and Si-H₂ bonds. Heintz *et al* reported several peaks for their blue luminescent silicon nanoparticles passivated with alkyl groups. Strong peaks ranging from 2800 to 3000 cm⁻¹ were attributed to C-CH₃ stretching along with C-H vibrational stretches around 1370 and 717 cm⁻¹ indicating that capping agents' presence on the surface of silicon nanoparticles. Additional peaks at 796, 1257 and 806 cm⁻¹ were attributed to Si-C bonds, and broad band from 1000 to 1120 cm⁻¹ was ascribed to Si-O bond.

4.1.3 Photoluminescence

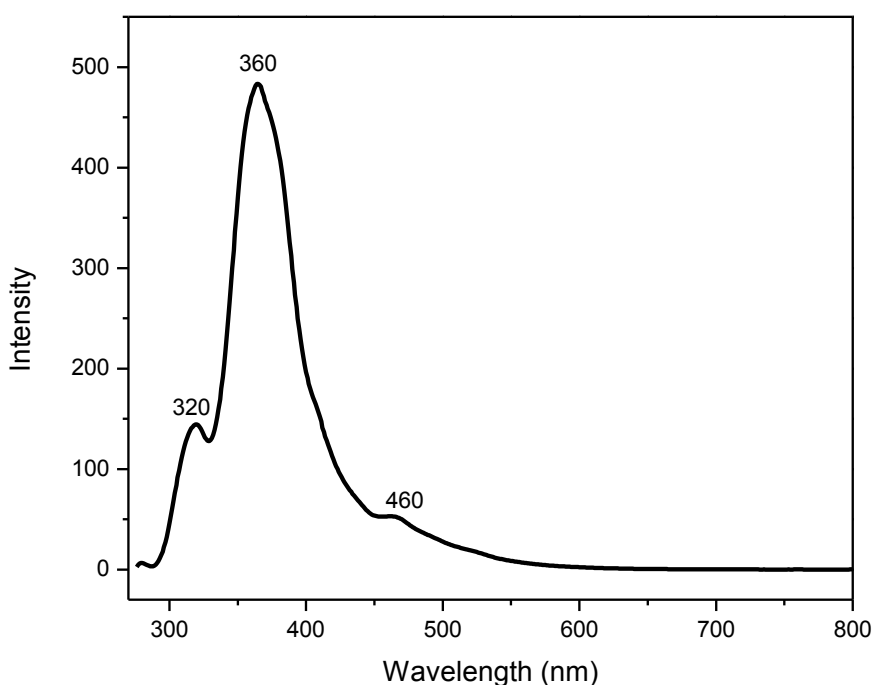


Figure 8. Photoluminescence of silicon nanoparticles synthesized by LVCC method.

Figure 8 depicts photoluminescence of silicon nanoparticles suspended in methanol solution. The excitation wavelength used was 266 nm and produced a prominent peak at 360 nm corresponding to 94 nm Stokes shift with shoulders at 320 and 460 nm. Bulk silicon has no

photoluminescent properties due to its narrow and indirect band gap⁹³. Silicon's direct bandgap is 3.3 eV, whereas the indirect bandgap is only 1.1 eV. To access that conduction minimum band of silicon at 1.1 eV a phonon coupled with a photon excitation is required. However, as silicon approaches the 4.3 nm Bohr exciton radius size the indirect band gap becomes more easily accessible due to discrete energy levels and photon energy alone is sufficient to create electron-hole pairs. As such, photoluminescence in near IR and UV-Visible region can be observed. The shoulders in figure 8 represent photoluminescent peak of silicon and can be the consequence of size quantization of silicon nanoparticles⁹³.

Silicon nanoparticles, depending on their size, excitation wavelength and their passivating agents, have emission spectra all over the visible range. Lam⁹³ has synthesized ultrafine silicon through ball milling process resulting in 6 nm sized particles with 1 nm of passivating oxide layer. Lam and co-workers have excited silicon nanoparticles with 514.5 nm argon laser and have observed 7 discrete peaks ranging from 650 to 950 nm. It was reported that those peaks corresponded to porous silicon with energies ranging from 1.89 to 1.38 eV. It was speculated that the rise of multiple discrete peaks was due to silicon's quantum confinement effect, where energy levels would become discrete if the silicon core was below its Bohr radius of 4.3 nm. Riabinina⁹⁴ and co-workers have synthesized nanometer sized silicon particles by reactive laser ablation method in oxygen atmosphere. The synthesized particles ranged in size from 2 to 16 nm and have observed photoluminescence peaks ranging from 750 to 950 nm respectively. The photoluminescence intensity increased with rising oxygen pressure, due to decrease in radiation-less Auger recombination, decreased particle core size and increased oscillator strength. The peak shifts in photoluminescence were attributed to the size of the silicon

nanocrystals where 750 nm photoluminescence was attributed to 1.9 nm particles and 950 nm photoluminescence peak was ascribed to 7 nm particles.

Heintz⁹⁵ and co-workers demonstrated photoluminescence of silicon nanoparticles ranging from 380 to 500 nm with excitation light from 280 to 440 nm respectively. They have reported that photoluminescence emission maximas shift with higher wavelength of the excitation light. Furthermore, the red-shift in their emission spectra were caused by larger silicon nanoparticles present in the solution. Heintz has described that the luminescence of silicon at around 360 nm is ascribed to silicon nanoparticles with average size of 2 nm. The emission spectra of LVCC produced silicon nanoparticles agrees well with Rosso-Vasic⁹⁰ reported values.

4.1.4 Raman Spectroscopy

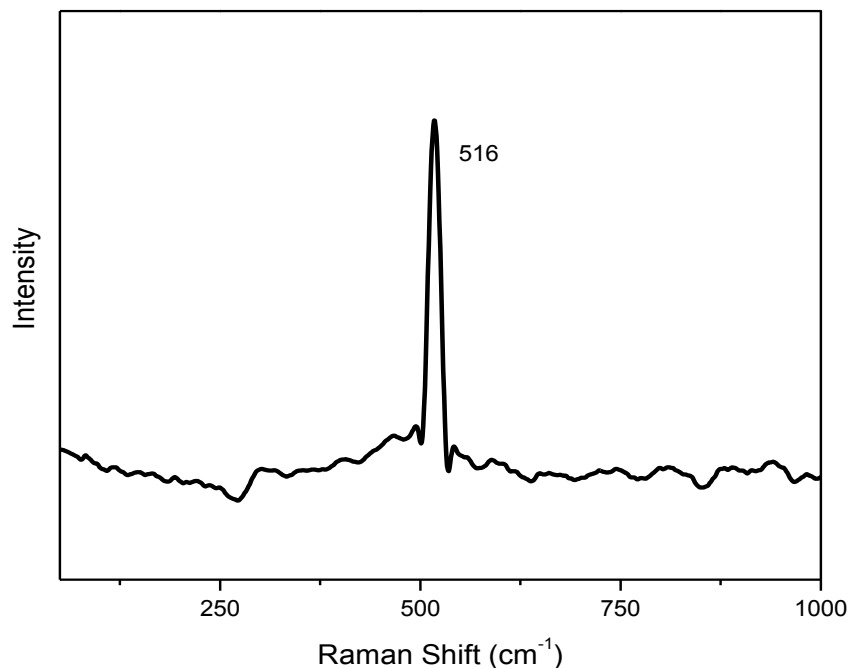


Figure 9. Raman spectrum of surface-oxidized silicon nanoparticles synthesized by LVCC method.

Figure 9 depicts Raman spectrum showing a sharp peak around 516 cm^{-1} , corresponding to the Raman allowed transverse optical (TO) phonon⁹⁶⁻⁹⁸. Optical phonon is a quantized lattice vibration and for microcrystalline silicon it is usually displayed around $480\text{-}520\text{ cm}^{-1}$. Depending on the size of silicon nanoparticles, Raman scattering peaks can be shifted accordingly. For example, Raman shifts of $520, 517, 510, 485$ and 480 cm^{-1} correspond to $22, 14, 10, 8$ and 7 nm size silicon nanoparticles respectively^{88, 97, 99}. Based on the literature published and the peak position, the average particle size of silicon nanoparticles is approximately 14 nm . The Raman peak of silicon nanoparticles blue shifts if more oxygen is present during the LVCC process⁷⁸.

Similar Raman spectra of silicon nanoparticles have been published in literature. Lam⁹³ reported Raman scattering peak around 520 cm^{-1} corresponding to optical phonon of silicon. Line broadening was observed at the base of the peaks which was attributed to small size of silicon nanocrystals from ball milling process. Interestingly, they have not observed a peak around 520 cm^{-1} for bulk silicon. Umezu⁹² reported similar Raman scattering peaks for silicon appearing around 520 cm^{-1} and increasing in intensity with higher pressure of hydrogen gas during the synthetic procedure. Hamad⁸⁴ and co-workers measured Raman scattering of their silicon nanoparticles prepared by femtosecond laser ablation. Peaks were measured at 484 and 512.3 cm^{-1} corresponding to amorphous and crystalline silicon nanoparticles respectively. Furthermore, it was observed that with decreasing size of silicon nanoparticles, the peak would broaden at its base and shift to lower wavenumbers.

4.1.5 Powder X-Ray Crystallography

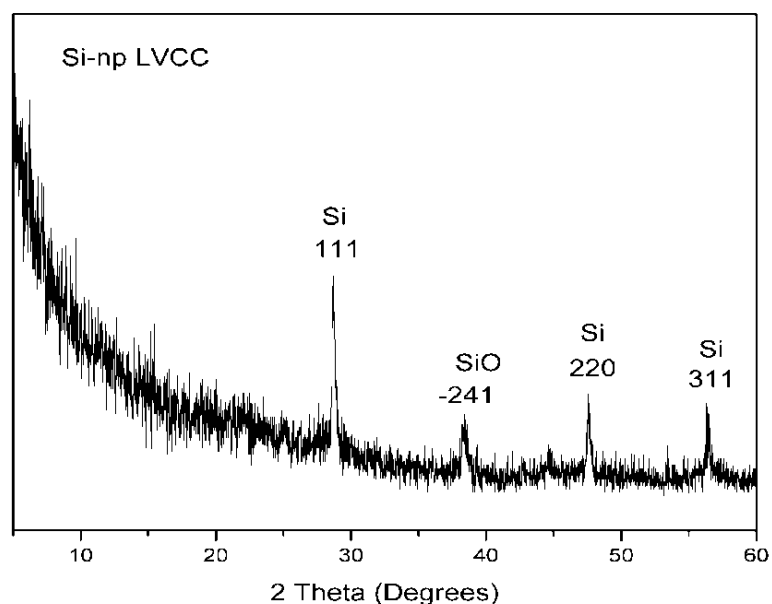


Figure 10. Powder X-ray diffraction of silicon nanoparticles synthesized by LVCC method.

Figure 10 depicts the crystallinity of silicon nanoparticles synthesized through LVCC process, where the spectrum shows crystalline silicon lines at 29° , 39° , 48° and 57° that correspond to 111, -241, 220 and 311 planes respectively. Due to the small size of silicon nanoparticles⁹⁴ synthesized by LVCC process, line broadening can be seen on diffraction patterns. Line -241 corresponds to SiO_x surface oxide layer that develops on the surface of silicon nanoparticles after LVCC process. Silicon nanoparticles due to their very small size are highly reactive and easily get oxidized by ambient air after opening LVCC chamber. The passivating oxide layer is 1-2 nm thick and serves as a protecting cap from further oxidation of silicon nanoparticles. The powder x-ray diffraction pattern matches well with what has been published in literature¹⁰⁰.

Similar x-ray diffraction patterns have been published in literature. Riabinina⁹⁴ *et al* have synthesized silicon nanocrystals by employing pulsed laser deposition of bulk silicon in oxygen atmosphere and further annealing it. The resultant silicon nanoparticles ranged in sizes from 2 to 16 nm and x-ray diffraction patterns have showed a strong line at 29° corresponding to 111 plane of silicon. Additionally, it was reported that peak broadening of diffraction pattern was attributed to presence of silicon nanocrystals. The size of nanocrystals was calculated from diffraction pattern corresponding to particles of 4 and 11 nm in size. Prosini¹⁰⁰ and co-workers have synthesized silicon nanoparticles supported by laser driven aerosol synthesis and have anchored them on reduced graphene oxide. X-ray diffraction patterns have been taken and peaks at 28.4, 47.3 and 56.1° corresponded to silicon lines 111, 220 and 311, which is very similar to our results. Using Scherrer's equation was applied to determine the particles size of silicon and it turned out to be between 28.4 to 55.8 nm in diameter. X-ray diffraction patterns were slightly broadened at its base and that was attributed to the nanometer size of the silicon crystals.

4.1 Characterization of SiO_x -RGO support

4.2.1. FTIR Spectroscopy

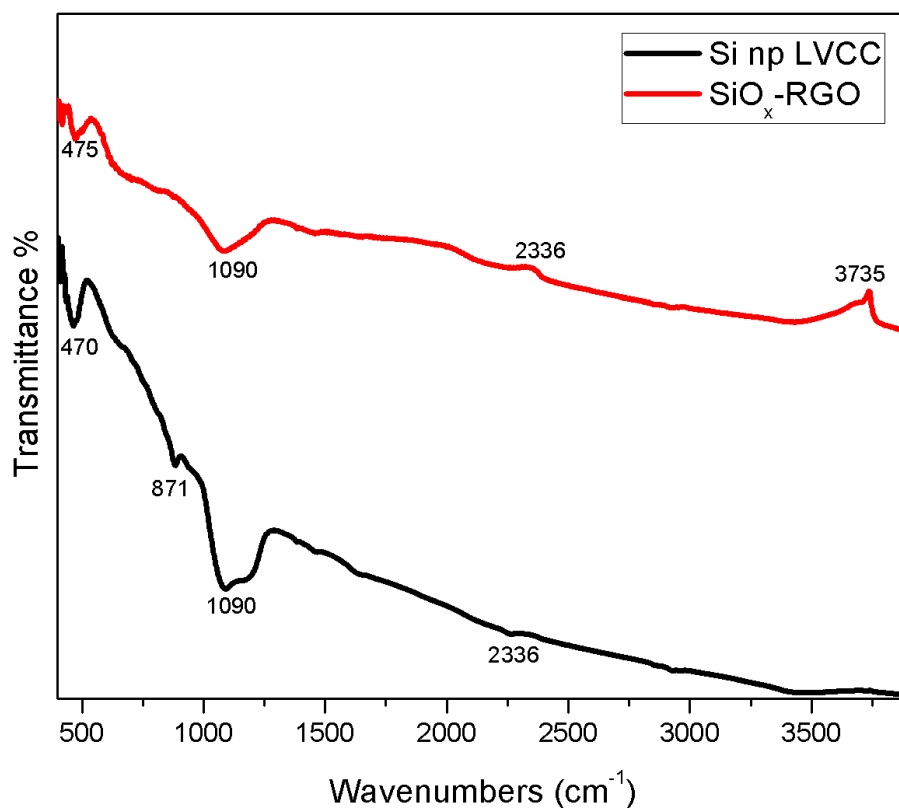


Figure 11. FTIR spectrum of Si nanoparticles (black) and SiO_x -RGO support (red).

Figure 11 depicts the FTIR spectrum of SiO_x -RGO support and Si nanoparticles alone for comparison. Peak around 470 cm^{-1} is attributed to transverse optical (TO) phonon of silicon. Peak at 871 cm^{-1} represents the in-plane bending of Si-O-Si bonds and can be shifted depending on the stress of SiO_x planes. A strong band at 1080 cm^{-1} is observed corresponding to asymmetric stretching mode of Si-O-Si bond. Small peaks around 2330 cm^{-1} represent the Si-H stretching modes. Peak around 3735 cm^{-1} represents the Si-OH stretching and is only present on

the SiO_x-RGO support possibly due to presence of functional –OH groups on the surface of graphene sheets.

4.2.2 Powder X-ray Crystallography

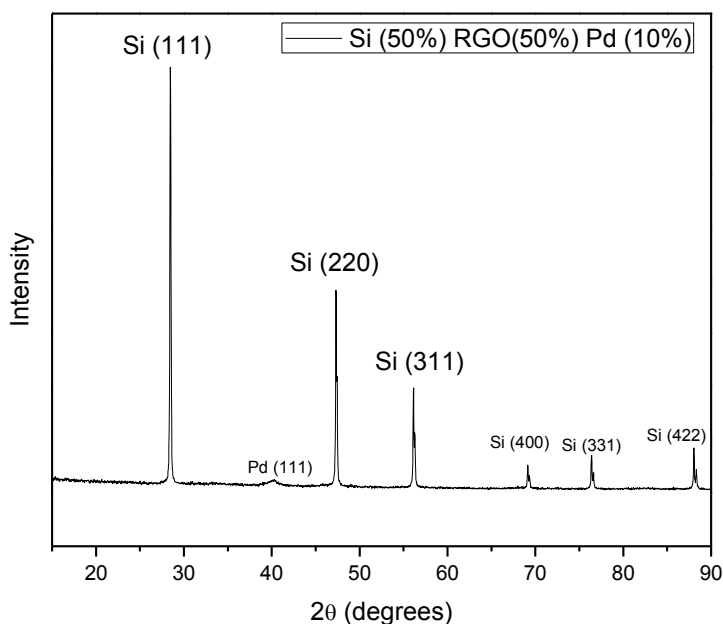


Figure 12. Powder XRD pattern of Si(50%) RGO(50%) support with 10 % by weight of palladium nanoparticles deposited on the support.

Figure 12 illustrates the powder x-ray diffraction patterns of SiO_x-RGO support loaded with palladium nanoparticles. Silicon lines 111, 220, 311, 400, 311 and 422 can be seen at 29, 47, 56, 69, 76 and 88° respectively. A small palladium line 111 at 40° can be seen due to insignificant presence of palladium in the sample. Palladium has more lines corresponding to its crystallinity, however due to small amount of palladium present in the sample, only the strongest line at 111 appears on the diffraction pattern. The powder x-ray diffraction of Si lines agrees well with published literature.

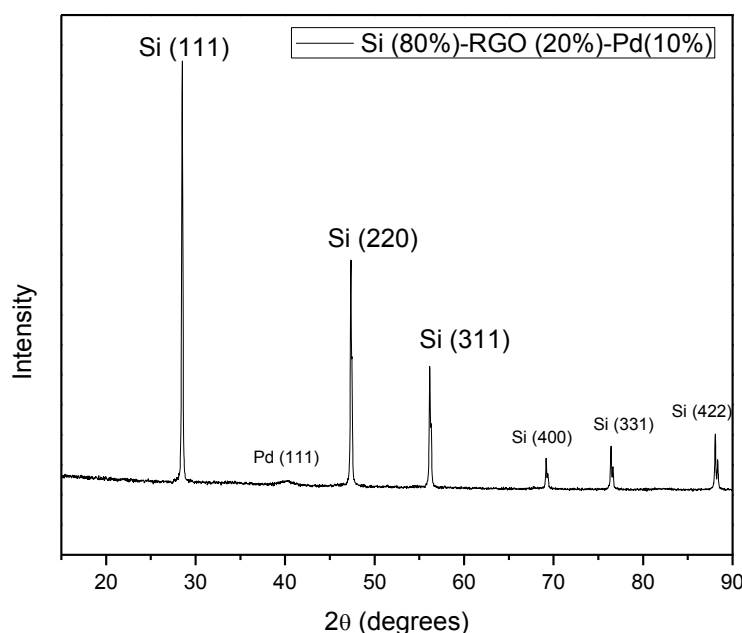


Figure 13. Powder XRD pattern of Si(80%) G(20%) support with 10 % by weight of palladium deposited on the support.

Figure 13 depicts x-ray diffraction patterns of Si-G support with palladium nanoparticles supported on it. The composition of support is slightly different – more silicon present by weight compared to reduced graphene. Silicon lines 111, 220, 311, 400, 311 and 422 appear at 29, 47, 56, 69, 76 and 88° respectively. Small palladium line 111 is present at 40° indicating successful deposition of palladium nanoparticles on the surface of the support. The peaks of silicon and palladium in particular are broadened at its base due to the small crystalline size of the particles present in the sample. Similar results have been published in literature. Nasrollahzadeh¹⁰¹ reported synthesis of palladium supported reduced graphene oxide for reduction of nitroarenes. Upon measuring the x-ray diffraction pattern, peaks at 10.2 and 23.0° were attributed to reduced graphene oxide lines of 001 and 002 respectively. Palladium peaks were observed at 40.1, 47.0, 68.1 and 82.0° and its peaks were slightly broadened due small particle size (18.2 nm).

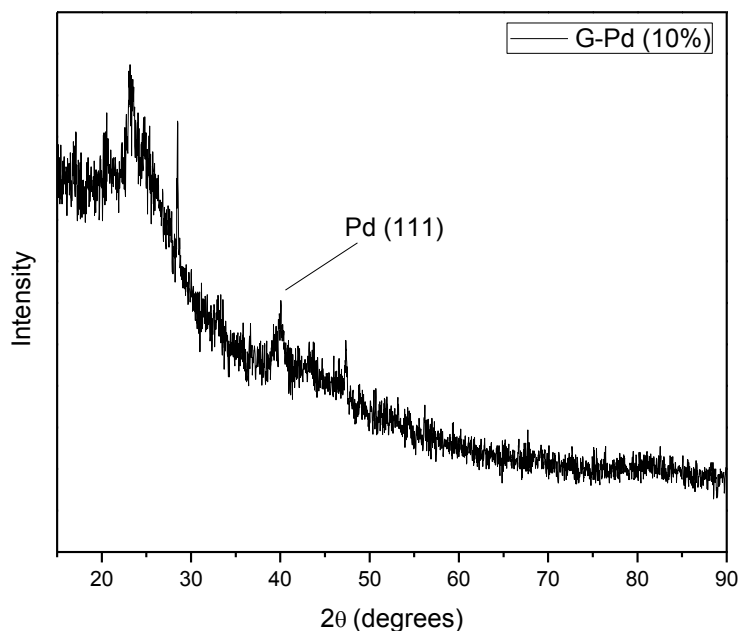


Figure 14. Powder XRD of reduced graphene with palladium nanoparticles deposited on its surface.

Figure 14 depicts powder x-ray diffraction of palladium nanoparticles supported on reduced graphene oxide. High background noise is attributed to low presence of carboxylic or carbonyl groups on the surface of reduced graphene sheets. Broadened palladium line 111 is observed at 40° , indicating low presence of palladium supported on reduced graphene sheet and small size of palladium particles.

Nasrollahzadeh¹⁰¹ and co-workers reported synthesis of palladium supported reduced graphene oxide for reduction of nitroarenes. Upon measuring the x-ray diffraction pattern, peaks at 10.2° and 23.0° were attributed to reduced graphene oxide lines of 001 and 002 respectively. Palladium peaks were observed at 40.1° , 47.0° , 68.1° and 82.0° attributing to 111, 200, 311 and 222 planes of its face centered cubic structure. The palladium peaks showed slight broadening due to small size (18.2 nm) of palladium nanoparticles.

4.2.3 X Ray Photoelectron Spectroscopy

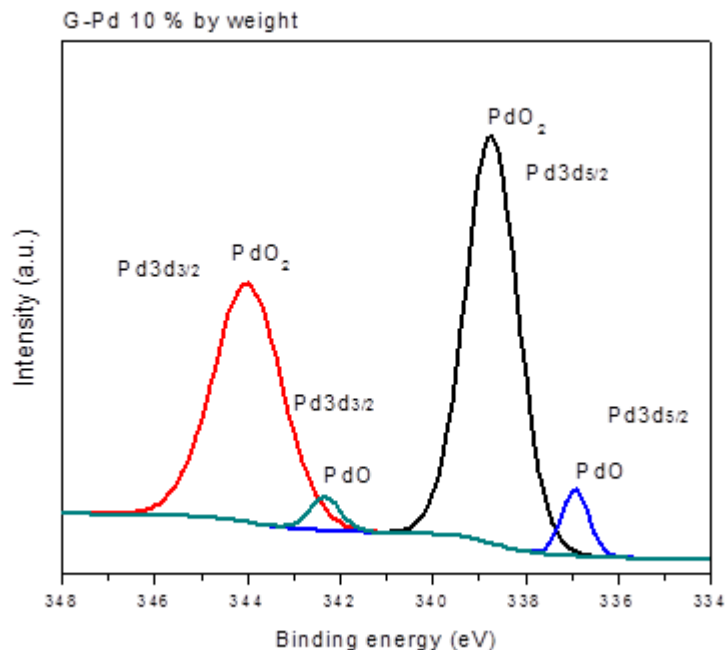


Figure 15. XPS binding energies of palladium in G-Pd (10%) sample. XPS accurately determines the oxidation state of palladium on the support. Palladium +2 and +4 oxidation states are evident from the binding energies. The XPS image was obtained by Julian Bobb.

Figure 15 depicts the binding energies of palladium on graphene-palladium sample. The binding energy of 337 eV and 342.5 eV correspond to +2 oxidation state of palladium, whereas binding energies of 338.5 eV and 343.5 eV correspond to +4 oxidation state of palladium. These oxidation states of palladium were attributed to the high ratio of surface to volume atoms, thus making the oxidation from ambient atmosphere unavoidable. The other possible cause for such oxidation states could be attributed to the drying process during the preparation of the catalyst. After introducing palladium nitrate salt and proceeding with microwave irradiation, the mixture of support and freshly prepared palladium nanoparticles is placed in the oven in ambient atmosphere. Elevated temperatures during drying process of the catalyst could increase the speed of oxide layer growth on palladium nanoparticles.

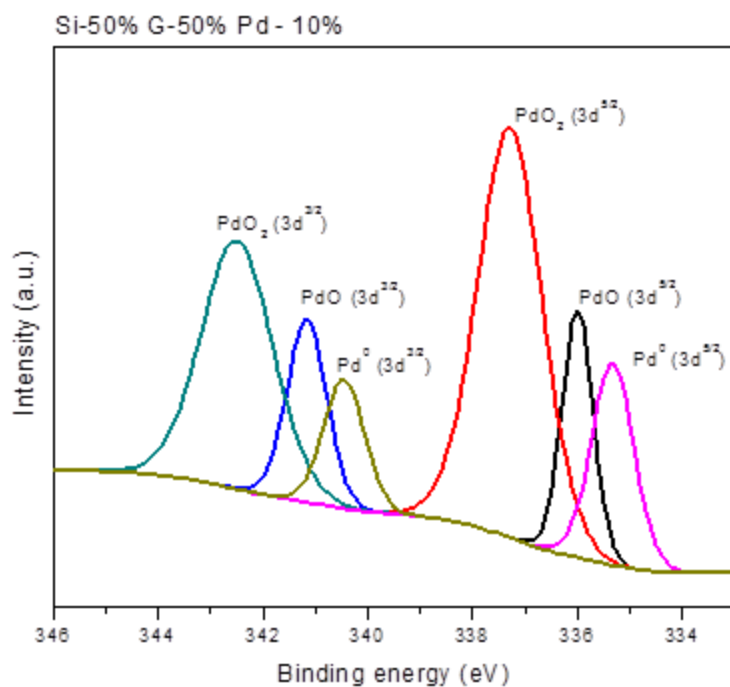


Figure 16. XPS spectrum of Pd/SiO_x-RGO showing the oxidation states of palladium catalyst. The XPS image was obtained by Julian Bobb.

Depicted in figure 16 is the XPS spectrum of palladium on SiO_x-RGO supports. Multiple oxide peaks such as PdO₂ and PdO corresponding to 342.7 eV and 341.1 eV respectively can be seen. Such oxide passivating layer could form upon drying process after reduction procedure of palladium precursor salt in the microwave oven. Due to nanoparticle's high surface to volume ratio of atoms, oxide layer could easily form overtime on top of the particles. Despite prominent palladium oxide peaks, palladium 0 can be seen at 340.5 eV and 335.5 eV. Both oxidized and reduced species of palladium play a significant role in carbon cross-coupling reactions in transmetallation and oxidative addition steps. Highest intensity peaks are seen for Pd. Such multiple oxidation peaks can be explained by forming a passivating oxidation layer on top of palladium nanoparticles with a palladium 0 core.

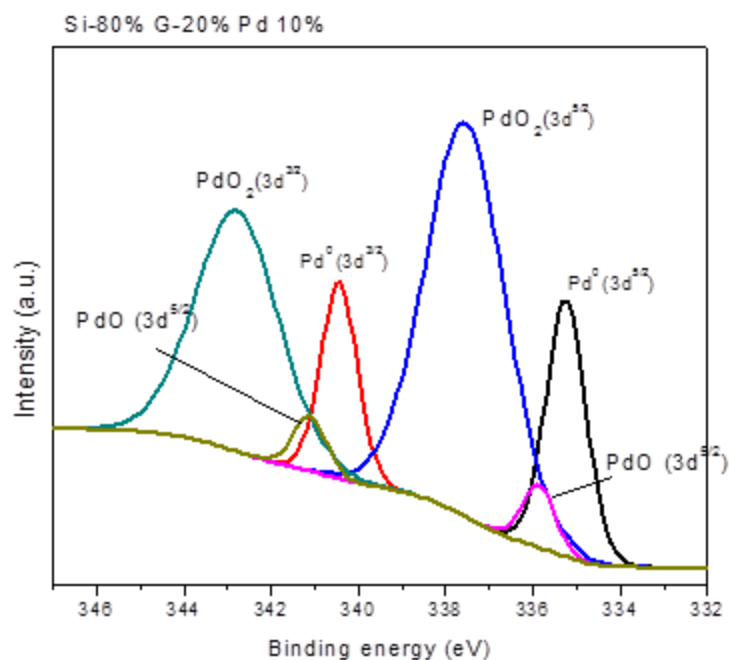


Figure 17. XPS spectrum of Pd/SiO_x-RGO sample with 10% palladium by weight. The XPS image was obtained by Julian Bobb.

Figure 17 depicts three oxidation states of palladium nanoparticles to be 0, +2 and +4. Binding energies of palladium 0 are 341.1 eV for Pd 3d^{3/2} and 335 eV for Pd 3d^{5/2}, for palladium +2 they are 341 eV for Pd 3d^{5/2} and 335.7 eV for Pd 3d^{3/2}, finally for palladium +4 the binding energies are 342.7 eV for Pd 3d^{3/2} and 337 eV for Pd 3d^{5/2}. These oxidation states might be the result of surface oxidation occurring on the particles right after synthesis process in the oven. Based on the intensity of the peaks, Pd (+4) species is present the most, followed by Pd (0) and Pd (+2). It is clear that with higher concentration of silicon in the support, total oxidation of palladium particles is lower compared to figures 15 & 16. Majority of palladium was in the form of +4 oxidation state in Pd-RGO sample in figure 15 and oxidation of palladium particles would decrease with introduction of silicon into the support in figure 16 and would further decrease with higher weight% of silicon in the support in figure 17.

4.2.4 Transmission Electron Microscopy

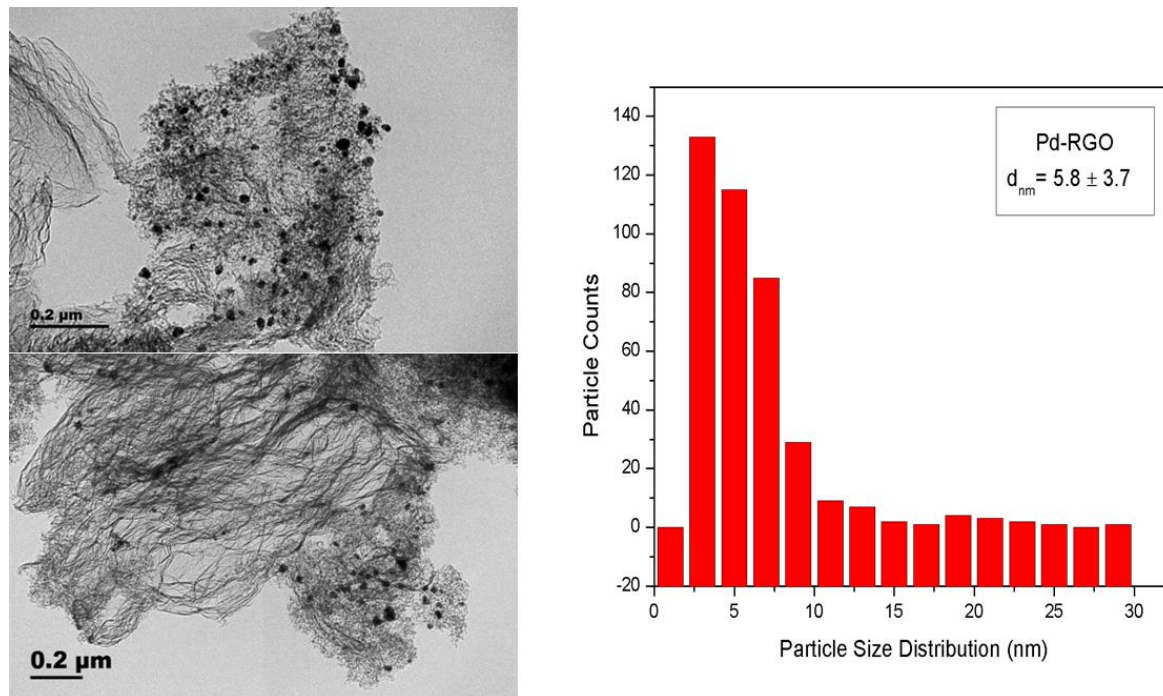


Figure 18. TEM images of Graphene with 10% palladium by weight deposited on the sheets. The TEM images were obtained by Dr. Khaled Abozeid.

Figure 18 depicts electron microscopy images of RGO catalyst support with palladium nanoparticles dispersed on the sheets. The mean size of the particles was 5.8 ± 3.7 nm and showed good dispersion across the sample.

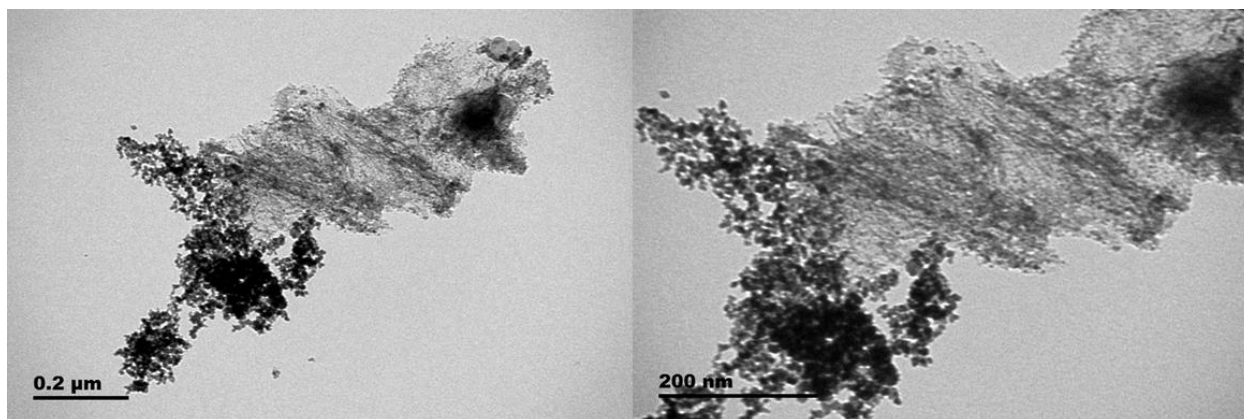


Figure 19. TEM images of Pd/SiO_x-RGO and 10% palladium by weight. The TEM images were obtained by Dr. Khaled Abozeid.

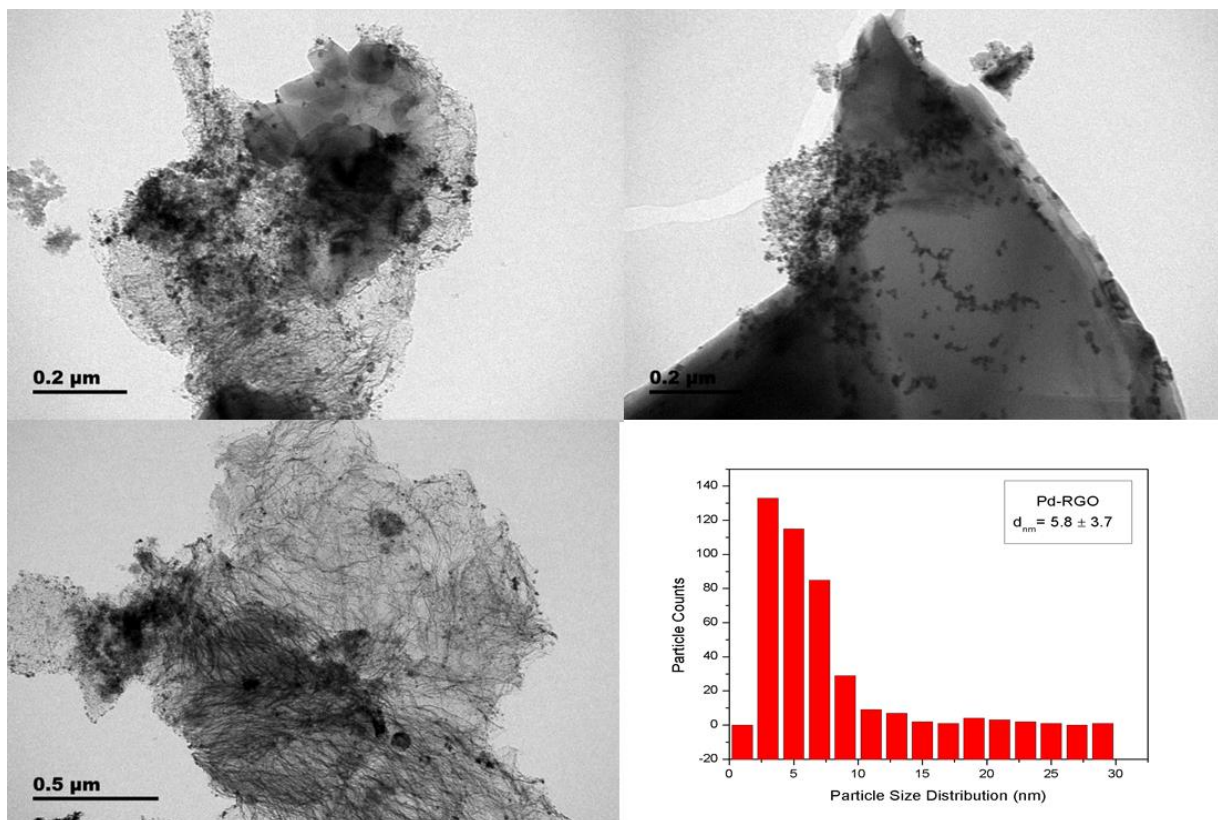


Figure 20. TEM images of silicon-graphene support with embedded palladium nanoparticles 10% by weight. The TEM images were obtained by Dr. Khaled Abozeid.

Figures 18-20 depict the Transmission Electron Microscopy images of palladium on graphene sheets. The mean size of nanoparticles was 7.4 ± 4.0 nm and the particles were polydisperse.

4.2.5 Raman Spectroscopy

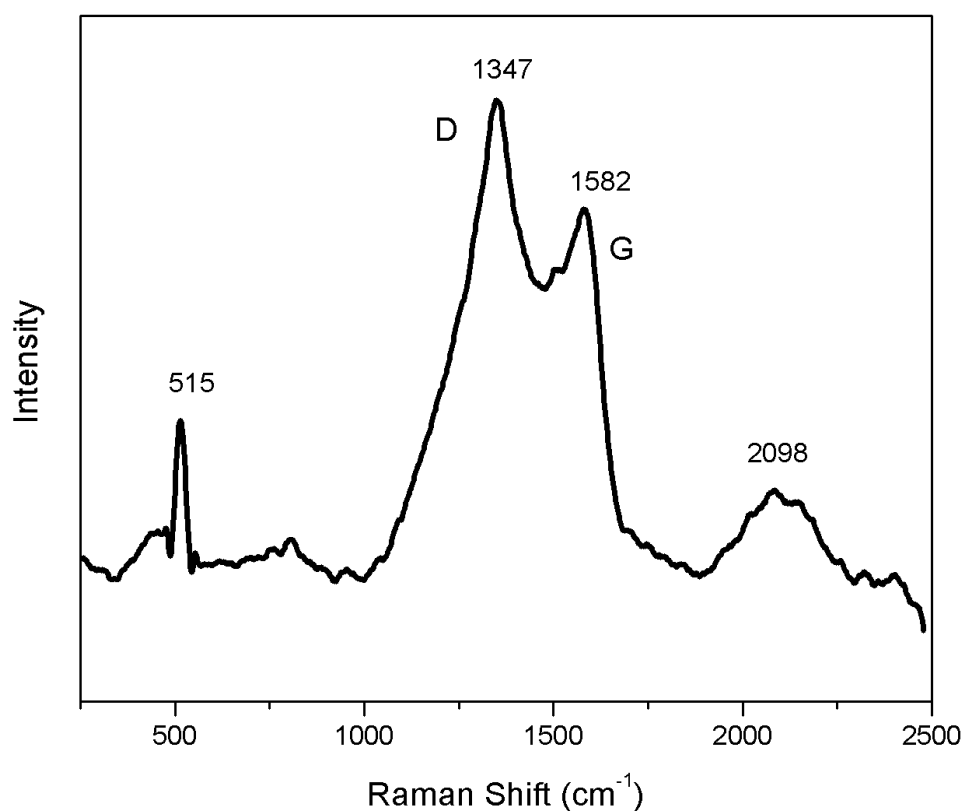


Figure 21. Raman scattering of SiO_x-RGO support used for carbon cross-coupling reactions.

Figure 21 depicts Raman scattering of SiO_x-RGO excited with 532 nm laser with a few prominent peaks. Peak at 515 cm⁻¹ corresponds to Raman allowed Transverse Optical phonon. There is a slight peak broadening present attributed to small size of silicon particles and based on the peak shift of 515 cm⁻¹ the average size of silicon nanoparticles is about 14 nm^{88, 97, 99}.

Generally, with smaller silicon nanoparticles the peak broadens at its base and shifts to lower wavenumbers.

Strong peaks at 1347 and 1582 cm^{-1} are observed corresponding to characteristic D and G band respectively. The D-band is attributed to structural disorder or defect sites of graphitic structures and represents “breathing mode” of sp^2 carbon atoms^{102, 103}. The G-band is attributed to stretching and vibrating modes of sp^2 atoms. Ratio of D/G gives a measure of amount of defects present and quality of the carbon materials. Generally the ratio approaches zero for highly ordered graphite and for a single layer graphene sheet¹⁰³. With higher D/G ratio, more defect sites are present which are favorable for catalysis applications due to metal nanoparticle immobilization. This immobilization is favorable, since nanoparticles will not be able to experience further growth and thus inhibiting growth of large particles and preventing their aggregation.

Broad peak around 2098 cm^{-1} corresponds to polyyne stretch representing carbyne which is a carbon chain structure with alternating triple and single bonds¹⁰⁴. Peak arises from the R mode which is out of phase stretching of C-C bond and is sometimes called the ECC mode. Generally, the polyyne band lies anywhere from 1800 to 2300 cm^{-1} and it relates to various C-C stretching vibrations.

Afshani⁸⁷ and co-workers have synthesized silicon nanoparticles and mixed them in solution with RGO nanosheets under pulsed laser irradiation at 532 nm. The Raman spectra displayed D band at 1367 cm^{-1} corresponding to defects of the RGO nanosheets and a G band at 1591 cm^{-1} corresponding to vibrations of sp^2 hybridized carbons within the RGO nanosheets. Because the synthetic procedure involved physical mixture of prepared silicon nanoparticles with

RGO nanosheets it was quite different from current work discussed where bulk silicon and bulk graphite oxide powder was mixed and irradiated in a cloud chamber under specific pressure and temperature conditions.

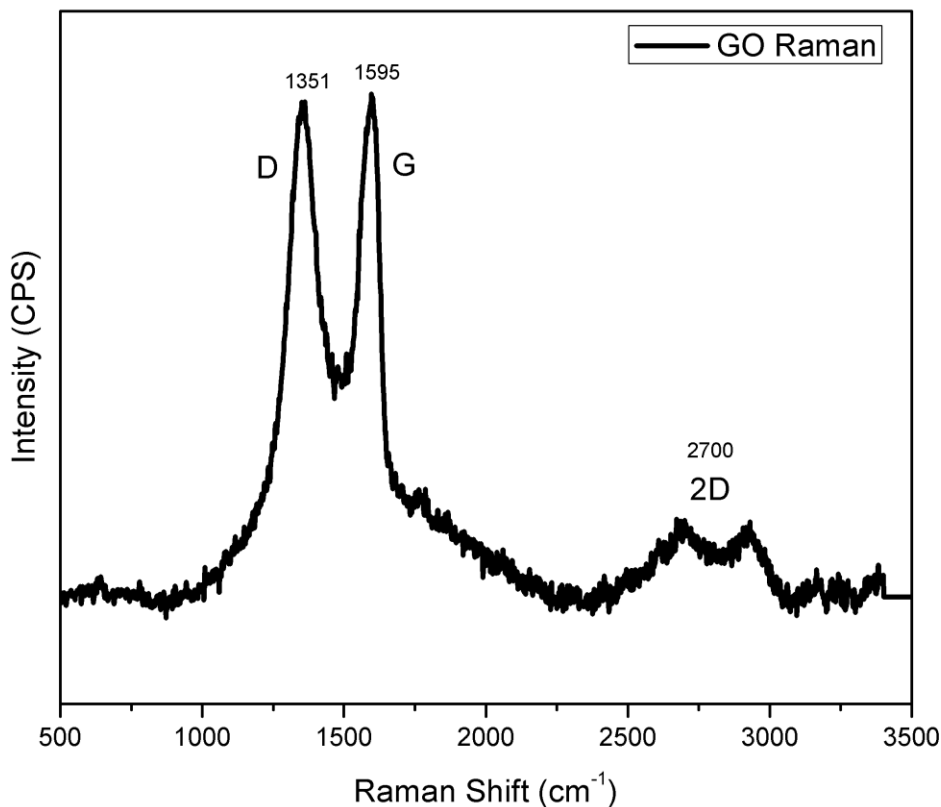


Figure 22. Raman scattering of Graphene Oxide.

Figure 22 depicts Raman spectroscopy of graphene oxide. As in figure 21, strong bands at 1351 cm^{-1} and 1595 cm^{-1} are observed which correspond to D and G bands respectively. A broad band around 2700 cm^{-1} corresponds to second order of D peak or 2D band of graphene¹⁰³. A single layer of graphene sheet would produce a sharp peak at 2700 cm^{-1} however broadening together with split into two components and drop in intensity occurs due to multiple sheets stacked upon

each other¹⁰⁵. Based on this 2D peak, it can be said that graphene oxide has more than 10 layers of graphene sheets¹⁰³.

4.2 Carbon Cross-Coupling Reactions Results*

Illustrated in table 1 are a series of reactions ran using Pd/SiO_x-RGO as a catalyst for Suzuki-Miyaura cross-coupling reaction. Conversion into biphenyl vs concentration of palladium catalyst in the system was studied by diluting the catalyst in the solvent and testing the catalysis performance in the microwave reactor. Table 1 illustrates the reactions carried out at different temperatures and different mol% of palladium catalyst. The best reaction carried out was with the use of 0.05 mol% of palladium at 80 °C and after 10 minutes 95% conversion of reactants into biphenyl was achieved. It is interesting to note that even with 10x fold more diluted catalyst, at the same temperature after 10 minutes 65% of reactant conversion into biphenyl was observed. Using 0.3 mol% of palladium catalyst supported on SiO_x-RGO a complete conversion into biphenyl was observed at room temperature after 25 minutes.

Calculation of palladium weight percent was performed using the following equation

$$\text{Pd wt\%} = \frac{\text{Pd mass}}{\text{SiO}_x\text{-RGO mass}} \times 100\% \quad (1)$$

where mass of palladium in milligrams is in the numerator divided by mass of SiO_x-RGO support in the denominator and multiplied by 100%. Different palladium weight percentage was tested throughout the catalysis – 5, 10 and 15% with 10% producing the best results for carbon cross-coupling reactions. The higher palladium loading of the sample was not efficient due to

possible aggregation of nanoparticles on the surface of the support. The 5 wt% loadings were not sufficient enough, possibly due to loss of palladium during the synthetic procedure and thus a significantly lower amount of palladium present on the surface of the support available for the cross-coupling reactions. The ICP-AES has revealed that the average weight% of palladium on the sample was close to 5.2% instead of theoretical 10 wt%. This significant loss of palladium can be attributed to poor reduction procedure and lack of proper mixing of the solution inside the conventional microwave oven. Additionally, despite that conventional microwave ovens operate in power range from 600 to 1000 Watt, the density of microwaves per unit volume inside the conventional oven is low. In future, reactor microwave would be a better option for reduction of palladium precursors due to higher density of microwaves per unit volume and the possibility of vigorously mixing the solution with the stirring bar.

Conversion of biaryl product was calculated based on the peak areas of products and reactants

$$\text{Conversion\%} = \frac{\text{Peak Area of Biaryl}}{\text{Peak Area of Reactants} + \text{Peak Area of Biaryl}} \times 100\% \quad (2)$$

where peak area extracted from GC-MS was in the numerator and peak areas of reactants and biaryl were in the denominator.

Table 1. Concentration studies in Suzuki-Miyaura reaction using 10% Pd-SiO_x/RGO (10-45-45%). The conversion measurements were provided by Dr. Ali Siamaki.

Concentration	Temp (°C)	Time (min)	Conversion%	TOF (h ⁻¹)
0.3 mol%	RT	25	100	800
0.1 mol%	RT	60	90	450
0.1 mol%	80	10	100	5988
0.05 mol%	80	10	95	11,377
0.005 mol%	80	10	65	77,844

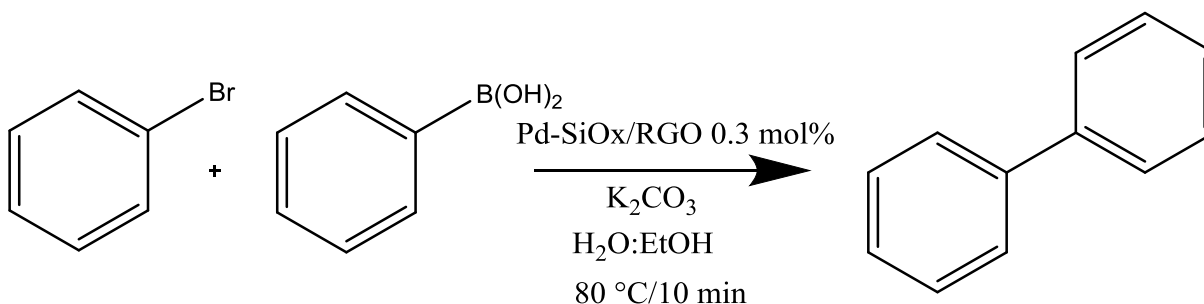


Figure 23. Suzuki-Miyaura cross-coupling reaction between bromobenzene and phenylboronic acid to produce biphenyl.

Reusability of catalyst is an important aspect in heterogeneous catalysis and is of vital importance in industry for saving costs to synthesize new catalysts and remove contaminants from the fine chemicals. As such, the Pd/SiO_x-RGO catalysts were tested for reusability and as can be seen from table 2, the catalyst can be recycled up to 3 times without significant drop in catalytic activity. After the 4th run, agglomeration of palladium particles occurs on the surface of the catalyst support, which reduced the amount of active sites on palladium particles, thus reducing the catalytic power to convert reactants into biphenyl. To avoid the aggregation of the particles, a better reducing method can be employed. For example, reduction of palladium nitrate with hydrazine hydrate can be performed in microwave reactor while the solution is being stirred vigorously to distribute the particles evenly across the catalyst support. Our synthetic procedure

included a conventional microwave oven, without the ability to stir the solution and thus homogeneously disperse the particles across the sample.

Table 2. Reusability test of Pd/SiO_x-RGO catalyst for Suzuki-Miyaura cross-coupling reaction performed at 80 °C for 10 minutes under microwave irradiation. This table was provided by Dr. Ali Siamaki.

Run	Conversion (%) ^a
1	100
2	100
3	100
4	65
5	25

Illustrated in table 3 are the various Pd/SiO_x-RGO catalysts with different loadings used for carbon cross-coupling reactions at room temperature. The highest conversion can be seen with Pd/SiO_x samples, entries 1 and 4, with 0.3 mol% and 0.05 mol% of catalyst loading in the system. Complete conversion into biphenyl can also be seen with the Pd-SiO_x/RGO catalyst, entry 5, after 40 minutes of reaction. The SiO_x-Pd catalyst has the best catalytic power and that can be attributed to higher amount of Pd (0) present on the surface of the SiO_x-RGO support as shown by the XPS spectroscopy, where the ratio of Pd (0) to other species of palladium was the highest. It could be possible that with higher concentration of silicon in the sample, palladium nanoparticles have a lower affinity towards oxidation, thus silicon could be hindering the growth of oxide layer on palladium nanoparticles. Despite of the unique mechanical and chemical properties of graphene, it still challenging to produce graphene sheets in mass quantities, thus using it for catalysis on industrial scale would be quite difficult. In comparison, silicon is the second most abundant element in the Earth's crust by weight, and silicon powder is

commercially available, thus making it a much more attractive option as a support for the Suzuki-Miyaura cross-coupling reaction.

Table 3. Comparison of catalytic activity among different SiO_x-RGO catalysts. Measurements of conversion in this table were provided by Dr. Ali Siamaki and Stanley Gilliland^a.

Entry	Catalysts	Loading	Temperature	Time (min)	Conversion%	TOF(h ⁻¹)
1	Pd/SiO _x (10-90%)	0.3 mol%	RT	15	100	1333
2	Pd-SiO _x /RGO (10-87-3%)	0.3 mol%	RT	22	95	901
3	Pd-SiO _x /RGO (9-73-18%)	0.3 mol%	RT	20	97	1010
4 ^a	Pd-RGO (10-90%)	0.3 mol%	RT	30	100	333
5	Pd/SiO _x (10-90%)	0.05 mol%	RT	25	100	4762
6	Pd-SiO _x /RGO (10-87-3%)	0.05 mol%	RT	40	100	2985
7	Pd-SiO _x /RGO (9-73-18%)	0.05 mol%	RT	45	98	2667
8 ^a	Pd-RGO (10-90%)	0.05 mol%	RT	30	100	2000

Illustrated in table 4 are different catalysts from various research groups used in Suzuki-Miyaura cross-coupling reactions and comparison of their catalytic activity.

Yang¹⁰⁶ and co-workers have synthesized Pd/PdO-CNT catalysts through gas-liquid interfacial plasma (GLIP) and have reported a yield of 73% for Suzuki cross-coupling reaction. The group has tested the catalyst for reusability and has managed to recycle the catalyst up to 9 times without significant drop in yield. Ignaszak's group¹⁰⁷ has synthesized multi-walled carbon nanotubes where palladium nanoparticles were electrodeposited on its surface. Resulting catalyst

produced a 84% conversion after 2.5 hours of reflux reaction at ambient conditions. However, upon testing the catalyst recyclability, the yield decreased significantly after the 2nd and 3rd run to 62 and 31% yield respectively. Fareghi-Alamdari¹⁰⁸ and co-workers have tested their phosphine modified graphene support (PFG) anchored with palladium nanoparticles for Suzuki cross coupling reaction. Their group has managed to achieve 93% conversion after 12 hour reaction in mild base conditions at 80 °C temperature. The catalyst has been successfully reused up to 5 times without significant drop in activity. Gomez-Martinez¹⁰⁹ has reported 99% conversion after 12 hour microwave reaction in mild base conditions using 0.1 mol% palladium nanoparticles supported on graphene sheets. The Pd-G catalyst showed excellent recyclability where conversion remained virtually unchanged even after 8 reaction runs. Brinkley¹¹⁰ and co-workers have reached 100% conversion for biaryl by using palladium nanoparticles supported on graphene. The maximum conversion was reached within 10 minutes of microwave irradiation at 80 °C. Brinkley has managed to successfully recycle the catalyst up to 4 times without significant loss in catalytic activity. Palladium nanoparticles supported on nafion-graphene have shown excellent catalytic activity for Suzuki cross coupling reaction by yielding a 95% conversion after 2 hour reaction at 25 °C using methanol as solvent as reported by Kishor¹¹¹ and co-workers. They have tested their catalyst for reusability and reported no significant drop in catalytic activity up to 5 reaction runs. Durap¹¹² has synthesized chemically derived graphene and incorporated palladium nanoparticles for testing it for Suzuki cross coupling reactions. His group achieved 98 % conversion after 5 hour reaction at 110 °C in mild base conditions. Catalyst reusability test has been performed up to 15 times without significant loss in catalytic activity. Palladium nanoparticles supported on reduced graphene sheets have been synthesized by Hussain¹¹³ and co-workers and tested for Suzuki-Miyaura reaction. They have achieved 94%

conversion after 2 hour reaction under room temperature and in mild base conditions in ethanol solvent. Recycling test has showed that the Pd-rGO retained its catalytic power up to 4 runs for Suzuki cross-coupling reaction. Visic¹¹⁴ and co-workers have synthesized WS₂ nanotubes incorporated with palladium nanoparticles and tested it for Suzuki cross-coupling reaction. They have achieved 86% conversion after 3 hour reaction in methanol-water solvent at 55 °C under mild base conditions. A palladium – carbon nanotube hybrid catalyst was synthesized by Jawale¹¹⁵ and co-workers and has shown excellent activity towards carbon cross coupling reaction. The catalyst was tested for Suzuki cross-coupling reaction and Jawale's group achieved 98% conversion after 4 hour reaction at room temperature in mild base conditions. However, despite catalyst's good performance the reusability of the catalyst has not been tested. Cornelio¹¹⁶ reported synthesizing nanoreactors consisting from hollow graphitized nanofibers (GNF) enshrouded with palladium nanoparticles. He successfully tested the catalyst for Suzuki cross-coupling reaction and has achieved 98% conversion after 24 hour reaction at 70 °C in methanol solvent. However, when the catalyst was studied for reusability, there was a significant drop in catalytic activity after the first run and it remained very similar throughout the next 4 reaction runs. Zahraei¹¹⁷ and co-workers have synthesized Fe@Pd nanowires through arc discharge of iron electrodes and drop-drying palladium chloride onto the iron nanowires. The catalyst was tested for Suzuki cross-coupling reaction and gave a high conversion of 92% after 5 hour reaction in water solvent at room temperature with mild base conditions. Because the catalyst consists of iron nanowires enshrouded with palladium nanoparticles, it can be easily separated from the reaction mixture by using an ordinary magnet. An interesting catalyst composite material consisting of ordered mesoporous silica containing Zn MOFs enshrouded with palladium nanoparticles was synthesized by Yang's group¹¹⁸ and tested for cross-coupling

reactions. The catalyst tested produced a 94.3% conversion for biaryl product after 2 hour reaction at 80 °C under mild base conditions in ethanol solvent. Despite catalyst's excellent activity, it was not tested for reusability. Palladium nanocatalysts incorporated into partially reduced graphene oxide (Pd/PRGO) nanosheets have been synthesized through pulsed irradiation of aqueous solution of graphene oxide and palladium precursors by Moussa¹¹⁹ et al. The resulting catalysts were tested for Suzuki-Miyaura and have demonstrated remarkable activity. The palladium catalysts with mean particle size of 7.8 nm distributed on PRGO has shown a 100% conversion of bromobenzene into biaryl after 45 minute reaction in a microwave reactor under mild base conditions. Similar catalysts only with larger mean palladium particle size have been tested and have shown slightly lower activity of 95% and 85% for 10.8 and 14.8 nm sized palladium particles respectively. Such high activities for Suzuki cross-coupling reactions were attributed to large presence of Pd⁰ nanoparticles on the surfaces of PRGO sheets as well as multiple defects on PRGO sheets arising from laser irradiation. These defect sites would impair the movement of nanoparticles and thus reduce the probability of their coalescence leading to improved stability and reusability properties of the catalyst. In comparison to this work discussed, the reduction of palladium precursors was performed in solution of graphene oxide with ethanol under 532 nm pulsed laser irradiation. Because GO is a semiconductor with a bandgap ranging from 2.5 – 4.0 eV depending on the degree of oxidation, it would absorb two 532 nm photons and create an electron-hole pair. These generated electrons would then reduce the palladium ions from +2 to 0 state. Photogenerated electrons would further reduce GO sheets to produce partially reduced graphene oxide sheets. In this work, however, palladium nanoparticles were reduced using a very strong reducing agent – hydrazine hydrate under microwave irradiation which would reduce Pd⁺² ions into Pd⁰. Because of this strong chemical

reduction, the catalytic conversion of Pd-SiO_x is higher as evident by using only 0.05 mol% of catalyst in Suzuki-Miyaura cross coupling reaction. Siamaki¹²⁰ and co-workers have synthesized Pd/G catalyst by supporting palladium nanoparticles on graphene sheets via reduction of palladium nitrate on graphene oxide using hydrazine hydrate and microwave irradiation. The reported catalyst was tested for Suzuki-Miyaura reaction and 0.3 mol% of Pd/G catalyst resulted in complete conversion of bromobenzene into biaryl after 25 minutes of reaction under mild base conditions in microwave reactor. Elazab et al has reported 100% conversion for Suzuki cross coupling reaction using well dispersed mixture of palladium and iron oxide nanoparticles supported on GO sheets with average Pd⁰ to Pd²⁺ ratio of 8.1. The highest conversion was reached under mild base conditions after 45 minutes at room temperature using microwave reactor and due to the magnetic properties of iron oxide nanoparticles, the catalyst was easily recycled up to 8 times without significant loss in activity. Catalyst synthesized by Elazab displayed 6-8 nm sized palladium nanoparticles of which majority were Pd⁰ together with 12-16 nm sized iron oxide particles supported on highly reduced graphene oxide.

Table 4. Comparison of catalytic activity for carbon cross-coupling reactions with different catalyst systems from recently published literature.

Entry	Catalyst	Loading(Pd)	Temp	Time	Conversion %	Ref.
1	Pd/PdO-CNT	0.1 mol%	90 °C	1 hour	73	Yang ¹⁰⁶
2	Pd@MWCNT	n/a	Room	2.5 hours	84	Radtke ¹⁰⁷
3	PFG-Pd	1.2 mol%	80 °C	12 hours	93	Fareghi-Alamdari ¹⁰⁸
4	Pd-G	0.1 mol%	80 °C	2 hours	99	Gomez-Martinez ¹⁰⁹
5	Pd-G	2 mol%	80 °C	10 min	100	Brinkley ¹¹⁰
6	Pd/Nf-G	0.2 mol%	25 °C	2 hours	95	Kishor ¹¹¹
7	Pd-CDG	0.005 mol%	110 °C	5 hours	98	Durap ¹¹²
8	Pd-rGO	n/a	Room	2 hours	94	Hussain ¹¹³
9	Pd-WS ₂	n/a	55 °C	3 hours	86	Visic ¹¹⁴
10	Pd-CNT	1.2 mol%	Room	4 hours	98	Jawale ¹¹⁵
11	Pd@GNF	2.0 mol%	70 °C	24 hours	98	Cornelio ¹¹⁶
12	Fe@Pd	3.0 mol%	Room	5 hours	92	Zahraei ¹¹⁷
13	OMS@Pd-ZnMOF-10%	1.2 mol%	80 °C	2 hours	94.3	Yang ¹¹⁸
14	Pd/PRGO	0.5 mol%	Room	45 min	100	Moussa ¹¹⁹
15	Pd/G	0.3 mol%	Room	25 min	100	Siamaki ¹²⁰
16	Pd-Fe ₃ O ₄ /GO	0.3 mol%	Room	45 min	100	Elazab ¹²¹
17	Pd-SiO _x	0.05 mol%	Room	25 min	100	This work

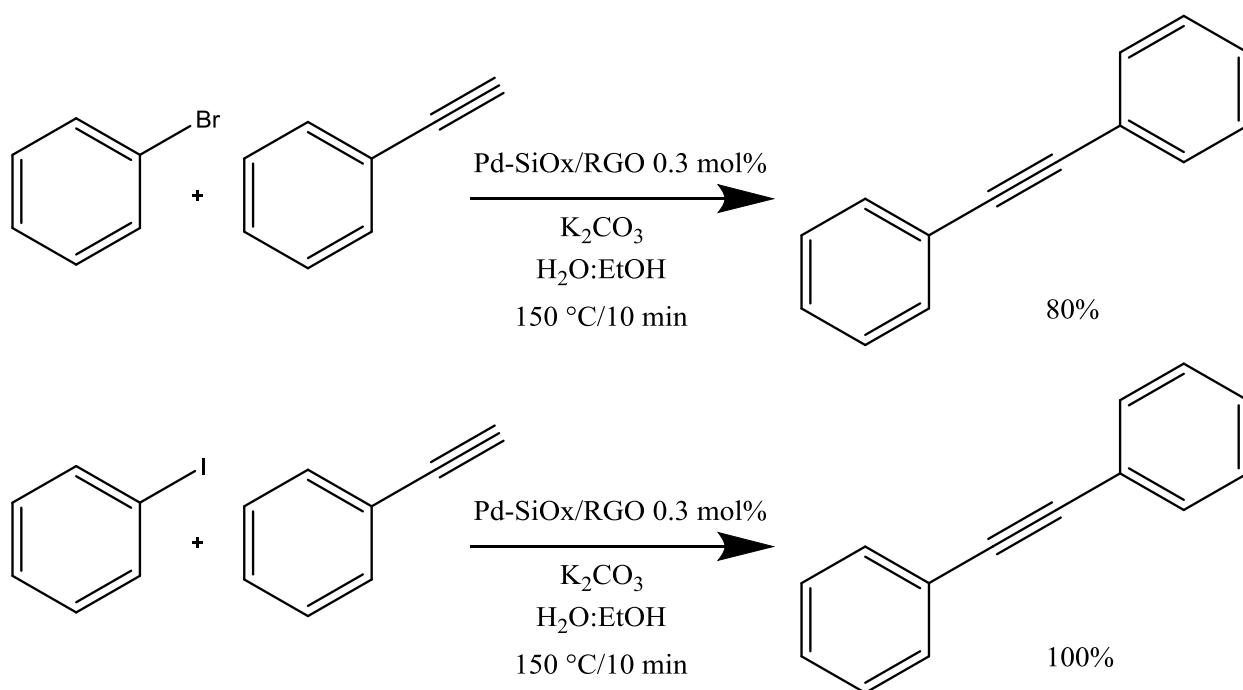


Figure 24. Sonogashira reactions using 10% palladium by weight on SiO_x/RGO support and its corresponding conversion into products. The conversion of reactants into products was provided by Dr. Ali Siamaki.

Figure 24 depicts Sonogashira reactions of bromobenzene and iodobenzene with phenylacetylene using Pd/SiO_x-RGO catalysts at 0.3 mol% loading in the system. Using iodobenzene as a starting reactant gave a higher conversion of reactants into diphenylacetylene which is attributed to a weaker bond between iodine and aromatic carbon compared to bromine-carbon bond. Furthermore, iodine is known to be a better leaving group compared to bromine. Although, iodobenzene is a better starting reagent for Suzuki-Miyaura reaction, bromobenzene is cheaper and thus it is more appropriate to use bromobenzene as a starting reagent for catalytic tests.

4.3 Characterization of Pd@UiO-67 catalyst

The zirconium-based metal organic frameworks were first successfully synthesized in University of Oslo in 2008 by Jasmina Cavka and co-workers¹²². The new zirconium-based MOF was named after the university in which it was first synthesized - Universitet i Oslo (UiO). The UiO MOFs structure consist of Zr₆O₄(OH)₄(CO₂)₁₂ inorganic brick which is 12 coordinated to 1,4-benzene-dicarboxylate linkers (BDC), 4,4' biphenyl-dicarboxylate (BPDC) and terphenyl dicarboxylate (TPDC) in the cases of UiO-66, UiO-67 and UiO-68 respectively. Figure 24 depicts all three MOFs with different linkers.

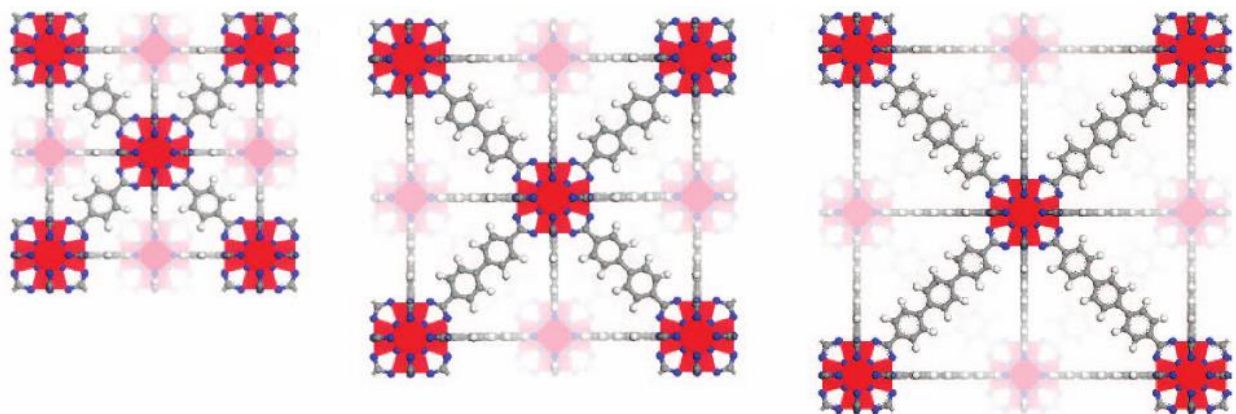


Figure 25. (Left) UiO-66 with BDC linkers, (center) UiO-67 with BPDC linkers and (right) UiO-68 MOF with TPDC linkers, where zirconium atoms are red, oxygen are blue, carbon are gray and hydrogen are white¹²².

Because the MOF is 12 coordinated it follows a cubic closed packed structure (CCP) otherwise known as face centered cubic (FCC). It was demonstrated that Zr-MOFs can be made with increasing length of the linkers without compromising their stability. Thermal decomposition of Zr-MOFs does not occur until a temperature of 540 °C is reached, where benzene can be seen as a separate fragment in the gas phase. Thus the weakest link in the UiO MOFs is the bond between the terminal carboxyl groups and the benzene rings and not between benzene-dicarboxylate linker and inorganic node. Further research has supported that claim and performed DFT calculations to show that Zr-MOFs are stable to cleavage between the inorganic node and the linker¹²³.

Surface areas have been calculated and measured for the UiO MOFs and it has been shown that with increasing linker length the pore volume of the structures and its surface area increases with a longer linker. The Langmuir surface area of UiO-66 was measured to be 1187 m² g⁻¹ while the BET surface areas of UiO-67 and UiO-68 were measured to be 3000 m² g⁻¹ and 4170 m² g⁻¹ respectively. The pore availability of the UiO MOFs is restricted by triangular

windows formed by the linkers where UiO-66, 67 and 68 have window openings of 6, 8 and 10 Å respectively. Even the smallest window opening of UiO-66 can allow fully methylated benzene ring inside the porous structure, thus molecules of similar sizes or smaller would be able to occupy the pores for storage or catalysis purposes. The UiO MOFs have been tested for their chemical resistance against different solvents by having the desolvated sample stir in acetone, benzene, ethanol, DMF and water at room temperature for 24 hours. After being stirred in these solvents, powder x-ray diffraction was taken where the peaks corresponding to the UiO MOF have been virtually unchanged. Mechanical stability of Zr-based MOFs was tested by applying external pressure of 10 000 kg/cm² and powder x-ray diffraction patterns have shown no change in the crystallinity of the material. Wu¹²⁴ reported the minimum shear modulus of the UiO-66 MOF to be 13.7 GPa, which is significantly higher compared to other highly porous MOFs, such as MOF-5 and HKUST-1. The UiO-66 MOF in its mechanical rigidity is close to zeolites. Such high mechanical stability is attributed to very high framework connectivity between the inorganic nodes with 12 linkers, which is very important for its practical applications such as gas storage or gas separation. Only 2 other MOFs are known for having such a high coordination number – UiO-66 isostructural MOF from Ferey¹²⁵ group where the ligand is *trans,trans* muconic acid and the aluminum-based CAU-1 MOF from Stock¹²⁶ group.

Such chemically stable and mechanically strong MOFs are scarce - out of reported 20 000 MOFs¹²⁷, only a few of them stand up to such claims including MOF-5, MIL-53 (Al), HKUST-1 and the UiO MOFs.

4.3.1 X-ray Diffraction

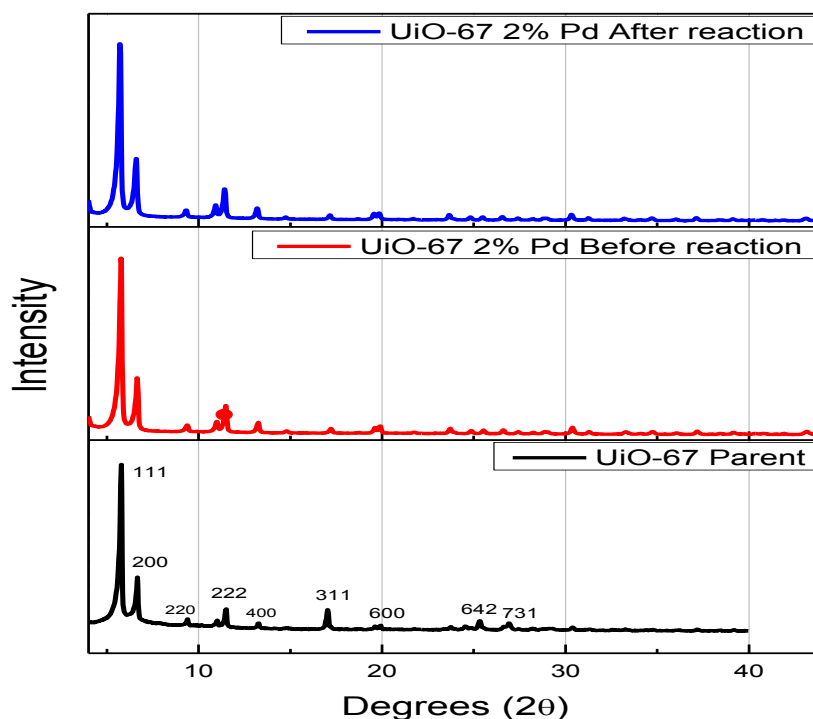


Figure 26. Powder X ray diffraction patterns of (black) UiO-67 (red) Pd/UiO-67 (blue) Pd/UiO-67 after benzyl alcohol oxidation reaction.

Illustrated in figure 26 are the powder x-ray diffraction patterns of UiO-67 parent material and UiO-67 enshrouded in palladium nanoparticles before and after the reaction. The diffraction pattern closely follows the literature published by Cavka¹²², Katz⁸¹ and others^{123, 128-130}. For UiO-67 MOF powder x-ray diffraction shows crystalline lines 111, 200, 220, 222, 400, 311, 600, 642, 731 at 6, 7, 9, 11, 13, 17, 20, 25, 27° respectively. The 111 peak at 40° corresponding to palladium was not present on the powder x-ray diffraction possibly for two reasons: the palladium content was too low to give any scattering or the palladium particles were inside the porous MOF structure. The peak shifts in the powder x-ray diffraction patterns are insignificant demonstrating the stability of the support throughout the reaction progress during oxidation of benzyl alcohol.

4.3.2 FTIR Spectroscopy

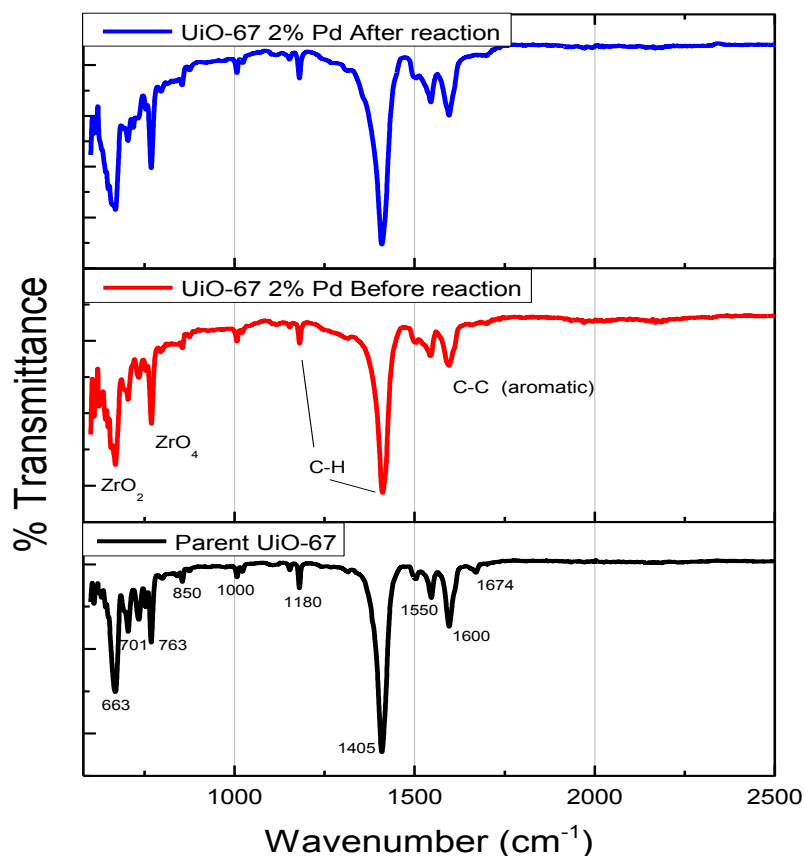


Figure 27. Fourier Transformation Infrared spectra of UiO-67 crystals displaying parent material (black) UiO-67 with palladium before the reaction (red) and UiO-67 with palladium after the reaction (blue).

Illustrated in figure 27 are the FTIR spectra of UiO-67 that experienced almost no change in peak shifts throughout the reaction. The FTIR spectra depicted in figure above correlate with the literature spectra published^{122, 129, 131, 132} The peak at 1674 cm⁻¹ corresponds to DMF that is present within the pores of freshly prepared UiO-67 and later disappears after palladium nanoparticle impregnation. The doublet at 1405 cm⁻¹ and 1600 cm⁻¹ corresponds to stretches of carboxylate group from the BPDC linker. Peaks at 663 cm⁻¹ and 701 cm⁻¹ correspond to longitudinal and transverse modes of inorganic ZrO₂ brick. Peak at 1180 cm⁻¹ corresponds to

single bonded carbon hydrogen originating from BPDC linkers. Peaks at 1500 cm^{-1} to 1550 cm^{-1} correspond to aromatic carbon-carbon bond originating from BPDC linker.

4.3.3 Nitrogen Adsorption Isotherms

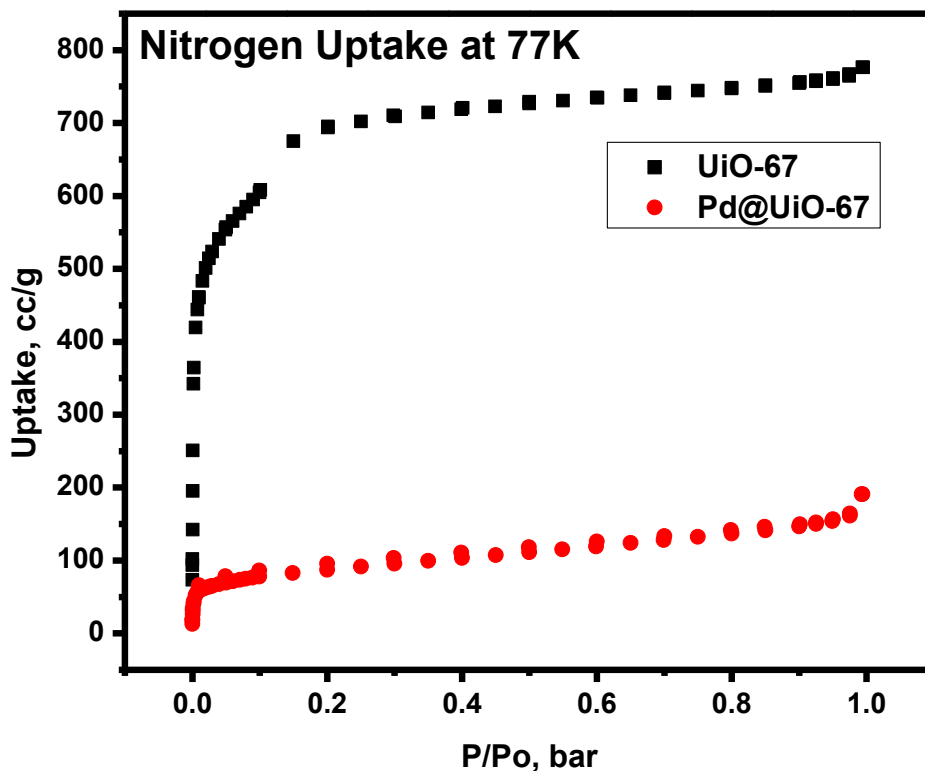


Figure 28. Nitrogen adsorption isotherms of (black) UiO-67 and (red) palladium loaded UiO-67 metal organic framework at 77 K. This data was obtained by Tsemre Tessema from Dr. El-Kaderi's group.

Depicted in figure 28 are the nitrogen adsorption isotherms at 77 K for freshly prepared UiO-67 and for the UiO-67 loaded with palladium nanoparticles after pulsed laser irradiation. The measured surface area of freshly prepared UiO-67 is $2591\text{ m}^2\text{ g}^{-1}$ slightly lower than its theoretical surface area of $3000\text{ m}^2\text{ g}^{-1}$ but it is in good agreement with values published in literature^{81, 122, 133} The reason why the measured surface area is slightly lower compared to the

theoretical value is attributed to the capillary forces driven collapse of pores during drying process, where solvents with relatively high surface tension such as water and DMF are present inside the pores of the UiO-67 framework. This problem of capillary forces driven pore collapse can easily be avoided by using solvent exchange technique where low surface tension liquids such as acetone can be used for washing the pores of the MOF. Ultimately, supercritical CO₂ liquid, possessing zero surface tension, can be used to efficiently clean the pores without damaging them in the washing process. The UiO-67 adsorption isotherm corresponds to type I physisorption isotherm defined by IUPAC¹³⁴, indicating MOF's microporous and mesoporous nature of its tetrahedral and octahedral holes of 18 and 23 Å respectively.

The measured surface area of palladium loaded UiO-67 is 317 m² g⁻¹ and follows type IV(a) physisorption isotherm according to the updated IUPAC classification of isotherms¹³⁵. Type IV(a) isotherm validates the presence of mesoporous material which UiO-67 is considered to be. The surface area is low for metal organic framework loaded with palladium nanoparticles compared to literature which has reported surface area values of around 2000 m² g⁻¹ with comparable palladium weight¹³⁶. Although it has been demonstrated by various research groups^{122, 123} that zirconia-based MOFs are known to be mechanically and thermally stable, and immune to various acids, bases and aggressive industrial solvents such as benzene, acetone, toluene and *N,N*-dimethylformamide (DMF), there is still a lot of controversy surrounding the superior structural stability of zirconia based MOFs. A possible explanation to the low measured surface area of Pd/UiO-67 could be the use of palladium nitrate precursor which caused a collapse in pore structure of UiO-67. Ebrahim¹³⁷ reported decrease in porosity of UiO-67 framework after exposing it to NO₂ gas in moist conditions. Nitrogen dioxide exposed to water inside the pores of UiO-67 leads to formation of nitrous/nitric acid further reacting with

zirconium oxide units in the inorganic node, leading to the formation of zirconium oxynitrate hydrate.^{137, 138} Thus, formation of zirconium oxynitrate hydrate destroys the $\text{Zr}_6\text{O}_4(\text{OH})_4$ core of the node and causes a collapse of UiO-67 structure, leading to a significantly lower measured surface area¹³⁷. Decrease of surface area in the UiO-67 is stronger when both nitrogen dioxide and water is present in the pores of the MOF as compared to dry exposure to nitrogen dioxide¹³⁷. During washing procedure of UiO-67 and because of its microporosity, its pores quickly absorb water from the air and retain it within its pores. To avoid potential structure collapse, supercritical CO_2 can be used to clean the metal organic framework and help retain its structure for a significantly longer time.

Although measured surface area has decreased significantly from $2591 \text{ m}^2 \text{ g}^{-1}$ to $317 \text{ m}^2 \text{ g}^{-1}$, there are still some UiO-67 MOF crystals present in the mixture as the PXRD and FTIR patterns show in figures 26 & 27 respectively.

4.3.4 Pore Size Distribution

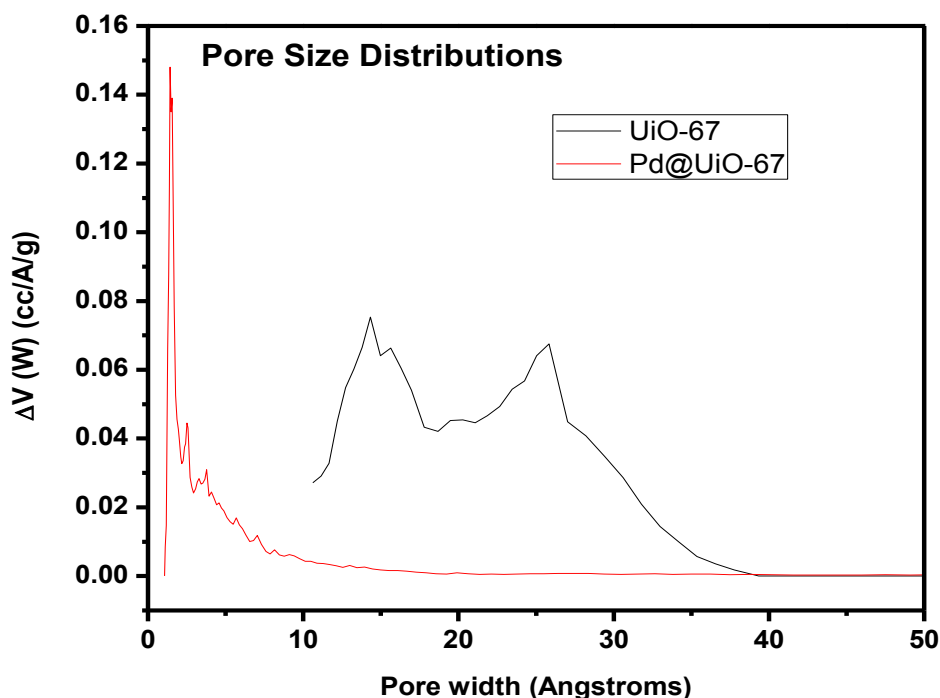


Figure 29. Pore size distribution of (black) UiO-67 and (red) Pd@UiO-67. This data was provided by Tsemre Tessema from Dr. El-Kaderi's group.

Figure 29 depicts the pore size distribution in the freshly prepared UiO-67 before loading with palladium nanoparticles and pore size distribution in the Pd/UiO-67 after loading with palladium nanoparticles. The majority of the pores in the UiO-67 are 15 and 26 Å which correspond to octahedral and tetrahedral pores respectively. These pore sizes agree well with the published literature values by Katz⁸¹ and Cavka¹²². The pore size distribution illustrates that UiO-67 MOF is a micro and mesoporous material, where micropores are less than 20 Å in diameter and mesopores are in the size range from 20 Å to 500 Å.

The pore size of the UiO-67 loaded with palladium nanoparticles is approximately 1-2.5 Å which is significantly smaller compared to pristine UiO-67 and published literature values⁸¹,

¹²². These are essentially bond lengths between atoms in the structure of the UiO-67, thus it is more likely that the structure has structurally failed or the pores are completely blocked by the palladium nanoparticles. Part of the MOF's structural collapse could have been caused by excessive size of palladium nanoparticles of about 20 nm, which corresponds to about 200 Å, making the nanoparticles 8 to 13 times larger than the pores in the UiO-67 MOF. Another possible explanation of the collapse of the UiO-67 structure could be palladium nitrate, where the precursor is slightly diluted in 10% nitric acid. As mentioned previously, the nitrates can be dissolved by water in the pores of UiO-67 and form nitrous/nitric acid that would react with Zr-O bond to form zirconium oxynitrate hydrate triggering the structural failure¹³⁷.

4.3.5 Transmission Electron Microscopy

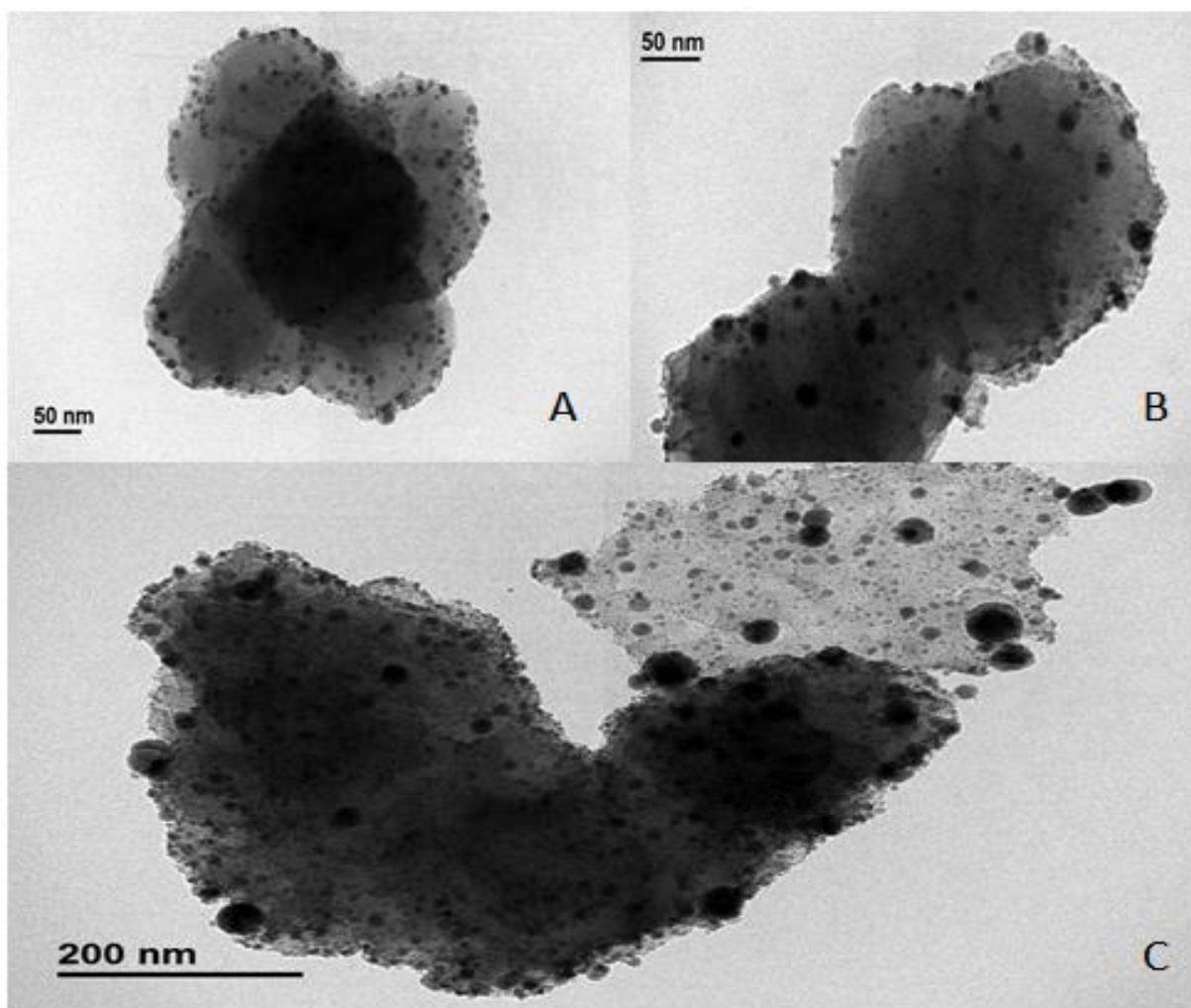


Figure 30. Transmission electron micrographs of UiO-67 crystals displaying (A) 1% palladium (B) 2% palladium and (C) 5% palladium by weight. These TEM images were obtained by Dr. Khaled Abozeid.

Figure 30 depicts electron microscopy images of Pd@UiO-67 catalysts. Generally, particle size increases with a higher loading of palladium on the UiO-67 MOF, which can be visually identified in figure 29A-C.

The weight percentage of palladium in the UiO-67 was calculated using a similar formula in eq 1 for weight loading of palladium on SiO_x-RGO

$$\text{Pd wt\%} = \frac{\text{Pd mass}}{\text{UiO-67 mass}} \times 100\% \quad (3)$$

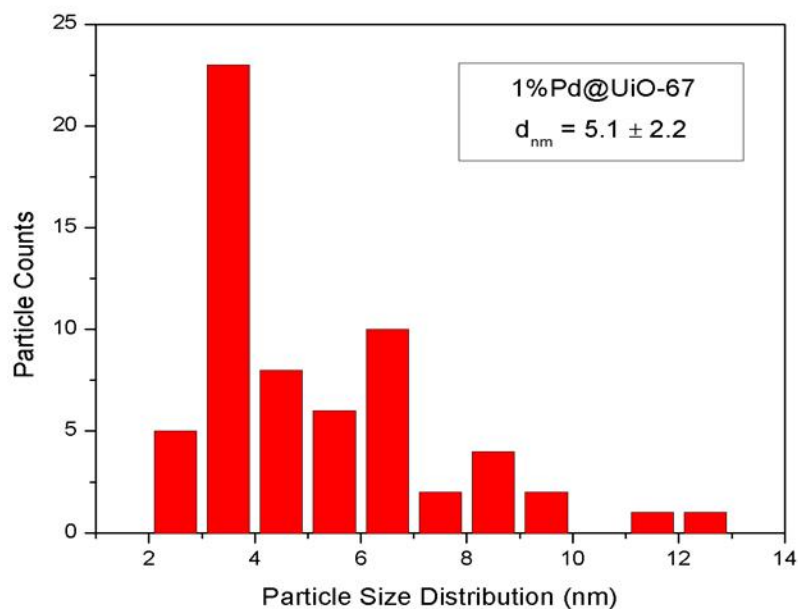
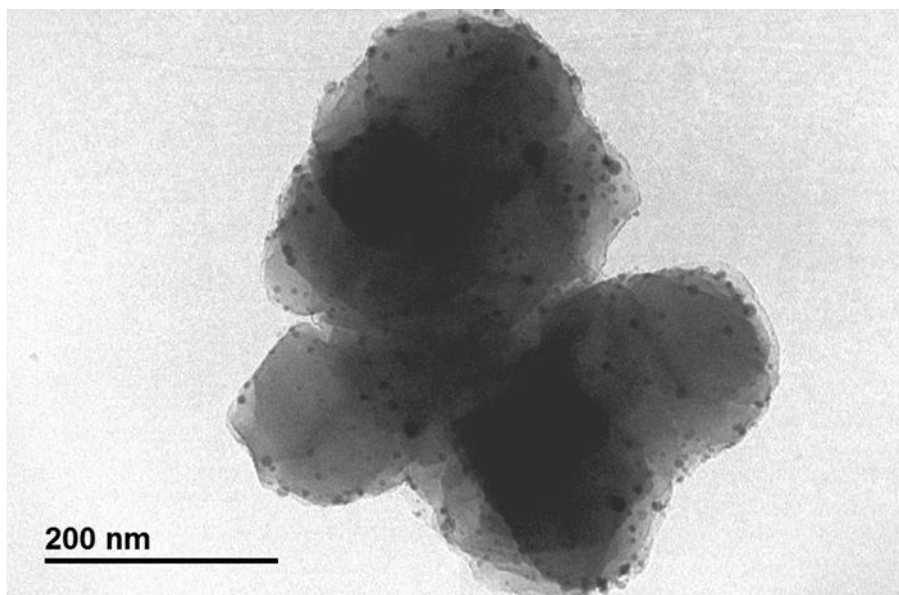


Figure 31. TEM image (A) of Pd@UiO-67 MOF crystal with 1% palladium by weight (B) size distribution of palladium nanoparticles on the UiO-67 MOF. The TEM image was obtained by Dr. Khaled Abozeid.

Figure 31A illustrates the image of a MOF crystal loaded with only 1% palladium by weight. As a result of such a low loading the mean size of particles is 5.1 ± 2.2 nm and they are

quite monodisperse. It is interesting to note that with lower palladium precursor smaller and more monodisperse particles are formed compared to higher palladium loadings. This is attributed to lower palladium to reducing solvent ratio and higher irradiation power per mole of palladium present in the solution, thus promoting growth of palladium nanoparticles that is limited by the size of the UiO-67 pores. Ultimately for catalysis purposes, small and highly monodisperse particles are highly attractive, considering they convert more reactants into products per unit time.

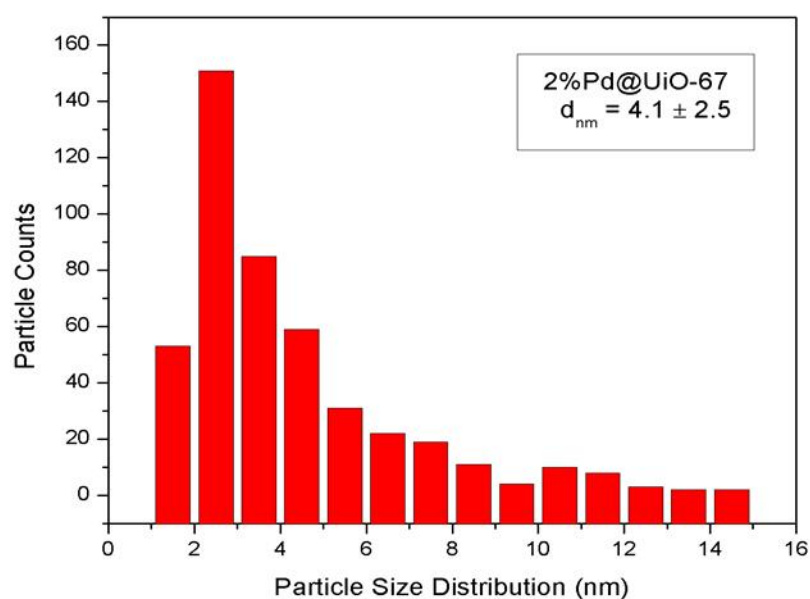
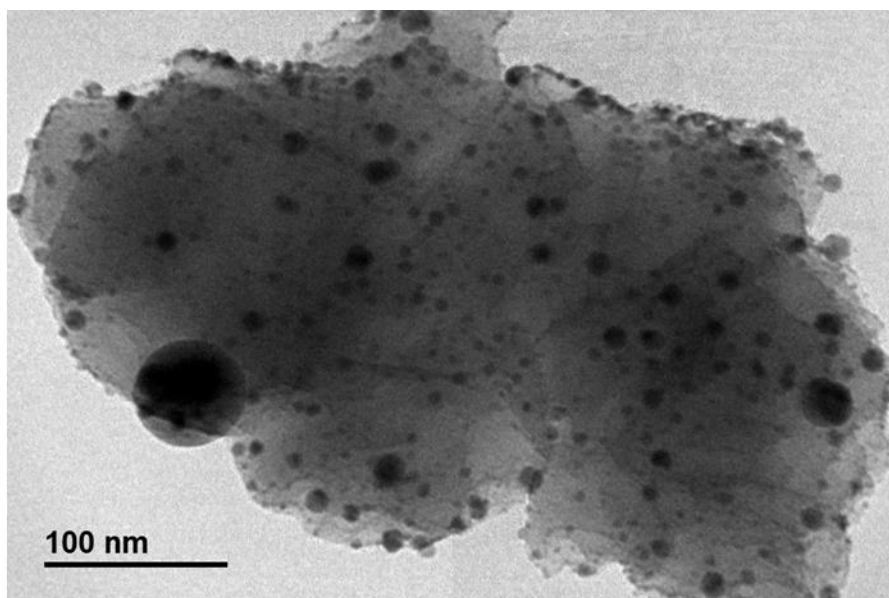


Figure 32. TEM image (A) of Pd@UiO-67 MOF crystals with 2% palladium by weight, (B) size distribution of palladium nanoparticles within UiO-67. The TEM image was obtained by Dr. Khaled Abozeid.

Figure 32A depicts the UiO-67 crystal with 2% palladium loading by weight. The mean size of the palladium particles is 4.1 ± 2.5 nm. Even though, the mean size of palladium nanoparticles present in the 2% palladium by weight sample is lower compared to 1% palladium

by weight sample, the particles are quite polydisperse suggesting large particles (up to 40 nm) can be present together with 4 nm particles. Very large particles were not accounted for in the calculations and therefore the real mean size of the particles is slightly higher than what is report in figure 32B.

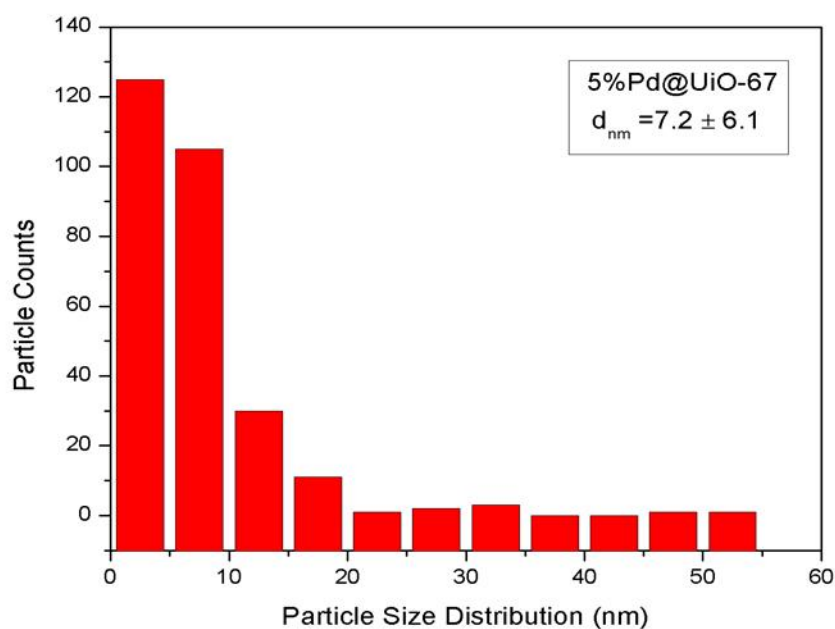
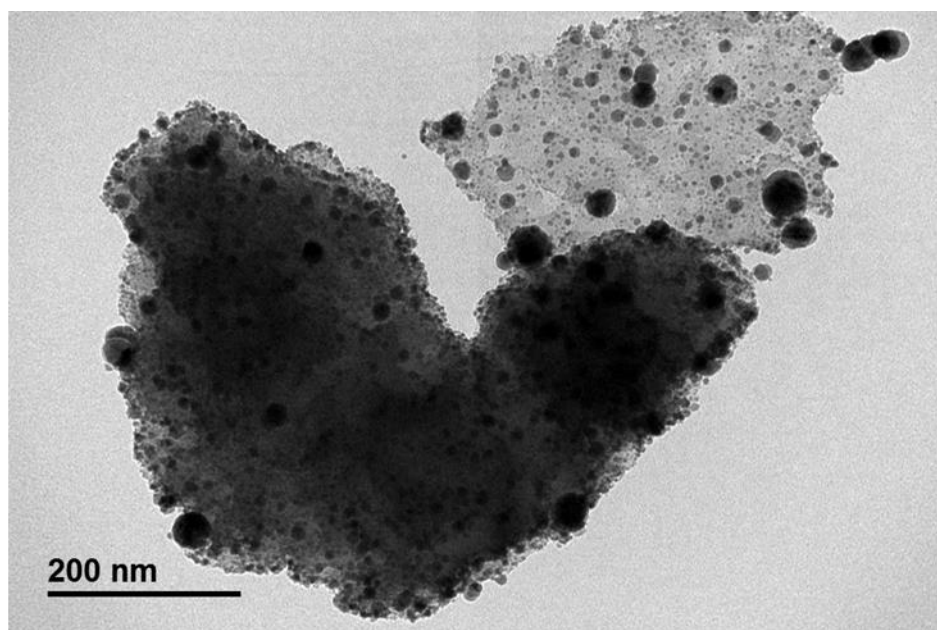


Figure 33. TEM images (A) of Pd@UiO-67 MOF crystal with 5% palladium by weight and (B) size distribution of palladium nanoparticles within UiO-67. The TEM image was obtained by Dr. Khaled Abozeid.

In figure 33A is the depiction of UiO-67 crystal with palladium nanoparticles on the nano MOF crystals. The average particle size of the palladium in figure 33A is approximately 7.2 ± 6.1

nm and large particles with 40 nm diameters are much more frequent compared to the 1% and 2% palladium by weight loadings. With higher concentration of palladium precursors, more agglomeration is observed and thus larger polydisperse particles. Ultimately larger particles lower the catalytic power for oxidation of benzyl alcohol, due to lower amount of active catalytic sites resulting from lower surface to volume ration of atoms on the particles.

4.3.6 Absorbance

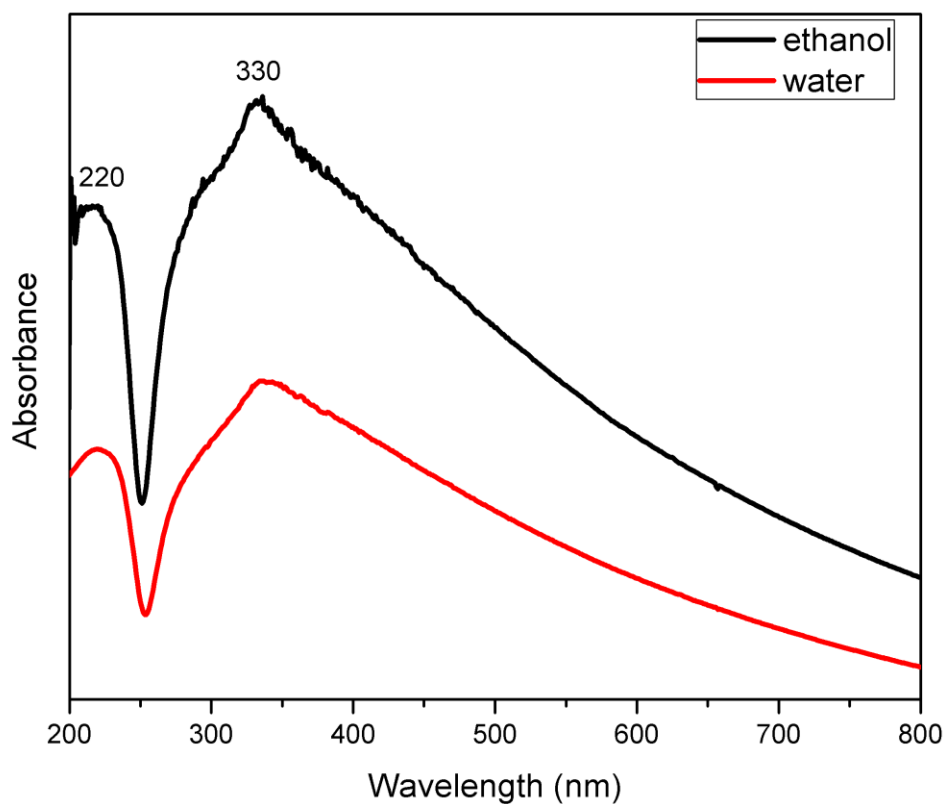


Figure 34. UV-Vis spectra of UiO-67 in ethanol (black) and water (red).

Depicted in figure 34 is UV-Vis absorbance of UiO-67 in various solutions. It can be seen that absorbance of UiO-67 is similar for ethanol and water with bands at 220 nm and 330 nm with a long absorption tail

after 330 nm. Such a wide absorption band of UiO MOF allows it to be easily excited with visible light to be further used as a photocatalyst in multitude of reactions^{139, 140}. The bandgap of UiO-67 has been calculated experimentally by Larsen¹⁴¹ to be 2.5 eV suggesting that the excitation wavelength is around 495 nm, which is well within the visible range and the absorbance of UiO-67 depicted in figure 34.

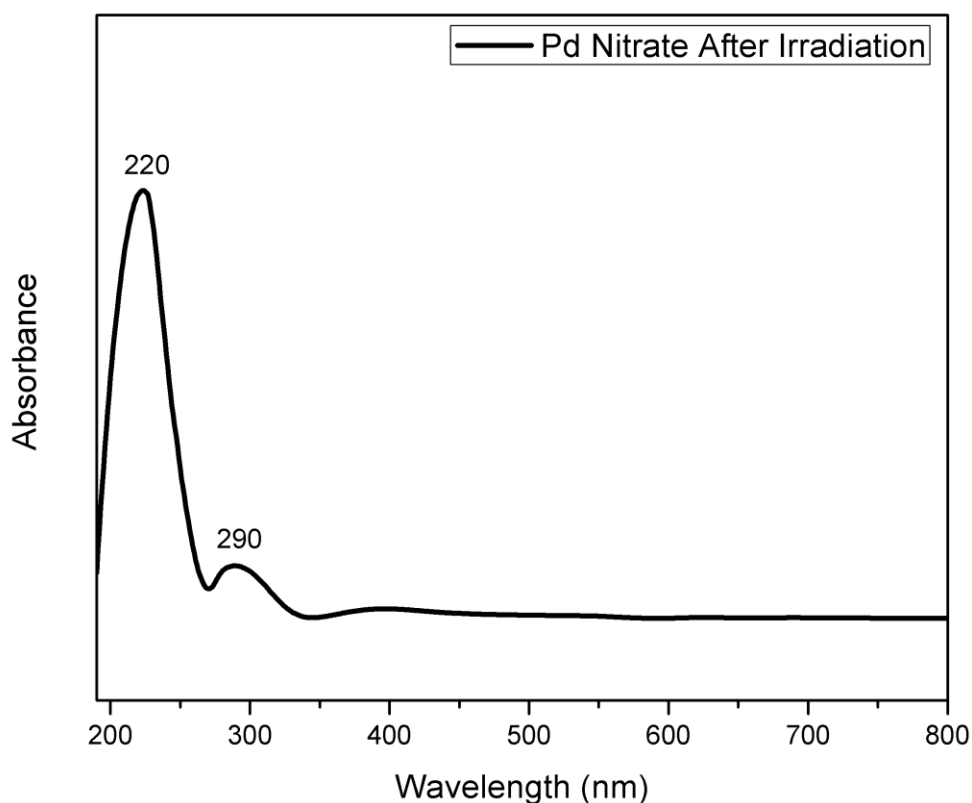


Figure 35. UV-Vis spectra of palladium nitrate after laser irradiation.

Absorbance of palladium nanoparticles after laser irradiation by Nd:YAG laser at 532 nm is depicted in figure 35. The absorbance of palladium nanoparticles was found to be similar to the literature published^{142, 143}. A small peak around 290 nm corresponds to electronic transition from n to π^* in the free nitrate ions in the solution. Another peak for nitrate appearing around 380 nm,

however is not visible in figure 34 due to its very small presence in the solution and major formation of palladium nanoparticles¹⁴⁴. Peak at 220 nm corresponds to absorption of square-planar palladium complex $\text{Pd}(\text{NO}_2)_4^{2-}$ according to literature published¹⁴⁴.

4.4 Benzyl Alcohol Oxidation Results

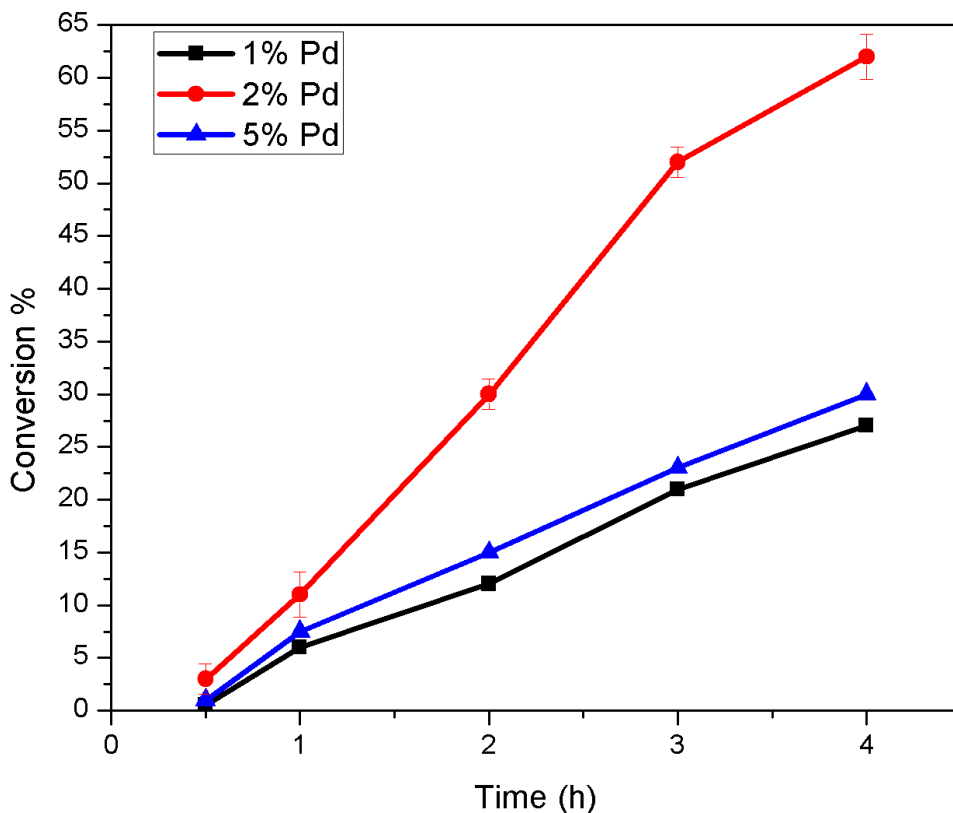


Figure 36. Mole conversion of benzyl alcohol into products versus time. Pd@UiO-67 MOFs were used as a catalyst with (blue) 1% palladium nanoparticles supported on UiO-67 (red) 2% palladium nanoparticles and (black) 5% palladium nanoparticles by weight.

Illustrated in figure 36 is the mole conversion of benzyl alcohol into its product – benzyl aldehyde. Finding an optimal palladium nanoparticle loading was critical for further reactions, therefore a range was chosen from 1% to 5% loading by weight with the middle point in 2%. After acquiring the transmission electron micrographs based on the dispersion and the size of the nanoparticles in the UiO-67 it was speculated that 1% Pd in figure 31A would give the highest possible conversion followed by 2% (figure 32A) and 5% (figure 33A) palladium loading by

weight. However in the figure 36 the highest conversion was achieved with 2% palladium by weight loading and 1% and 5% were very similar to each other in catalytic activity.

It can be seen that initially up until 1 hour mark the catalytic pathway is very similar. However, after the 1 hour mark there is a significant difference between the 2% and the other palladium weight loadings. It is possible that the reason why catalytic activity is higher for the 2% palladium loading compared to the other palladium loadings is because in case of 1% palladium loading there is a lower amount of palladium nanoparticles present which doesn't provide enough catalytically active sites for rapid benzyl alcohol conversion into benzaldehyde. In the case of 5% palladium loading there is a visible large agglomeration of palladium nanoparticles that can be seen in figure 33A with some ranging up to 50 nm in diameter. In comparison, the 1% palladium by weight Pd UiO-67 catalyst has nanoparticles that are roughly 10 nm in diameter and the 2% palladium loading by weight Pd UiO-67 catalyst has particle sizes in between 10 and 20 nm thus making them polydisperse. Small monodisperse particles are highly attractive due to their consistent size and good distribution throughout the sample. Polydisperse particles, especially in high surface area supports such as MOFs, can potentially damage the pores of the structures and aggregate with the neighboring nanoparticles thus minimizing the highly sought surface to volume ratio property of nanoparticles.

Before proceeding to further oxidation reactions, multiple runs for 2% palladium loading have been performed to verify the reproducibility of the results. It appeared that conversion varied by 2-3% for all time marks throughout the reaction as depicted in figure 36 error bars. Thus it was deemed safe to proceed with further reactions on 2% palladium loading Pd@UiO-67 catalyst.

Conversion of benzyl alcohol reaction was calculated based on the peak areas for products and reactants based on the following equation

$$\text{Conversion \%} = \frac{\text{Peak Area of Benzaldehyde}}{\text{Peak Area of Benzyl Alcohol} + \text{Peak Area of Products}} \times 100\% \quad (4)$$

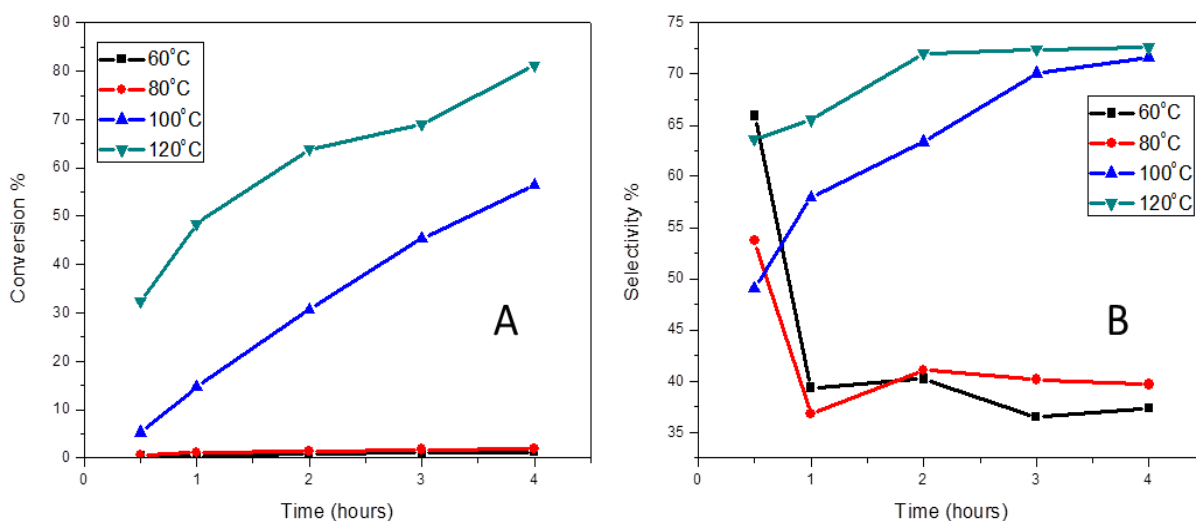


Figure 37. Influence of temperature on (A) mole conversion of benzyl alcohol and (B) selectivity for benzaldehyde at a constant pressure of 0.7 MPa.

Figure 37 illustrates temperature effect on the conversion of benzyl alcohol and selectivity towards benzaldehyde. It can be seen in figure 37A that at 60 and 80 °C there is almost no catalytic activity throughout the reaction whereas at 100 °C the conversion at 4 hour mark reaches 62 % at 0.7 Mpa of oxygen gas and at 120 °C conversion reaches 80%. At higher temperatures there is a significant increase of the initial rates and the conversion of benzyl alcohol at 120 °C at 1 hour mark is approximately the same as for 100 °C at the 3 hour mark. The

calculated turnover frequency listed in table 3 for the benzyl alcohol reaction at 120 °C is about 8500 h⁻¹ compared to 1453 h⁻¹ for the 100 °C oxidation of benzyl alcohol.

Selectivity illustrated in figure 37B for 60 and 80 °C samples start at 66% and 54% respectively but soon decrease to about 40% at the end of 4 hour mark. In case of 100 and 120 °C temperatures, the selectivity is significantly higher especially at 0.5 h mark for the 120 °C and at 4 hour mark the selectivities are roughly the same at about 73%. Selectivity for benzaldehyde at 120 °C reaction has decreased and remained similar to reaction at 100 °C because of benzoic acid formation. Interestingly enough, benzyl alcohol acts as an inhibitor for autoxidation of benzaldehyde caused by free radicals, thus intercepting them¹⁴⁵. As a result of higher temperature towards the 4 hour mark lower amounts of benzyl alcohol is left in the reaction and thus, there is a higher probability for benzaldehyde to undergo autoxidation into benzoic acid, which leads to lower selectivity for benzaldehyde even though conversion is higher. Additionally, water, which is a by-product of benzyl alcohol oxidation, can lead to overoxidation of alcohols producing benzoic acid bypassing the benzaldehyde intermediate¹⁴⁶. Considering that higher temperature leads to higher conversion of benzyl alcohol, higher quantities of water are formed and thus, higher probability that formed benzaldehyde will oxidize to benzoic acid.

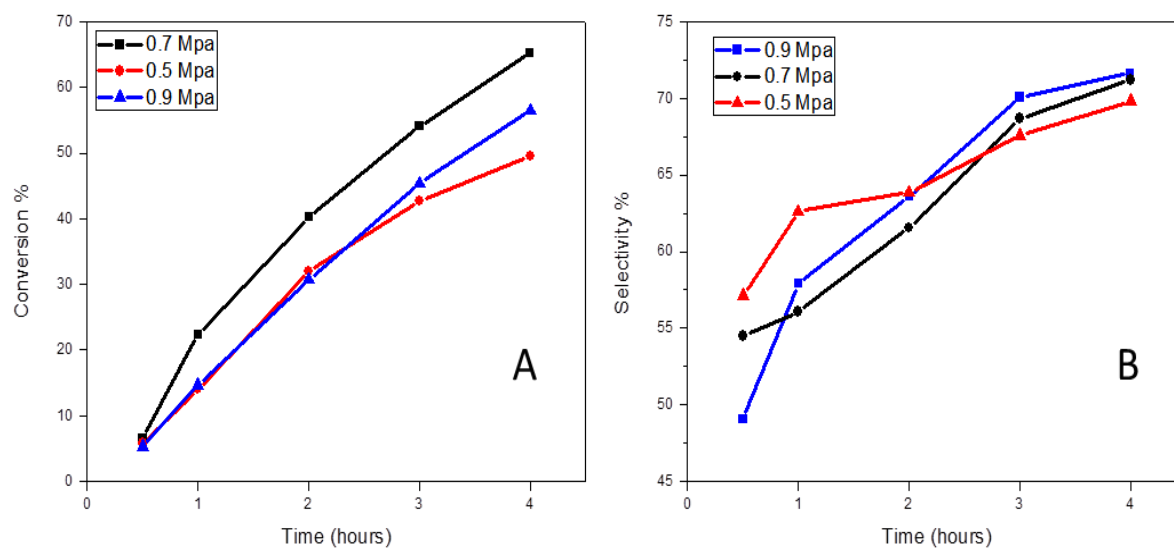


Figure 38. Influence of pressure on (A) mole conversion of benzyl alcohol and (B) selectivity for benzaldehyde at a constant temperature of 100 °C.

Figure 38 depicts effect of pressure on conversion and selectivity towards benzaldehyde. For the different pressures at constant reaction temperature of 100 °C illustrated in figure 38A the highest conversion and highest initial rate was achieved with 0.7 MPa pressure of oxygen gas, whereas the 0.5 and 0.9 MPa pressures had similar initial rates but at the 4 hour mark the selectivity for benzaldehyde slightly decreased. It is not exactly clear why 0.9 MPa pressure gives a lower conversion than a 0.7 MPa pressure.

Figure 38B illustrates that selectivity for benzaldehyde at constant temperature of 100 °C varied significantly at the 0.5 hour mark; however towards the 4 hour mark the differences in selectivity have become negligible, especially between the 0.7 and 0.9 MPa pressures.

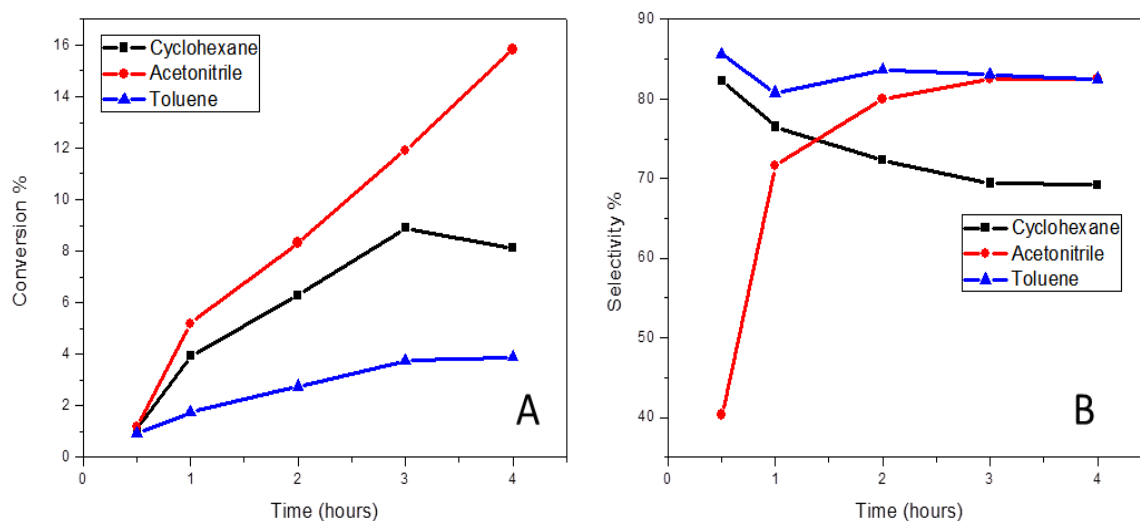


Figure 39. Influence of (A) solvent in the autoclave reactor on the mole conversion of benzyl alcohol and (B) selectivity for benzaldehyde.

With the effect of reaction solvent illustrated in figure 39 the conversion of benzyl alcohol decreased significantly in comparison to solvent-free reaction. Figure 39A illustrates that the highest % mole conversion of benzyl alcohol is 16% reached with acetonitrile solvent whereas in solvent-free reaction, the % mole conversion was 62% as depicted in figure 38A. The highest initial rates and conversion was observed with the acetonitrile solvent followed by cyclohexane and toluene solvent.

Selectivity for benzaldehyde was very similar using toluene and acetonitrile and slightly lower for cyclohexane. It is interesting to note that selectivity for benzaldehyde with use of solvent increases by around 10% specifically in the case of acetonitrile and toluene. In the case of cyclohexane, the selectivity is comparable to reaction of benzyl alcohol in solvent-free conditions. Depending on the solvent certain products can be extracted from the reactant mixture to increase selectivity for the desired product.

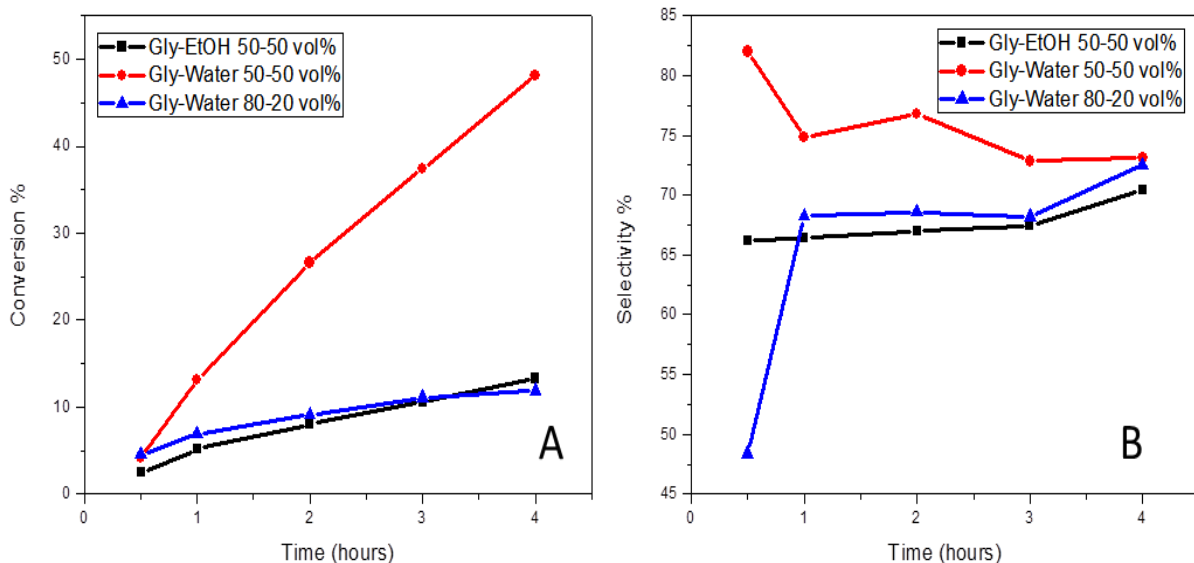


Figure 40. The effect of various reducing solvents during laser irradiation on the (A) mole conversion of benzyl alcohol and (B) selectivity for benzaldehyde.

In figure 40 different reducing media for palladium precursor were compared for the oxidation of benzyl alcohol. The best reducing media used for laser irradiation after ethanol is a 50% volume mixture of ethylene glycol and water (Figure 40A red), followed by 50% volume mixture of ethylene glycol-ethanol (Figure 40A black) and 80-20% volume mixture of ethylene glycol-water (Figure 40A blue). The conversion for 50% mixture ethylene glycol and water has the highest initial rates and highest conversion of 48%. The glycol-water 80/20 mixture was too viscous which caused poor dispersion of palladium precursor within the MOF and thus possibly lead to agglomeration of nanoparticles, blocking the pores and decreasing the available surface area for catalysis. The glycol-ethanol mixture didn't mix well within itself, which led to poor distribution of palladium precursors within the UiO-67 and thus to lower catalytic activity.

The selectivity for benzaldehyde illustrated in figure 40B was highest for 50% mixture between glycol and water (red) at 73% which slightly decreased from initial 83% due to higher

formation of toluene product. Selectivity towards benzaldehyde for other solvents were similar at the 4 hour mark but significantly lower at 0.5 hour mark. It is well established that different capping agents influence optical, mechanical and chemical properties of the nanoparticles^{147, 148}. Capping agents establish chemical bonds with the surface of the nanoparticles, however they can reduce the density of electrons on the surface of the metal particles, which can be crucial during catalysis. Ethylene Glycol used as a reducing medium would also act as a capping agent in this case and thus, would influence the activity towards benzyl alcohol oxidation. Ethanol, as a reducing solvent, provided the highest conversion of benzyl alcohol partly because it didn't cap the nanoparticles and thus didn't alter the surface chemistry of palladium nanoparticles anchored to the UiO-67 MOF.

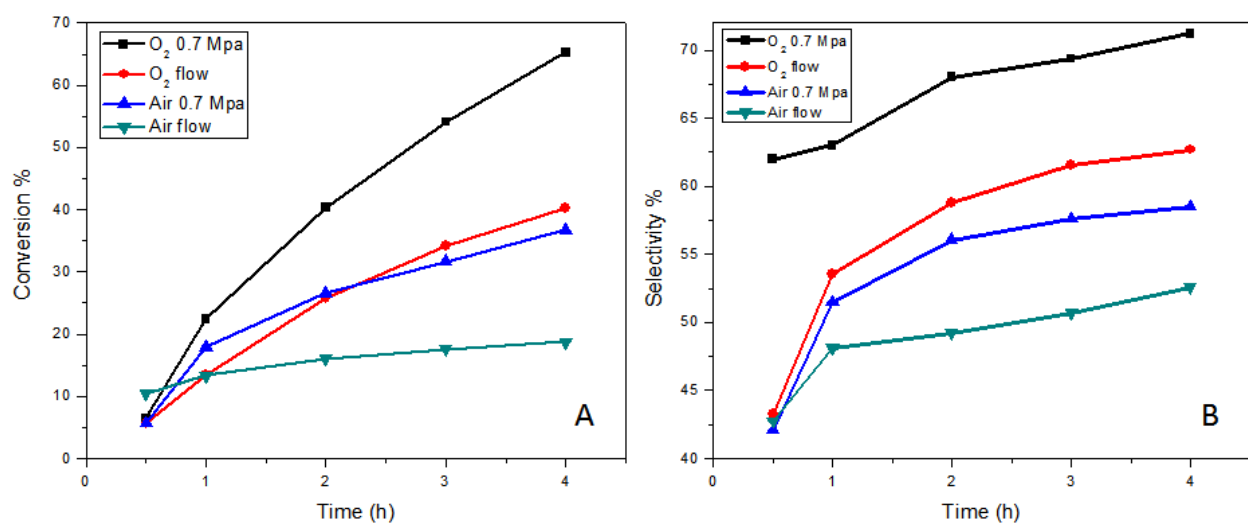


Figure 41. Influence of (black) compressed oxygen at 0.7 Mpa (red) oxygen flow (blue) compressed air and (green) air flow at 1 atm on conversion of (A) benzyl alcohol and (B) selectivity for benzaldehyde.

Illustrated in figure 41 is the comparison of two oxidants: oxygen and air oxidation of benzyl alcohol in the autoclave reactor. From figure 41A the highest conversion at the 4 hour

mark of the reaction was achieved with compressed oxygen gas at 0.7 Mpa pressure followed by oxygen flow at 1 atm, compressed air at 0.7 Mpa and air flow at 1 atm pressure. It is interesting to note that the TOF was the highest for the air flow (green) conversion at 0.5 h mark which is around 1850 h^{-1} compared to 984 h^{-1} for compressed air at 0.7 Mpa pressure, 988 h^{-1} for oxygen flow at 1 atm and 1453 h^{-1} for 0.7 Mpa compressed oxygen gas.

Since the active oxidant specie in benzyl alcohol oxidation reaction is molecular oxygen, it seems reasonable to assume that with higher amounts of oxygen, conversion of benzyl alcohol would be higher as what has been observed in figure 41A.

Similarly, selectivity for benzaldehyde illustrated in figure 41B was the highest for compressed oxygen flow at 0.7 MPa pressure with roughly 72% selectivity at the 4 hour mark followed by 63% for oxygen flow at 1 atm, 57% for compressed air at 0.7 MPa and 52% for air flow at 1 atm. Selectivity for benzaldehyde with 0.7 MPa compressed oxygen gas was significantly higher at the 0.5 hour mark compared to the other gas mixtures used in the reaction. It can be speculated that with lower amount of molecular oxygen present in the system, benzyl alcohol is being oxidized favorably to toluene, however with higher concentration of oxygen, benzyl alcohol is oxidized to benzaldehyde.

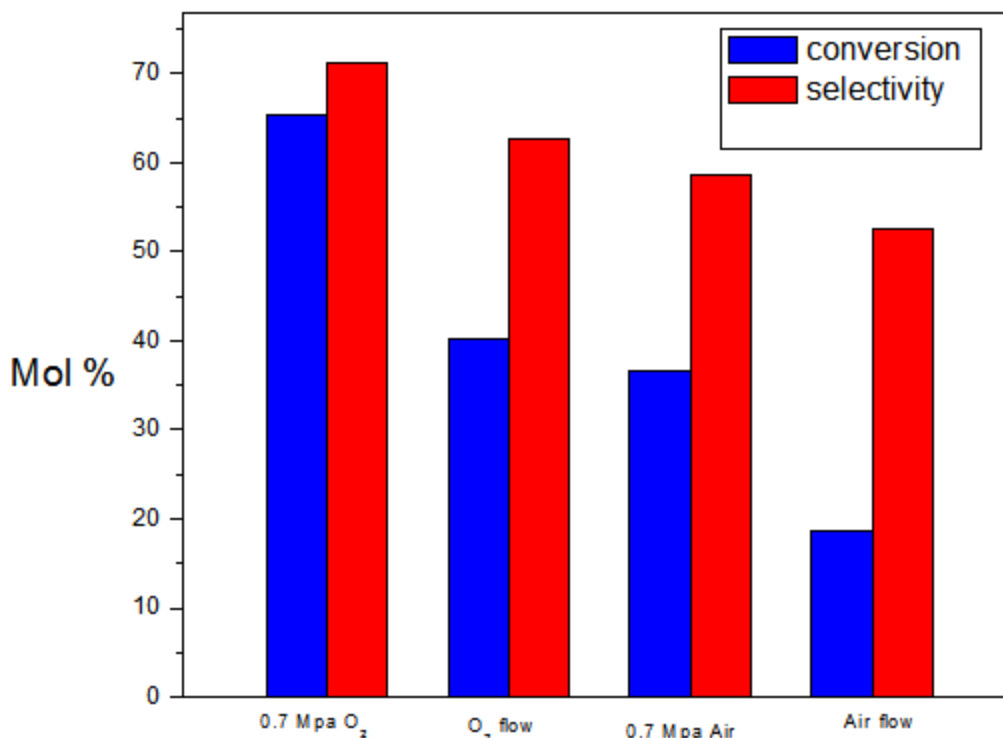


Figure 42. Scale bar representation of (blue) benzyl alcohol conversion and (red) benzaldehyde selectivity with 0.7 Mpa oxygen gas, oxygen flow at 1 atm, 0.7 Mpa air and with air flow at 1 atm at 4 hour time mark.

Figure 42 illustrates in a bar representation the conversion (blue) of benzyl alcohol and selectivity (red) toward benzaldehyde. The highest conversion of benzyl alcohol and selectivity is obtained in a reaction with molecular oxygen at 0.7 MPa pressure, followed by oxygen gas at atmospheric pressure, dry pressurized air at 0.7 MPa and air at atmospheric pressure. It is interesting to note that the conversion and selectivity between the flow of oxygen at ambient pressure and compressed dry air at 0.7 MPa are similar.

Illustrated in table 5 is the summary of all the reactions performed on oxidation of benzyl alcohol in the autoclave reactor. The highest conversion of benzyl alcohol was achieved with 2% palladium by weight Pd@UiO-67 at 120 °C with 81% and with a turnover frequency of 8434 h⁻¹.

It is interesting to note that the turnover frequency between the air flow at ambient pressure and compressed oxygen gas at 0.7 MPa is higher – 1841 h⁻¹ vs 1453 h⁻¹. This is attributed to the fact that turnover frequency was measured during the first 30 minutes of the reaction, and the benzyl alcohol conversion with air flow at 0.5 hour mark was higher compared to the conversion with compressed oxygen at 0.7 MPa.

The turnover frequency reported in table 5 depends on moles of benzaldehyde and moles of palladium present in the reaction mixture at certain time and was calculated as follows:

$$\text{TOF} = \frac{\text{Moles of Benzaldehyde}}{(\text{Moles of Palladium in Pd@UiO-67}) \times 0.5 \text{ h}} \quad (5)$$

where turnover frequency was calculated at 0.5 hour mark of the reaction. Equation 5 is not an accurate equation for calculating the TOF number for benzyl alcohol oxidation reaction. The reasoning lies in the fact that only surface atoms of palladium participate in the catalysis, whereas palladium atoms inside the core of the particles are idle. Therefore a more accurate equation would have number of active sites of palladium multiplied by unit of time in the denominator. However, it is quite difficult to calculate the number of active sites on palladium nanoparticles due to their different sizes and random allocation throughout the structure of UiO-67. Palladium nanoparticles can be blocked by the collapsed pore or by another palladium particle residing in close proximity. The turnover frequency provides reader with information on how many molecules of benzyl alcohol are converted over moles of palladium per hour. For example, a TOF of 8434 h⁻¹ represents that 8434 molecules of benzyl alcohol are converted into benzaldehyde over one mole of palladium in one hour.

Comparison has been made with different solvents to observe the effect of solvent on the oxidation rate of benzyl alcohol and is presented in the table below. In general, solvent has led to

a decreased oxidation of benzyl alcohol, but has slightly increased selectivity towards benzaldehyde, thus having lower amounts of unnecessary byproducts from the oxidation reaction. Solvents help extract benzaldehyde into a different liquid phase because of different solubilities of reactants and products. Once benzaldehyde is extracted by the solvent, it won't be overoxidized further into benzoic acid. Typical solvents used in benzyl alcohol oxidation include n-heptane, n-hexane, ethanol, methanol, water, acetonitrile and trifluorotoluene¹⁴⁹. Pristine UiO-67 was run with benzyl alcohol in the reactor to observe if the metal-organic framework has any catalytic activity. With UiO-67 catalyst, 1.96 % conversion was reached for benzyl alcohol at the end of the 4 hour mark with 68.9% selectivity towards benzaldehyde.

Further studies could include PVP-capped palladium nanoparticles and be tested for benzyl alcohol oxidation to see if there is any metal-support interaction between the metal catalysts and the UiO-67 MOF. Additionally, palladium particles capped with different capping agents could be tested for oxidation of benzyl alcohol. Using the same capping agents, UiO-67 MOF can be grown around the formed nanoparticles and then tested for benzyl alcohol oxidation. The latter choice would be very promising due to pore size restriction on nanoparticle growth, thus making palladium nanoparticles smaller than the pore size of UiO-67 (less than 2.5 nm) and monodisperse. Use of palladium acetate as a precursor could be a better choice to avoid nitrate ions that result in reaction between nitrous/nitric species and the zirconium-nodes, ultimately leading to framework collapse.

Table 5. Summary of benzyl alcohol reactions performed in different conditions.

Catalyst@UiO-67	Conversion ^a %	Selectivity ^a %	T °C	P (MPa)	Gas	Reactor Solvent	Reducing Solvent	TOF (h ⁻¹)
1% Pd	27	9.61	100	0.9	O ₂	--	EtOH	230
2% Pd	62	71.64	100	0.9	O ₂	--	EtOH	603
5% Pd	30	60.25	100	0.9	O ₂	--	EtOH	69
2% Pd	65.27	71.20	100	0.7	O ₂	--	EtOH	1453
2% Pd	81.11	72.60	120	0.7	O ₂	--	EtOH	8434
2% Pd	49.48	69.82	100	0.5	O ₂	--	EtOH	1348
2% Pd	1.91	39.69	80	0.9	O ₂	--	EtOH	148
2% Pd	1.18	37.31	60	0.9	O ₂	--	EtOH	154
2%Pd	18.77	52.59	100	0.7	Air	--	EtOH	984
2%Pd	36.69	58.52	100	0.1	Air	--	EtOH	1841
2%Pd	40.16	62.70	100	0.1	O ₂	--	EtOH	988
2%Pd	8.11	82.30	100	0.7	O ₂	Cyclohexane	EtOH	375
2%Pd	15.82	82.51	100	0.7	O ₂	Acetonitrile	EtOH	198
2%Pd	3.89	82.52	100	0.7	O ₂	Toluene	EtOH	324
2%Pd ^b	13.29	70.39	100	0.7	O ₂	--	Gly-EtOH	675
2%Pd ^c	11.86	72.53	100	0.7	O ₂	--	Gly-H ₂ O	897
2%Pd ^d	48.13	73.12	100	0.7	O ₂	--	Gly-H ₂ O	1400
Parent Material	1.96	68.88	100	0.7	O ₂	--	--	

a- Conversion and selectivity after 4 hours

b- Ethylene-glycol – ethanol 50-50 volume ratio mixture

c- Ethylene glycol – water 80-20 volume ratio mixture

d- Ethylene glycol-water 50-50 volume ratio mixture

Illustrated in table 6 are list of catalysts consisting of noble metal nanoparticles supported on metal-organic frameworks tested for benzyl alcohol oxidation. It can be seen that majority of catalysts demonstrate excellent conversion and chemoselectivity towards benzaldehyde. However, it is very difficult to compare the literature to Pd@UiO-67 catalyst system due to very different reaction conditions, various moles of substrate used, different metal-organic frameworks and scarcity of literature on palladium nanoparticles encaged in MOFs for benzyl alcohol reaction.

The highest conversion and selectivity for benzaldehyde are demonstrated by Liu¹⁵⁰ and Chen¹⁵¹ where reaction was carried out by using MIL-101 and UiO-67 catalyst supports in

toluene solvent using oxygen or air as oxidants. It is clear that solvent has a significant influence on selectivity towards benzaldehyde. Solvent hinders the production of toluene from benzyl alcohol oxidation reaction and promotes benzaldehyde as the desirable intermediate. Other notable entry is oxidation reaction done by Luan¹⁵² where he used DMF as solvent and Au/UiO-66-NH₂ as a catalyst. His group managed to achieve 94% conversion after 1 hour mark of reaction with 99% selectivity towards benzaldehyde. Zhu¹⁵³ and co-workers have tested Au/UiO-66 in solvent-free oxidation of benzyl alcohol and have demonstrated that benzaldehyde was the only product formed from the reaction. They have also managed to reuse the catalyst up to 8 times without significant drop in conversion and without leaching of gold into the system. Tilgner and co-workers¹⁵⁴ have synthesized Pd/TiO₂@MIL-101 catalysts and have tested it for alcohol dehydrogenation reactions. For benzyl alcohol oxidation, they reported achieving 96% conversion with 58% selectivity towards benzaldehyde after 24 hours at 90 °C in inert atmosphere at ambient pressure. Xinle¹⁵⁵ have demonstrated excellent conversion of benzyl alcohol into benzaldehyde by synthesizing Pd@UiO-66-NH₂ catalyst and testing it for oxidation reaction. Reported conversion of benzyl alcohol reached 98.7% with 58% selectivity towards benzaldehyde after 24 hour reflux reaction at 90 °C at 0.1 MPa oxygen gas pressure. The catalyst has been tested for reusability and conversion remained virtually unchanged after 5 catalytic cycles. Chen¹⁵⁶ and co-workers reported 95% conversion of benzyl alcohol with 99% chemoselectivity to benzaldehyde after 25 hour reaction at 130 °C under ambient air conditions. This group used palladium loaded Cu(II) MOF catalyst which was successfully recycled for benzyl alcohol oxidation reaction up to 6 times without significant loss in conversion and selectivity. Hossain¹⁵⁷ reported 88% conversion of benzyl alcohol with 88% selectivity to benzaldehyde after 5.5 hour reaction under air at 85 °C in by catalyzing the reaction over

Pd@MOF-3 catalyst. The catalyst was successfully recycled up to 2 times with minor loss in conversion and selectivity to benzaldehyde.

Despite that a lot of catalysts had 100% selectivity towards benzaldehyde with similar conversion of benzyl alcohol, our system had a much higher mole ratio of substrate to catalyst – 21000. Chen and co-workers had a higher ratio, however their reaction lasted for 25 hours and at higher temperature in liquid phase solvent of xylene. The Pd@UiO-67 system was used in a solvent-free reaction and majority of product was converted by the end of 4 hour mark. It is very probable to have close to 100% conversion with a longer reaction time and thus the Pd@UiO-67 is a very promising catalyst for benzyl alcohol oxidation.

Table 6. Comparison of the Pd UiO-67 catalyst with other noble metal based MOF catalysts for benzyl alcohol oxidation.

Catalyst	Conversion %	Selectivity % for benzaldehyde	Time (h)	Temp °C	Pressure (atm)	Solvent	Oxidant	Mol subst/mol catalyst	Ref.
Au@UiO-66-NaBH ₄	94	100	9.5	100	5	Toluene	O ₂	50	Leus ¹⁵⁸
Au@UiO-66-NaBH ₄	83	100	23	100	5	Toluene	Air	50	Leus ¹⁵⁸
Au@UiO-66	53.8	100	10	80	1	None	O ₂	n/a	Zhu ¹⁵³
Au@MIL-101	99	99	n/a	80	1	Toluene	O ₂	0.001	Liu ¹⁵⁰
Pd@MIL-101	99	99	1.5	80	1	Toluene	O ₂	0.001	Chen ¹⁵⁹
Pd@UiO-67	99	99	20	100	1	Toluene	Air	0.001	Chen ¹⁵¹
Au@UiO-66-NH ₂	94	99	1	100	1	DMF	O ₂	0.001	Luan ¹⁵²
Au@PMA-MIL-101	60	100	n/a	80	1	Toluene	Air	n/a	Juan-Alcaniz ¹⁶⁰
Pd/TiO ₂ @MIL-101	96	58	24	90	1	None	Inert	n/a	Tilgner ¹⁵
Pd@UiO-66-NH ₂	98.7	45.9	22	90	1	Toluene	O ₂	100	Xinle ¹⁵⁵
Pd@Cu(II)-MOF	95	99	25	130	1	Xylene	Air	22300	Chen ¹⁵⁶
Pd@MOF-3	88	88	5.5	85	1	Toluene	Air	n/a	Hossain ¹⁵⁷
Pd@UiO-67	62	70	4	100	7	None	O ₂	21000	This Work

CHAPTER 5

5.1 Concluding Remarks

The SiO_x-RGO catalysts have been successfully prepared through LVCC process by laser irradiation of mixture of bulk silicon and graphene oxide powder in inert atmosphere of helium. The resultant solid was collected and was dispersed in water solution with further addition of palladium nitrate together with reducing hydrazine hydrate agent. The mixture was subject to microwave irradiation and was dried in the oven overnight. Different mixtures of silicon and graphene oxide supports were examined for the catalytic efficacy towards Suzuki-Miyaura and Sonogashira cross-coupling reaction. Additionally, catalysts were characterized through different techniques including UV-Vis absorbance, photoluminescence, FTIR, Raman spectroscopy, x-ray diffraction, electron microscopy and x-ray photoelectron spectroscopy.

These characterization techniques provided evidence for presence of silicon and graphene oxide in the catalyst supports and presence of different oxidized species of palladium nanoparticles on the surfaces of the support. UV-Vis spectroscopy confirmed the presence of silicon nanoparticles by showing a long tail absorbing from 400 nm corresponding to indirect band gap of silicon and peak around 260 nm corresponded to silicon's direct bandgap L to L' transition. FTIR has showed Si-O-Si stretches around 1080 cm⁻¹ and peaks around 450 cm⁻¹ corresponding to silicon. Raman spectroscopy has demonstrated the presence of silicon from the 514 cm⁻¹ peak corresponding to transverse optical phonon of silicon. Furthermore, peaks around 1350 and 1500 cm⁻¹ were attributed to the D and G bands demonstrating presence of reduced graphene oxide. X-ray diffraction confirmed the presence of silicon and palladium present in the sample where peaks of 29, 47, 56, 69, 76 and 88° were attributed to silicon lines of 111, 220, 311, 400, 311, 422 respectively and a small line at 39° was attributed to the palladium 111 line.

XPS has provided the presence of multiple palladium species in the sample with oxidation states of 0, +2 and +4. Moreover, electron microscopy has confirmed presence of palladium nanoparticles on the surface of the supports with different size distributions ranging from 5.8 ± 3.7 to 7.4 ± 4.0 nm.

The catalysts have been tested for Suzuki-Miyaura and Sonogashira carbon cross-coupling reactions with varying loading amounts of silicon and reduced graphene oxide. The results have shown that the highest catalytic efficiency was achieved with SiO_x -Pd sample due to the higher presence of palladium 0 in the sample. Additionally, the same catalyst was tested for Sonogashira cross-coupling reactions using iodobenzene and bromobenzene and the conversion was 100 and 80% respectively to produce diphenylacetylene.

The Pd@UiO-67 catalysts have been successfully prepared by synthesizing UiO-67 metal-organic framework and impregnating palladium nanoparticles through pulsed laser irradiation. The resulting catalyst was dried in the oven overnight and was later characterized by FTIR spectroscopy, x-ray diffraction, nitrogen adsorption measurements and electron microscopy. The FTIR has revealed several peaks corresponding to the UiO-67 MOF. Peak at 1674 cm^{-1} was attributed to DMF that was present in the freshly prepared UiO-67 but disappearing later during the palladium impregnation process. Doublet around 1405 and 1600 cm^{-1} was attributed to carboxylate group stretches from the BPDC linker and peak at 1180 cm^{-1} was attributed to C-H bond originating from the BPDC as well. Peaks from 1500 to 1550 cm^{-1} were attributed to aromatic C-C bond originating from the organic linker. The inorganic node peaks were observed around 663 and 701 cm^{-1} corresponding to longitudinal and transverse modes of ZrO_2 . X-ray

diffraction peaks for UiO-67 appear at 6, 7, 9, 11, 13, 17, 20, 25, 27° corresponding to 111, 200, 220, 222, 400, 311, 600, 642, 731 lines respectively. Diffraction peaks remained at the same angles verifying presence of UiO-67 metal-organic framework during post-synthetic impregnation of UiO-67 and after the reaction. BET surface area measurement of pristine UiO-67 have showed a surface area of 2591 m² g⁻¹ which was similar to literature values published and was slightly lower compared to its theoretical surface area of 3000 m² g⁻¹. However, the surface area of Pd@UiO-67 was measured to be 317 m² g⁻¹ and was significantly lower compared to published literature values. Furthermore, the pore size distribution of the Pd@UiO-67 showed a sharp peak around 1-2 Å corresponding to bond lengths between atoms, whereas for the pristine UiO-67 two main pore sizes of 15 and 25 Å were observed corresponding to tetrahedral and octahedral holes respectively. Electron microscopy has been performed on the UiO-67 samples loaded with palladium nanoparticles and the particle size ranged from 4.1 ± 2.5 to 7.2 ± 6.1 nm in diameter with a few particles larger than 40 nm in size. Except for the 1% palladium loading, majority of the palladium nanoparticles were polydisperse.

The Pd@UiO-67 catalysts with different loadings of palladium have been tested for benzyl alcohol oxidation reaction. Throughout different temperatures, pressures and solvents used the highest mole conversion of 81% was observed at 120 °C under 0.7 MPa pressure with 2 wt% palladium loading. The catalyst has been tested for air oxidation and performed well achieving 30% conversion at the 4 hour mark of the reaction at 100 °C. Furthermore, the catalyst has been tested for the reusability and was recycled up to 3 times with the increasing conversion but lower selectivity towards benzaldehyde. The Pd@UiO-67 catalyst was compared to the published

literature and it provides an excellent catalytic activity towards benzyl alcohol oxidation with a TOF of 8434 h^{-1} .

5.2 Future Research

Further research can be done for studying the Pd/SiO-RGO catalysts and Pd@UiO-67. Performing XPS measurements on silicon oxidation for the SiO_x-RGO could explain why palladium is mostly in 0 oxidation state compared in SiO_x-RGO catalyst support with higher silicon ratio. Microscopy images could show the particle size distribution of palladium nanoparticles on the SiO_x support and XPS would reveal its oxidation state aiding in understanding of catalytic power towards carbon cross-coupling reactions. Performing ICP analysis on the catalyst samples before and after reaction would demonstrate the amount of palladium presence and further revealing if palladium leaching is present during the reaction.

For Pd@UiO-67 system further research needs to be done in the area of reusability of the catalyst. Additionally, ICP analysis would demonstrate the actual amount of palladium in the UiO-67 MOF before the reaction and after the reaction explaining the presence or absence of palladium leaching into the reaction mixture. XPS measurements need to be made to examine the oxidation state of palladium nanoparticles and thus gain more insight about which palladium species contributes towards oxidation of aromatic alcohol and which method of catalyst preparation would deem more desirable for the reaction. Thorough investigation needs to be done for finding the correct loading of palladium nanoparticles inside the UiO-67 framework without causing its collapse. One possible way of loading palladium nanoparticles into the pores of the MOF, would be synthesizing surfactant-capped palladium nanoparticles and mixing them

together with the UiO-67 precursors allowing the metal-organic framework to grow around the particles. This would ensure the limited growth of palladium nanoparticles due to pore size restriction allowing for maximum possibility to exploit the high surface to volume ratio of atoms in nanoparticles. Furthermore, pore size of the UiO-67 MOF would prevent aggregation and thus preserve the unique properties of nanoparticles for catalysis. Electron microscopy and particle size distribution would confirm the size of palladium nanoparticles and would show its size distribution. Correct washing procedure using supercritical CO₂ could be used to ensure absence of DMF and unreacted ligands in the pores of UiO-67 which would lower the available sites for palladium impregnation and thus lower the overall surface area of the MOF. Different palladium precursors need to be used for palladium impregnation into UiO-67 framework and surface area be measured to get valuable insight and understanding of which palladium precursor would not trigger the collapse of the framework. After establishing the optimal procedure for synthesizing Pd@UiO-67, the catalyst could be used to test benzylic alcohols for their oxidation and comparison could be made between the tested alcohols with their conversion and selectivity for the desirable product.

Increasing the surface area of the support allows for a higher quantity of available anchoring sites for the nanoparticles. Removing linkers from metal-organic frameworks creates a vacancy spot that could be filled with either adsorbed gas or particles for catalysis. Because of the missing linker, porosity of the materials increases. Furthermore, because of the missing linker the mass of metal-organic framework decreases while its surface area increases. However, removing a linker from MOF can compromise its mechanical and chemical stability. Wu and co-workers¹⁶¹ have successfully studied the effect of missing linker defect in UiO-66 and how its surface area increases. It was reported that UiO-66 theoretical porosity and surface area of 0.426 cm³ g⁻¹ and

954 m² g⁻¹ respectively can be significantly increased to a pore volume of 0.502 cm³ g⁻¹ and surface area of 1433 m² g⁻¹. Because Zr-MOFs are 12-coordinated it was speculated that its stability will not be compromised if only 1 linker will be systematically removed from 12 surrounding the inorganic node. Wu and his colleagues used acetic acid as a modulator and have managed to achieve a higher increase in surface area than what was theoretically sought – 1620 m² g⁻¹ with porosity of 0.65 cm³ g⁻¹. It was speculated that acetic acid was not only acting as a modulator but it was promoting the defect formation by terminating metal centers and thus restricting the BDC linkers from binding. Considering that UiO-67 is isorecticular to UiO-66 differing only in the linker length, it would be interesting to see how acetic acid would affect the surface area of UiO-67 and catalysis of benzyl alcohol oxidation. Higher porosity and surface area would allow for higher particle distribution of the UiO-67 MOF and theoretically for a higher catalytic power of palladium nanoparticles towards oxidation of benzyl alcohol.

LIST OF REFERENCES

1. Puglia, C.; Bonina, F., Lipid nanoparticles as novel delivery systems for cosmetics and dermal pharmaceuticals. *Expert Opin. Drug Deliv.* **2012**, 9, 429-441.
2. Kamaly, N.; Xiao, Z.; Valencia, P. M.; Radovic-Moreno, A. F.; Farokhzad, O. C., Targeted polymeric therapeutic nanoparticles : design, development and clinical translation. *Chem. Soc. Rev.* **2012**, 41, 2971-3010.
3. Reddy, H. L.; Arias, J. L.; Nicolas, J.; Couvreur, P., Magnetic Nanoparticles: Design and Characterization, Toxicity and Biocompatibility, Pharmaceutical and Biomedical Applications. *Chem. Rev.* **2012**, 112, 5818-5878.
4. Dhakshinamoorthy, A.; Garcia, H., Catalysis by metal nanoparticles embedded on metal–organic frameworks. *Chemical Society Reviews* **2012**, 41, 5262-5284.
5. Stratakis, M.; Garcia, H., Catalysis by Supported Gold Nanoparticles: Beyond Aerobic Oxidative Processes. *Chem. Rev.* **2012**, 112, 4469-4506.
6. Kawasaki, H., Surfactant-free solution-based synthesis of metallic nanoparticles toward efficient use of the nanoparticles' surfaces and their application in catalysis and chemo-/biosensing. *Nanotechnology Reviews* **2013**, 2, 5-25.
7. Saunders, B. R., Hybrid polymer/nanoparticle solar cells: Preparation, principles and challenges. *J. Coll. Interf. Sc.* **2012**, 369, 1-15.
8. Sun, C.; Su, J.; Wang, X., A Design of Thin Film Silicon Solar Cells Based on Silver Nanoparticle Arrays. *Plasmonics* **2015**, 10, 633-641.
9. Chen, G.; Seo, J.; Yang, C.; Prasad, P. N., Nanochemistry and nanomaterials for photovoltaics. *Chem. Soc. Rev.* **2013**, 42, 8304-8338.
10. Park, H.; Lee, S.; Lee, J.; Nam, S.; Jeon, T.; Han, S.; Kim, S., High Performance Organic Photovoltaics with Plasmonic-Coupled Metal Nanoparticle Clusters. *ACS Nano* **2014**, 8, 10305-10312.
11. Wang, H.; Dai, H., Strongly coupled inorganic–nano-carbon hybrid materials for energy storage. *Chem. Soc. Rev.* **2013**, 42, 3088-3113.
12. Yang, K.; Huang, X.; Huang, Y.; Xie, L.; Jiang, P., Fluoro-Polymer@BaTiO₃Hybrid Nanoparticles Prepared via RAFT Polymerization: Toward Ferroelectric Polymer Nanocomposites with High Dielectric Constant and Low Dielectric Loss for Energy Storage Application. *Chem. Mat.* **2013**, 25, 2327-2338.
13. Vivero-Escoto, J. L.; Huxford-Phillips, R. C.; Lin, W., Silica-based nanoprobe for biomedical imaging and theranostic applications. *Chem. Soc. Rev.* **2012**, 41, 2673-2685.
14. Chevrier, D. M.; Chatt, A.; Zhang, P., Properties and applications of protein-stabilized fluorescent gold nanoclusters: short review. *J. Nanophot.* **2012**, 6, 64504-1 - 64504-16.
15. Shen, J.; Zhao, L.; Han, G., Lanthanide-doped upconverting luminescent nanoparticle platforms for optical imaging-guided drug delivery and therapy. *Adv. Drug Deliv. Rev.* **2013**, 65, 744-755.
16. Ye, M.; Gong, J.; Lai, Y.; Lin, C.; Lin, Z., High-Efficiency Photoelectrocatalytic Hydrogen Generation Enabled by Palladium Quantum Dots-Sensitized TiO₂Nanotube Arrays. *J. Am. Chem. Soc.* **2012**, 134, 15720-15723.
17. Kloeffer, C.; Loss, D., Prospects for Spin-Based Quantum Computing in Quantum Dots. *Ann. Rev. Cond. Matt. Phys.* **2013**, 4, 51-81.
18. Jones, C. N.; Meter, R.; Fowler, A. G.; McMahon, P. L.; Kim, J.; Ladd, T. D.; Yamamoto, Y., Layered Architecture for Quantum Computing. *Phys. Rev. X* **2012**, 2.
19. Veldhorst, M.; Hwang, J. C. C.; Yang, C. H.; Leenstra, A. W.; de Ronde, B.; Dehollain, J. P.; Muhonen, J. T.; Hudson, F. E.; Itoh, K. M.; Morello, A.; Dzurak, A. S., An addressable quantum dot qubit with fault-tolerant control-fidelity. *Nat. Nanotech.* **2014**, 9, 981-985.

20. Shen, J.; Zhu, Y.; Yang, X.; Li, C., Graphene quantum dots : emergent nanolights for bioimaging, sensors, catalysis and photovoltaic devices. *Chem. Comm.* **2012**, 48, 3686-3699.
21. Zhu, S.; Meng, Q.; Wang, L.; Zhang, J.; Song, Y.; Jin, H.; Zhang, K.; Sun, H.; Wang, H.; Yang, B., Highly Photoluminescent Carbon Dots for Multicolor Patterning, Sensors, and Bioimaging. *Angew. Chem. Int. Ed.* **2013**, 52, 3953-3957.
22. Wu, P.; Yan, X.-P., Doped quantum dots for chemo/biosensing and bioimaging. *Chem. Soc. Rev.* **2013**, 42, 5489-5521.
23. Weng, M.; Ju, S., CO Oxidation Mechanism on Tungsten Nanoparticle. *J. Phys. Chem. C* **2012**, 116, 18803-18815.
24. Zhang, M.; de Respinis, M.; Frei, H., Time-resolved observations of water oxidation intermediates on a cobalt oxide nanoparticle catalyst. *Nat. Chem.* **2014**, 6, 362-367.
25. Mitsudome, T.; Kaneda, K., Gold nanoparticle catalysts for selective hydrogenations. *Green Chem.* **2013**, 15, 2636-2654.
26. Hudson, R.; Hamasaka, G.; Osako, T.; Yamada, Y. M. A.; Li, C.-J.; Uozumi, Y.; Moores, A., Highly efficient iron(0) nanoparticle -catalyzed hydrogenation in water in flow. *Green Chem.* **2013**, 15, 2141-2148.
27. Hou, W.; Cronin, S. B., A Review of Surface Plasmon Resonance-Enhanced Photocatalysis. *Adv. Func. Mat.* **2013**, 23, 1612-1619.
28. Sarina, S.; Wacławik, E. R.; Zhu, H., Photocatalysis on supported gold and silver nanoparticles under ultraviolet and visible light irradiation. *Green Chem.* **2013**, 15, 1814-1833.
29. Ranu, B. C.; Dey, R.; Chatterjee, T.; Ahammed, S., Copper Nanoparticle-Catalyzed Carbon-Carbon and Carbon-Heteroatom Bond Formation with a Greener Perspective. *Chem. Sus. Chem.* **2012**, 5, 22-44.
30. Deraedt, C.; Astruc, D., "Homeopathic" Palladium Nanoparticle Catalysis of Cross Carbon-Carbon Coupling Reactions. *Acc. Chem. Res.* **2014**, 47, 494-503.
31. Melaet, G.; Lindeman, A. E.; Somorjai, G. A., Cobalt Particle Size Effects in the Fischer-Tropsch Synthesis and in the Hydrogenation of CO₂ Studied with Nanoparticle Model Catalysts on Silica. *Top. Catal.* **2014**, 57, 500-507.
32. Melaet, G.; Ralston, W. T.; Li, C.-S.; Alayoglu, S.; An, K.; Musselwhite, N.; Kalkan, B.; Somorjai, G. A., Evidence of Highly Active Cobalt Oxide Catalyst for the Fischer-Tropsch Synthesis and CO₂Hydrogenation. *J. Am. Chem. Soc.* **2014**, 136, 2260-2263.
33. Schwab, G.-M., Metal electrons and catalysis. *Trans. Farad. Soc.* **1946**, 42, 689-697.
34. Tauster, S. J.; Fung, S. C.; Garten, R. L., Strong metal-support interactions. Group 8 noble metals supported on titanium dioxide. *J. Am. Chem. Soc.* **1978**, 100, 170-175.
35. Williams, K. J.; Boffa, A. B.; Salmeron, M.; Bell, A. T.; Somorjai, G. A., The kinetics of CO₂ hydrogenation on a Rh foil promoted by titania overlayers. *Catal. Lett.* **1991**, 9, 415-426.
36. Stankovich, S.; Dikin, D. A.; Piner, R. D.; Kohlhaas, K. A.; Kleinhammes, A.; Jia, Y.; Wu, Y.; Nguyen, S. T.; Ruoff, R. S., Synthesis of graphene-based nanosheets via chemical reduction of exfoliated graphite oxide. *Carbon* **2007**, 45, 1558-1565.
37. Rao, e. N. C.; Sood, e. K. A.; Subrahmanyam, e. S. K.; Govindaraj, A., Graphene: the new two dimensional nanomaterial. *Angew. Chem. Int. Ed.* **2009**, 48, 7752-7777.
38. Bolotin, K. I.; Sikes, K. J.; Jiang, Z.; Klima, M.; Fudenberg, G.; Hone, J.; Kim, P.; Stormer, H. L., Ultrahigh electron mobility in suspended graphene. *Sol. St. Comm.* **2008**, 146, 351-355.
39. Lee, C.; Wei, X.; Kysar, J. W.; Hone, J., Measurement of the Elastic Properties and Intrinsic Strength of Monolayer Graphene. *Science* **2008**, 321, 385-388.
40. Geim, A. K.; Novoselov, K. S., The rise of graphene. *Nat. Mat.* **2007**, 6, 183-191.
41. Fan, W.; Lai, Q.; Zhang, Q.; Wang, Y., Nanocomposites of TiO₂ and reduced graphene oxide as efficient photocatalysts for hydrogen evolution. *J. Phys. Chem. C* **2011**, 115, 10694-10701.

42. Sun, H.; Liu, S.; Zhou, G.; Ang, H. M.; Tadé, M. O., Reduced graphene oxide for catalytic oxidation of aqueous organic pollutants. *App. Mat. Interf.* **2012**, 4, 5466-5471.
43. Xiong, Z.; Zhang, L. L.; Zhao, X. S., Visible-Light-Induced Dye Degradation over Copper-Modified Reduced Graphene Oxide. *Chem. Eur. J.* **2011**, 17, 2428-2434.
44. Farha, O. K.; Eryazici, I.; Jeong, N. C., Metal–organic framework materials with ultrahigh surface areas: is the sky the limit? *Journal of the American Chemical Society* **2012**, 134, 15016-15021.
45. Zhou, H. C.; Long, J. R.; Yaghi, O. M., Introduction to metal–organic frameworks. *Chemical reviews* **2012**.
46. Kong, G.-Q.; Han, Z.-D.; He, Y.; Ou, S.; Zhou, W.; Yildirim, T.; Krishna, R.; Zou, C.; Chen, B.; Wu, C.-D., Expanded Organic Building Units for the Construction of Highly Porous Metal-Organic Frameworks. *Chemistry - A European Journal* **2013**, 19, 14886-14894.
47. Gascon, J.; Corma, A.; Kapteijn, F.; I Xamena, F. X., Metal Organic Framework Catalysis: Quo vadis ? *ACS Catalysis* **2014**, 4, 361-378.
48. Roy, A.; Mondal, J.; Banerjee, B.; Mondal, P.; Bhaumik, A.; Islam, S., Pd-grafted porous metal–organic framework material as an efficient and reusable heterogeneous catalyst for C–C coupling reactions in water. *Applied Catalysis A: General* **2014**, 469, 320-327.
49. Bhattacharjee, S.; Lee, Y.-R.; Puthiaraj, P.; Cho, S.-M.; Ahn, W.-S., Metal–Organic Frameworks for Catalysis. *Catalysis Surveys from Asia* **2015**, 19, 203-222.
50. Liu, J.; Chen, L.; Cui, H.; Zhang, J.; Zhang, L.; Su, C.-Y., Applications of metal–organic frameworks in heterogeneous supramolecular catalysis. *Chem. Soc. Rev.* **2014**, 43, 6011-6061.
51. Dhakshinamoorthy, A.; Garcia, H., Metal–organic frameworks as solid catalysts for the synthesis of nitrogen-containing heterocycles. *Chem. Soc. Rev.* **2014**, 43, 5750-5765.
52. Dhakshinamoorthy, A.; Garcia, H., Cascade Reactions Catalyzed by Metal Organic Frameworks. *ChemSusChem* **2014**, 7, 2392-2410.
53. Dhakshinamoorthy, A.; Opanasenko, M., Metal organic frameworks as heterogeneous catalysts for the production of fine chemicals. *Catalysis Science & Technology* **2013**, 3, 2509-2540.
54. Wu, J.; Gao, Y.; Zhang, W.; Tan, Y.; Tang, A.; Men, Y.; Tang, B., Deep desulfurization by oxidation using an active ionic liquid-supported Zr metal–organic framework as catalyst. *Applied Organometallic Chemistry* **2015**, 29, 96-100.
55. Shang, N.-Z.; Feng, C.; Gao, S.-T.; Wang, C., Ag/Pd nanoparticles supported on amine-functionalized metal–organic framework for catalytic hydrolysis of ammonia borane. *International Journal of Hydrogen Energy* **2016**, 41, 944-950.
56. Zhao, M.; Ou, S.; Wu, C.-D., Porous Metal–Organic Frameworks for Heterogeneous Biomimetic Catalysis. *Acc. Chem. Res.* **2014**, 47, 1199-1207.
57. Wang, S.; Wang, X., Multifunctional Metal–Organic Frameworks for Photocatalysis. *Small* **2015**, 11, 3097-3112.
58. Valvekens, P.; Vermoortele, F.; Vos, D. D., Metal–organic frameworks as catalysts: the role of metal active sites. *Catal. Sci. Technol.* **2013**, 3, 1435-1445.
59. Furukawa, S.; Mochizuki, K.; Kinoshita, Y., Three-dimensional porous coordination polymer functionalized with amide groups based on tridentate ligand: selective sorption and catalysis. *J. Am. Chem. Soc.* **2007**, 129, 2607-2614.
60. Miyaura, N.; Suzuki, A., Palladium-Catalyzed Cross-Coupling Reactions of Organoboron Compounds. *Chem. Rev.* **1995**, 95, 2457-2483.
61. Organization, N. P. for palladium-catalyzed cross couplings in organic synthesis. http://www.nobelprize.org/nobel_prizes/chemistry/laureates/2010/ (10 March),
62. Pagliaro, M.; Pandarus, V.; Ciriminna, R.; Béland, F.; Demma Carà, P., Heterogeneous versus Homogeneous Palladium Catalysts for Cross-Coupling Reactions. *Chem. Cat. Chem.* **2012**, 4, 432-445.

63. Annapurna, M.; Parsharamulu, T.; Reddy, V. P.; Suresh, M.; Likhar, P. R.; Kantam, M., Nano palladium supported on high-surface-area metal–organic framework MIL-101: an efficient catalyst for Sonogashira coupling of aryl and heteroaryl bromides with alkynes. *Appl. Organometal. Chem.* **2015**, 29, 234-239.
64. Wang, D.; Deraedt, C.; Salmon, L.; Labrugère, C.; Etienne, L.; Ruiz, J.; Astruc, D., Efficient and Magnetically Recoverable “Click” PEGylated γ -Fe₂O₃–Pd Nanoparticle Catalysts for Suzuki–Miyaura, Sonogashira, and Heck Reactions with Positive Dendritic Effects. *Chem. Eur. J.* **2015**, 21, 1508-1519.
65. Song, H.-q.; Zhu, Q.; Zheng, X.-j.; Chen, X.-g., One-step synthesis of three-dimensional graphene/multiwalled carbon nanotubes/Pd composite hydrogels: an efficient recyclable catalyst for Suzuki coupling reactions. *J. Mat. Chem. A* **2015**, 3, 10368-10377.
66. Mallat, T.; Baiker, A., Oxidation of Alcohols with Molecular Oxygen on Solid Catalysts. *Chem. Rev.* **2004**, 104, 3037-3058.
67. Enache, D. I., Solvent-Free Oxidation of Primary Alcohols to Aldehydes Using Au-Pd/TiO₂ Catalysts. *Science* **2006**, 311, 362-365.
68. Dijkstra, A.; Marino-González, A.; i Payeras, A.; Arends, I. W. C. E.; Sheldon, R. A., Efficient and Selective Aerobic Oxidation of Alcohols into Aldehydes and Ketones Using Ruthenium/TEMPO as the Catalytic System. *J. Am. Chem. Soc.* **2001**, 123, 6826-6833.
69. Pillai, U. R.; Sahle-Demessie, E., Oxidation of alcohols over Fe³⁺/montmorillonite-K10 using hydrogen peroxide. *Appl. Catal. A Gen.* **2003**, 245, 103-109.
70. Stevens, R. V.; Chapman, K. T.; Stubbs, C. A.; Tam, W. W., Further studies on the utility of sodium hypochlorite in organic synthesis. Selective oxidation of diols and direct conversion of aldehydes to esters. *Tetrah.* **1982**, 23, 4647-4650.
71. Xu, C.; Zhang, C.; Li, H.; Zhao, X.; Song, L.; Li, X., An Overview of Selective Oxidation of Alcohols: Catalysts, Oxidants and Reaction Mechanisms. *Catal. Surv. Asia* **2016**, 20, 13-22.
72. Shaabani, A.; Boroujeni, M.; Laeini, M., Porous chitosan-MnO₂ nanohybrid: a green and biodegradable heterogeneous catalyst for aerobic oxidation of alkylarenes and alcohols. *Appl. Organometal. Chem.* **2016**, 30, 154-159.
73. Baruah, D.; Hussain, F. L.; Suri, M.; Saikia, U.; Sengupta, P.; Dutta, D.; Konwar, D., Bi (NO₃)₃·5H₂O and cellulose mediated Cu-NPs — A highly efficient and novel catalytic system for aerobic oxidation of alcohols to carbonyls and synthesis of DFF from HMF. *Catal. Comm.* **2016**, 77, 9-12.
74. Long, J.; Xie, X.; Xu, J.; Gu, Q.; Chen, L.; Wang, X., Nitrogen-Doped Graphene Nanosheets as Metal-Free Catalysts for Aerobic Selective Oxidation of Benzylic Alcohols. *ACS Catal.* **2012**, 2, 622-631.
75. Huang, X.; Wang, X.; Wang, X.; Wang, X.; Tan, M.; Ding, W.; Lu, X., P123-stabilized Au–Ag alloy nanoparticles for kinetics of aerobic oxidation of benzyl alcohol in aqueous solution. *J. Catal.* **2013**, 301, 217-226.
76. Zamani, F.; Hosseini, S., Palladium nanoparticles supported on Fe₃O₄/amino acid nanocomposite: Highly active magnetic catalyst for solvent-free aerobic oxidation of alcohols. *Catal. Comm.* **2014**, 43, 164-168.
77. Yan, Y.; Chen, Y.; Jia, X.; Yang, Y., Palladium nanoparticles supported on organosilane-functionalized carbon nanotube for solvent-free aerobic oxidation of benzyl alcohol. *Appl. Catal. B Environ.* **2014**, 156, 385-397.
78. Li, S.; El-Shall, M. S., Synthesis of nanoparticles by reactive laser vaporization: silicon nanocrystals in polymers and properties of gallium and tungsten oxides. *Appl. surf. sci.* **1998**, 330-338.
79. El-Shall, M. S.; Slack, W.; Vann, W.; Kane, D., Synthesis of nanoscale metal oxide particles using laser vaporization/condensation in a diffusion cloud chamber. *J. Phys. Chem.* **1994**, 98.
80. Samy, S.; Li, S., Synthesis of nanoparticles by a laser-vaporization-controlled condensation technique. *Optic. Sci.* **1997**, 3123, 98-109.

81. Katz, M. J.; Brown, Z. J.; Colón, Y. J.; Siu, P. W.; Scheidt, K. A.; Snurr, R. Q.; Hupp, J. T.; Farha, O. K., A facile synthesis of UiO-66, UiO-67 and their derivatives. *Chem. Comm.* **2013**, 49, 9449-9451.
82. Miedziak, P.; Sankar, M.; Dimitratos, N.; Lopez-Sanchez, J. A., Oxidation of benzyl alcohol using supported gold–palladium nanoparticles. *Catal. Today* **2011**, 164, 315-319.
83. Li, S.; Silvers, S. J.; El-Shall, M. S., Surface oxidation and luminescence properties of weblike agglomeration of silicon nanocrystals produced by a laser vaporization-controlled condensation technique. *J. Phys. Chem. B* **1997**, 101, 1794-1802.
84. Hamad, S.; Podagatlapalli, G. K., Femtosecond ablation of silicon in acetone: tunable photoluminescence from generated nanoparticles and fabrication of surface nanostructures. *J. Phys. Chem. C* **2014**, 118, 7139-7151.
85. Holmes, J. D.; Ziegler, K. J.; Doty, C. R.; Pell, L. E.; Johnston, K. P.; Korgel, B. A., Highly luminescent silicon nanocrystals with discrete optical transitions. *J. A. Chem. Soc.* **2001**, 123, 3743-3748.
86. Wu, J.; Dai, J.; Shao, Y.; Sun, Y., One-step synthesis of fluorescent silicon quantum dots (Si-QDs) and their application for cell imaging. *RSC Adv.* **2015**, 5, 83581-83587.
87. Afshani, P.; Moussa, S.; Atkinson, G.; Kisurin, V. Y.; El-Shall, S. M., Enhanced photothermal effect of surface oxidized silicon nanocrystals anchored to reduced graphene oxide nanosheets. *Chem. Phys. Lett.* **2016**, 650, 148-153.
88. Chen, C.; Kimura, S.; Nozaki, S.; Ono, H.; Uchida, K., Selective Formation of Size-Controlled Silicon Nanocrystals by Photosynthesis in SiO Nanoparticle Thin Film. *IEEE Transac. Nanotech.* **2006**, 5, 671-676.
89. Liao, Y.-C.; Roberts, J. T., Self-Assembly of Organic Monolayers on Aerosolized Silicon Nanoparticles. *J. Am. Chem. Soc.* **2006**, 128, 9061-9065.
90. Rosso-Vasic, M.; Spruijt, E.; van Lagen, B.; Cola, L.; Zuilhof, H., Alkyl-Functionalized Oxide-Free Silicon Nanoparticles: Synthesis and Optical Properties. *Small* **2008**, 4, 1835-1841.
91. El-Shall, M. S.; Li, S.; Turkki, T.; Graiver, D.; Pernisz, U. C.; Baraton, M. I., Synthesis and Photoluminescence of Weblike Agglomeration of Silica Nanoparticles. *J. Phys. Chem.* **1995**, 99, 17805-17809.
92. Umezu, I.; Sugimura, A.; Inada, M.; Makino, T.; Matsumoto, K.; Takata, M., Formation of nanoscale fine-structured silicon by pulsed laser ablation in hydrogen background gas. *Phys. Rev. B* **2007**, 76, 045328-1-10.
93. Lam, C.; Zhang, Y. F.; Tang, Y. H.; Lee, C. S.; Bello, I.; Lee, S. T., Large-scale synthesis of ultrafine Si nanoparticles by ball milling. *J. Cryst. Grow.* **2000**, 220, 466-470.
94. Riabinina, D.; Durand, C.; Chaker, M.; Rosei, F., Photoluminescent silicon nanocrystals synthesized by reactive laser ablation. *Appl. Phys. Lett.* **2006**, 88, 73105.
95. Heintz, A. S.; Fink, M. J.; Mitchell, B. S., Mechanochemical Synthesis of Blue Luminescent Alkyl/Alkenyl-Passivated Silicon Nanoparticles. *Adv. Mat.* **2007**, 19, 3984-3988.
96. Li, S.; El-Shall, M. S., Synthesis of nanoparticles by reactive laser vaporization: silicon nanocrystals in polymers and properties of gallium and tungsten oxides. *Appl. Surf. Sci.* **1998**, 127, 330-338.
97. Okada, T.; Iwaki, T.; Yamamoto, K.; Kasahara, H.; Abe, K., Raman scattering from gas-evaporated silicon small particles. *Solid State Comm.* **1984**, 49, 809-812.
98. Li, S.; Germanenko, I. N.; El-Shall, M. S., Nanoparticles from the Vapor Phase: Synthesis and Characterization of Si, Ge, MoO₃, and WO₃ Nanocrystals. *J. Clust. Sci.* **1999**, 10, 533-547.
99. Yin, Y.-X.; Xin, S.; Wan, L.-J.; Li, C.-J.; Guo, Y.-G., Electrospray Synthesis of Silicon/Carbon Nanoporous Microspheres as Improved Anode Materials for Lithium-Ion Batteries. *J. Phys. Chem. C* **2011**, 115, 14148-14154.
100. Prosini, P.; Carewska, M.; Maroni, F.; Tossici, R.; Nobili, F., A lithium-ion battery based on LiFePO₄ and silicon/reduced graphene oxide nanocomposite. *Solid State Ion.* **2015**, 283, 145-151.

101. Nasrollahzadeh, M.; Sajadi, M. S.; Rostami-Vartooni, A.; Alizadeh, M.; Bagherzadeh, M., Green synthesis of the Pd nanoparticles supported on reduced graphene oxide using barberry fruit extract and its application as a recyclable and heterogeneous catalyst for the reduction of nitroarenes. *J. Coll. Interf. Sci.* **2016**, 466, 360-368.
102. Zedan, A. F.; Moussa, S.; Terner, J.; Atkinson, G.; El-Shall, S. M., Ultrasmall Gold Nanoparticles Anchored to Graphene and Enhanced Photothermal Effects by Laser Irradiation of Gold Nanostructures in Graphene Oxide Solutions. *ACS Nano* **2013**, 7, 627-636.
103. Ferrari, A. C., Raman spectroscopy of graphene and graphite: disorder, electron-phonon coupling, doping and nonadiabatic effects. *Solid State comm.* **2007**, 143, 47-57.
104. Milani, A.; Tommasini, M.; Russo, V., Raman spectroscopy as a tool to investigate the structure and electronic properties of carbon-atom wires. *Beilstein J. Nanotech.* **2015**, 6, 480-491.
105. Nan, H.; Ni, Z.; Wang, J.; Zafar, Z.; Shi, Z.; Wang, Y., The thermal stability of graphene in air investigated by Raman spectroscopy. *J Raman Spectrosc.* **2013**, 44, 1018-1021.
106. Yang, F.; Chi, C.; Dong, S.; Wang, C.; Jia, X.; Ren, L.; Zhang, Y.; Zhang, L.; Li, Y., Pd/PdO nanoparticles supported on carbon nanotubes: A highly effective catalyst for promoting Suzuki reaction in water. *Catal. Today* **2015**, 256, 186-192.
107. Radtke, M.; Stumpf, S.; Schröter, B.; Höppener, S.; Schubert, U.; Ignaszak, A., Electrodeposited palladium on MWCNTs as 'semi-soluble heterogeneous' catalyst for cross-coupling reactions. *Tetrah. Lett.* **2015**, 56, 4084-4087.
108. Fareghi-Alamdari, R.; Haqiqi, M. G.; Zekri, N., Immobilized Pd(0) nanoparticles on phosphine-functionalized graphene as a highly active catalyst for Heck, Suzuki and N-arylation reactions. *New J. Chem.* **2015**, 40, 1287-1296.
109. Gómez-Martínez, M.; Buxaderas, E.; Pastor, I. M.; Alonso, D. A., Palladium nanoparticles supported on graphene and reduced graphene oxide as efficient recyclable catalyst for the Suzuki-Miyaura reaction of potassium aryltrifluoroborates. *J. Mol. Catal. A Chem.* **2015**, 404, 1-7.
110. Brinkley, K. W.; Burkholder, M.; Siamaki, A. R.; Belecki, K.; Gupton, F. B., The continuous synthesis and application of graphene supported palladium nanoparticles: a highly effective catalyst for Suzuki-Miyaura cross-coupling reactions. *Green Proces. Synth.* **2015**, 0.
111. Lsane, K. E.; Shendage, S. S.; Nagarkar, J. M., Efficient Sonogashira and Suzuki-Miyaura coupling reaction catalyzed by Pd-Nanoparticles. *J. Chem. Sci.* **2015**, 127, 425-431.
112. Durap, F.; Metin, Ö., Monodisperse palladium nanoparticles supported on chemically derived graphene: highly active and reusable nanocatalysts for Suzuki-Miyaura cross-coupling reactions. *Turk. J. Chem.* **2015**, 39, 1247-1256.
113. Hussain, N.; Borah, A.; Darabdhara, G.; Gogoi, P.; Azhagan, V.; Shelke, M. V.; Das, M. R., A green approach for the decoration of Pd nanoparticles on graphene nanosheets: An in situ process for the reduction of C-C double bonds and a reusable catalyst for the Suzuki cross-coupling reaction. *New J. Chem.* **2015**, 39, 6631-6641.
114. Višić, B.; Cohen, H.; Popovitz-Biro, R.; Tenne, R.; Sokolov, V. I.; Abramova, N. V.; Buyanovskaya, A. G.; Dzvonkovskii, S. L.; Lependina, O. L., Direct Synthesis of Palladium Catalyst on Supporting WS₂ Nanotubes and its Reactivity in Cross-Coupling Reactions. *Chem. Asian J.* **2015**, 10, 2234-2239.
115. Jawale, D. V.; Gravel, E.; Boudet, C.; Shah, N.; Geertsen, V.; Li, H.; Namboothiri, I. N. N.; Doris, E., Room temperature Suzuki coupling of aryl iodides, bromides, and chlorides using a heterogeneous carbon nanotube-palladium nanohybrid catalyst. *Catal. Sci. & Tech.* **2015**, 5, 2388-2392.
116. Cornelio, B.; Saunders, A. R.; Solomonsz, W. A.; Laronze-Cochard, M.; Fontana, A.; Sapi, J.; Khlobystov, A. N.; Rance, G. A., Palladium nanoparticles in catalytic carbon nanoreactors: the effect of confinement on Suzuki-Miyaura reactions. *J. Mat. Chem. A* **2015**, 3, 3918-3927.
117. Nasrollahzadeh, M.; Azarian, A.; Ehsani, A.; Zahraei, A., Facile synthesis of Fe@Pd nanowires and their catalytic activity in ligand-free CN bond formation in water. *Tetrah. Lett.* **2014**, 55, 2813-2817.

118. Yang, Y.; Cong, D.; Hao, S., Template-Directed Ordered Mesoporous Silica@Palladium-Containing Zinc Metal–Organic Framework Composites as Highly Efficient Suzuki Coupling Catalysts. *Chem. Cat. Chem.* **2016**, 8, 900-905.
119. Moussa, S.; Siamaki, A. R.; Gupton, F. B.; El-Shall, S. M., Pd-Partially Reduced Graphene Oxide Catalysts (Pd/PRGO): Laser Synthesis of Pd Nanoparticles Supported on PRGO Nanosheets for Carbon–Carbon Cross Coupling Reactions. *ACS Catal.* **2012**, 2, 145-154.
120. Siamaki, A. R.; Rahman, A. S. K.; Abdelsayed, V., Microwave-assisted synthesis of palladium nanoparticles supported on graphene: A highly active and recyclable catalyst for carbon–carbon cross-coupling reactions. *J. Catal.* **2011**, 279, 1-11.
121. Elazab, H. A.; Siamaki, A. R.; Moussa, S.; Gupton, B. F., Highly efficient and magnetically recyclable graphene-supported Pd/Fe₃O₄ nanoparticle catalysts for Suzuki and Heck cross-coupling reactions. *Appl. Catal. A* **2015**, 58-69.
122. Cavka, J. H.; Jakobsen, S.; Olsbye, U., A new zirconium inorganic building brick forming metal organic frameworks with exceptional stability. *J. Am. Chem. Soc.* **2008**, 130, 13850-13851.
123. Mondloch, J. E.; Katz, M. J.; Planas, N.; Semrouni, D.; Gagliardi, L.; Hupp, J. T.; Farha, O. K., Are Zr₆-based MOFs water stable? Linker hydrolysis vs. capillary-force-driven channel collapse. *Chem. Comm.* **2014**, 50, 8944-8946.
124. Wu, H.; Yildirim, T.; Zhou, W., Exceptional Mechanical Stability of Highly Porous Zirconium Metal–Organic Framework UiO-66 and Its Important Implications. *J. Phys. Chem. Lett.* **2013**, 4, 925-930.
125. Gross, S.; Serre, C.; Devic, T.; Bauer, M.; Férey, G., A zirconium methacrylate oxocluster as precursor for the low-temperature synthesis of porous zirconium (IV) dicarboxylates. *Chem. Comm.* **2010**, 46, 767-769.
126. Margiolaki, I.; Loiseau, T.; Férey, G.; Senker, J., $\cdot x$ H₂O: A 12-Connected Porous Metal–Organic Framework with an Unprecedented Aluminum-Containing Brick. *Angew. Chem.* **2009**, 121, 5265-5268.
127. Furukawa, H.; Cordova, K. E.; O'Keeffe, M., The chemistry and applications of metal-organic frameworks. *Science* **2013**, 341, 974.
128. Kandiah, M.; Nilsen, M.; Usseglio, S.; Jakobsen, S.; Olsbye, U.; Tilset, M.; Larabi, C.; Quadrelli, E.; Bonino, F.; Lillerud, K., Synthesis and Stability of Tagged UiO-66 Zr-MOFs. *Chem. Mat.* **2010**, 22, 6632-6640.
129. Arrozi, U.; Wijaya, H. W.; Patah, A.; Permana, Y., Efficient acetalization of benzaldehydes using UiO-66 and UiO-67: Substrates accessibility or Lewis acidity of zirconium. *Appl. Catal. A Gen.* **2015**, 506, 77-84.
130. DeCoste, J. B.; Peterson, G. W.; Jasuja, H.; Glover, G. T.; Huang, Y.-g.; Walton, K. S., Stability and degradation mechanisms of metal–organic frameworks containing the Zr₆O₄(OH)₄ secondary building unit. *J. Mat. Chem. A* **2013**, 1, 5642-5650.
131. Pullen, S.; Fei, H.; Orthaber, A.; Cohen, S. M.; Ott, S., Enhanced photochemical hydrogen production by a molecular diiron catalyst incorporated into a metal–organic framework. *J. Am. Chem. Soc.* **2013**, 135, 16997-17003.
132. Abid, H.; Tian, H.; Ang, H.-M.; Tade, M. O.; Buckley, C. E.; Wang, S., Nanosize Zr-metal organic framework (UiO-66) for hydrogen and carbon dioxide storage. *Chemic. Eng. J.* **2012**, 187, 415-420.
133. McGuirk, M. C.; Katz, M. J.; Stern, C. L.; Sarjeant, A. A.; Hupp, J. T.; Farha, O. K.; Mirkin, C. A., Turning On Catalysis: Incorporation of a Hydrogen-Bond-Donating Squaramide Moiety into a Zr Metal–Organic Framework. *J. Am. Chem. Soc.* **2015**, 137, 919-925.
134. Balbuena, P. B.; Gubbins, K. E., Theoretical interpretation of adsorption behavior of simple fluids in slit pores. *Langmuir* **1993**, 9, 1801-1814.
135. Rodriguez-Reinoso, F.; Rouquerol, J., Physisorption of gases, with special reference to the evaluation of surface area and pore size distribution (IUPAC Technical Report). *Pure Appl. Chem.* **2015**, 87, 1051-1069.

136. Chen, L.; Chen, X.; Liu, H.; Bai, C.; Li, Y., One-step encapsulation of Pd nanoparticles in MOFs via a temperature control program. *J. Mater. Chem. A* **2015**, 3, 15259-15264.
137. Ebrahim, A. M.; Levasseur, B.; Bandoz, T. J., Interactions of NO₂ with Zr-based MOF: effects of the size of organic linkers on NO₂ adsorption at ambient conditions. *Langmuir* **2012**, 29, 168-174.
138. Shevchenko, A. V.; Ruban, A. K.; Dudnik, E. V.; Mel'nikova, V. A., Hydrothermal synthesis of ultrafine zirconia powders. *Powd. Metallur. Met. Ceram.* **1997**, 36, 420-424.
139. Wang, C.; Xie, Z.; deKrafft, K. E.; Lin, W., Doping metal-organic frameworks for water oxidation, carbon dioxide reduction, and organic photocatalysis. *J. Am. Chem. Soc.* **2011**, 133, 13445-13454.
140. Li, S.; Wang, X.; He, Q.; Chen, Q.; Xu, Y.; Yang, H.; Lü, M.; Wei, F.; Liu, X., Synergistic effects in N-K₂Ti₄O₉/UiO-66-NH₂ composites and their photocatalysis degradation of cationic dyes. *Chin. J. Catal.* **2016**, 37, 367-377.
141. Flage-Larsen, E.; Røyset, A.; Cavka, J.; Thorshaug, K., Band Gap Modulations in UiO Metal-Organic Frameworks. *J. Phys. Chem. C* **2013**, 117, 20610-20616.
142. Teng, X.; Wang, Q.; Liu, P.; Han, W.; Frenkel, A. I., Formation of Pd/Au nanostructures from Pd nanowires via galvanic replacement reaction. *J. Am. Chem. Soc.* **2008**, 130, 1093-1101.
143. Yin, Z.; Chi, M.; Zhu, Q.; Ma, D.; Sun, J.; Bao, X., Supported bimetallic PdAu nanoparticles with superior electrocatalytic activity towards methanol oxidation. *J. Mat. Chem. A* **2013**, 1, 9157-9163.
144. Benkhaled, M.; Morin, S.; Pichon, C.; Thomazeau, C., Synthesis of highly dispersed palladium alumina supported particles: Influence of the particle surface density on physico-chemical properties. *Appl. Catal. A* **2006**, 312, 1-11.
145. Sankar, M.; Nowicka, E.; Carter, E.; Murphy, D. M.; Knight, D. W.; Bethell, D.; Hutchings, G. J., The benzaldehyde oxidation paradox explained by the interception of peroxy radical by benzyl alcohol. *Nat. Comm.* **2014**, 5, 1-6.
146. Ilyas, M.; Siddique, M.; Saeed, M., Liquid-phase aerobic oxidation of benzyl alcohol catalyzed by mechanochemically synthesized manganese oxide. *Chin. Sci. Bullet.* **2013**, 58, 2354-2359.
147. Sun, Y.; Gray, S. K.; Peng, S., Surface chemistry: a non-negligible parameter in determining optical properties of small colloidal metal nanoparticles. *Physical Chemistry Chemical Physics* **2011**, 13, 11814.
148. Xiong, Y.; Brunson, M.; Huh, J.; Huang, A.; Coster, A.; Wendt, K.; Fay, J.; Qin, D., The Role of Surface Chemistry on the Toxicity of Ag Nanoparticles. *Small* **2013**, 9, 2628-2638.
149. Mistri, R.; Das, D.; Llorca, J.; Dominguez, M.; Mandal, T.; Mohanty, P.; Ray, B.; Gayen, A., Selective liquid phase benzyl alcohol oxidation over Cu-loaded LaFeO₃ perovskite. *RSC Adv.* **2016**, 6, 4469-4477.
150. Liu, H.; Liu, Y.; Li, Y.; Tang, Z.; Jiang, H., Metal-Organic Framework Supported Gold Nanoparticles as a Highly Active Heterogeneous Catalyst for Aerobic Oxidation of Alcohols. *J. Phys. Chem. C* **2010**, 114, 13362-13369.
151. Chen, L.; Chen, H.; Luque, R.; Li, Y., Metal-organic framework encapsulated Pd nanoparticles: towards advanced heterogeneous catalysts. *Chem. Sci.* **2014**, 5, 3708-3714.
152. Luan, Y.; Qi, Y.; Gao, H.; Zheng, N.; Wang, G., Synthesis of an amino-functionalized metal-organic framework at a nanoscale level for gold nanoparticle deposition and catalysis. *J. Mat. Chem. A* **2014**, 2, 20588-20596.
153. Zhu, J.; Wang, P.; Lu, M., Selective oxidation of benzyl alcohol under solvent-free condition with gold nanoparticles encapsulated in metal-organic framework. *Appl. Catal. A Gen.* **2014**, 477, 125-131.
154. Tilgner, D.; Friedrich, M.; Hermannsdörfer, J.; Kempe, R., Titanium Dioxide Reinforced Metal-Organic Framework Pd Catalysts: Activity and Reusability Enhancement in Alcohol Dehydrogenation Reactions and Improved Photocatalytic Performance. *Chem. Cat. Chem.* **2015**, 7, 3916-3922.
155. Li, X.; Guo, Z.; Xiao, C.; Goh, T.; Tesfagaber, D.; Huang, W., Tandem Catalysis by Palladium Nanoclusters Encapsulated in Metal-Organic Frameworks. *ACS Catal.* **2014**, 4, 3490-3497.

156. Chen, G.-J.; Wang, J.-S.; Jin, F.-Z.; Liu, M.-Y.; Zhao, C.-W.; Li, Y.-A.; Dong, Y.-B., Pd@Cu(II)-MOF-Catalyzed Aerobic Oxidation of Benzylic Alcohols in Air with High Conversion and Selectivity. *Inorg. Chem.* **2016**, 55, 3058-3064.
157. Hossain, S.; Jin, M. J.; Park, J.; Yingjie, Q.; Yang, D. A., Oxidation and Reduction of Various Substrates Over a Pd (II) Containing Post-Synthesis Metal Organic Framework. *Catal. Lett.* **2013**, 143, 122-125.
158. Leus, K.; Concepcion, P.; Vandichel, M.; Meledina, M.; Grirrane, A.; Esquivel, D.; Turner, S.; Poelman, D.; Waroquier, M.; Speybroeck, V. V.; Tendeloo, V. G.; García, H.; Voort, V. P., Au@UiO-66: a base free oxidation catalyst. *RSC Adv.* **2015**, 5, 22334-22342.
159. Chen, G.; Wu, S.; Liu, H.; Jiang, H.; Li, Y., Palladium supported on an acidic metal-organic framework as an efficient catalyst in selective aerobic oxidation of alcohols. *Green Chem.* **2012**, 15, 230-235.
160. Ferrando-Soria, J.; Luz, I.; Serra-Crespo, P.; Skupien, E., The oxamate route, a versatile post-functionalization for metal incorporation in MIL-101 (Cr): Catalytic applications of Cu, Pd, and Au. *J. Catal.* **2013**, 307, 295-304.
161. Wu, H.; Chua, Y.; Krungleviciute, V.; Tyagi, M.; Chen, P.; Yildirim, T.; Zhou, W., Unusual and Highly Tunable Missing-Linker Defects in Zirconium Metal-Organic Framework UiO-66 and Their Important Effects on Gas Adsorption. *J. A. Chem. Soc.* **2013**, 135, 10525-10532.

VITA

Vitaly Yevgeniyevich Kisurin was born on March 16th, 1991 in city of Saint Petersburg, Russia. He graduated from high school in Russia and came over to the United States in 2007 as an international student. After attending VCU he received his Bachelor of Science in Chemistry and since fall of 2012 he is pursuing his PhD in Nanoscience.